

# **Seismic modeling of plaster models deformed in extension and contraction**

Christine Torsvik Andersen

Thesis for the degree

Master of Science



Department of Earth Science

University of Bergen

November 2014



# Abstract

The effects of overburden, burial depth, source-receiver distance and frequency on seismic resolution have been studied in this thesis. Synthetic seismic sections of two plaster models, where a volume of plaster has been deformed in a plane strain deformation apparatus, have been created using the NORSAR-2D/3D- and SeisRoX modeling tools in order to observe which properties that enhance the seismic images in the best possible way.

Three different models have been created for each plaster model, hence, six different models will be displayed in this thesis. The modeling experiments differ with regards to velocity and density based on burial depth, where one shallow, one medium and one deep model have been created.

The plaster models were photographed and transferred into the NORSAR-2D software in order to create a geophysical framework for synthetic seismic modeling. Based on well logs provided by Statoil ASA (Appendix A), four different stratigraphic units were used as an analogue in order to establish the P- and S-wave seismic velocities and densities, and calculations of the matrix shear- and bulk modulus were made. Each artificial layer in the plaster model was assigned with values from each stratigraphic unit, in order to create a realistic model.

It has become clear that the distance between source and receiver is crucial when it comes to representation of dipping reflectors. Also, I demonstrate that regardless of survey direction, the same structures were displayed in the seismograms of similar depth, except for additional noise and lower reflection amplitudes in the strike survey seismograms.

When it comes to resolution of subsurface structures and potential reservoirs, creating synthetic seismograms based on structurally realistic plaster models can possibly relate the synthetic seismic sections to real seismic data, which is shown in this thesis.



## Acknowledgements

This thesis is a part of my Master's Degree in petroleum geology and has been written at the Department of Earth Science at the University of Bergen.


First of all, I would like to thank my supervisors. Haakon Fossen (UiB, Department of Earth Science) has encouraged and helped me during the last two years, which I am very grateful for. Also, thank you to Tor Arne Johansen (UiB, Department of Earth Science).

Second, I owe NORSTAR Innovation a huge thank you, especially Aasmund Drottning who has been of great assistance in teaching me how to use the NORSTAR-2D/3D- and SeisRoX software in addition to showing great patience and advice.

During my thesis, I have worked with some great people. Therefore, I would like to thank my fellow students Marie, Maria and Margrete, who are also working with plaster experiments, Signe Ottesen (Statoil ASA), Eivind Bastesen (UiB, CIPR) and Atle Rotevatn (UiB, Department of Earth Science) for their engagement. Also, thank you to Einar Magerøy (Statoil ASA) for providing me with well logs and advice. Kenneth Bredesen (PhD at UiB, Department of Earth Science) and Erling Hugo Jensen (postdoc. UiB) deserves a huge thank you for reading my thesis and giving me much needed feedback and motivation.

Through my five years at the university, there have been a lot of people who has made an impression on me. Without these people, my every day job as a student would not have been as amazing as it has been. Therefore, I would sincerely like to thank Arve, Knut, Andreas, Matias, Bjarte, Felix, Ingunn, Morten, Eirik and Tine for being the best study-buddies a girl can ask for. Also, thank you to the rest of my fellow students for some great years and fieldtrips.

Last but not least, I would like to thank my parents, Lisbeth and Rune, and my boyfriend Eirik for their support through my entire study and for giving me a shoulder to cry on when needed. Your patience, encouragement and understanding is highly valued.



Christine Torsvik Andersen



# Contents

<b>1</b>	<b>Introduction.....</b>	<b>1</b>
1.1	Aim and motivation .....	1
1.2	Main objectives.....	2
<b>2</b>	<b>Geological background theory .....</b>	<b>3</b>
2.1	Introduction .....	3
2.2	Contractional regimes.....	3
2.3	Extensional regimes.....	5
2.4	Geological analogue .....	6
<b>3</b>	<b>Geophysical background theory .....</b>	<b>8</b>
3.1	Introduction .....	8
3.1.1	Stress, strain and elastic moduli.....	8
3.1.2	Seismic waves and seismic velocities.....	10
3.1.3	Attenuation of seismic energy in homogeneous media .....	12
3.1.4	Ray paths in layered media .....	13
3.2	Geophysical exploration.....	17
3.2.1	Seismic reflection survey.....	17
3.2.2	Displaying seismic reflection data.....	20
3.2.3	Seismic resolution.....	22
3.3	Seismic processing .....	23
3.3.1	Basic processing.....	23
3.4	Seismic imaging .....	24
3.4.1	Post-stack migration.....	24
3.4.2	Pre-stack depth migration (PSDM).....	24
3.5	Seismic forward modeling.....	29
3.6	Seismic interpretation .....	29
<b>4</b>	<b>Plaster models.....</b>	<b>30</b>
4.1	Introduction .....	30
4.2	Method.....	30
4.3	Contractional plaster model development .....	32
4.4	Extensional plaster model development .....	34
<b>5</b>	<b>Modeling software and methods.....</b>	<b>35</b>
5.1	Introduction .....	35
5.2	NORSAR-2D model building procedure .....	35
5.3	From 2D model to 2.5D model.....	42
5.4	From 2.5D model to a SeisRoX 3D model.....	42

5.5 SeisRoX™ modeling software .....	42
5.5.1 The multi-domain model.....	43
5.5.2 The SimPLI (Simulated Prestack Local Imaging) method .....	44
5.6 General modeling setup in SeisRoX.....	44
5.6.1 Definition of background model .....	44
5.6.2 Survey definition.....	46
5.6.3 Creating a workflow .....	48
<b>6 Results .....</b>	<b>52</b>
6.1 General result information.....	52
6.2 Contractional plaster model results .....	52
6.2.1 Strike- and dip survey at 1 km depth using Ricker zero 30 Hz frequency. ....	55
6.2.2 Strike- and dip survey at 3 km depth using Ricker zero 20 Hz frequency. ....	56
6.2.3 Strike- and dip survey at 5 km depth using Ricker zero 10 Hz frequency. ....	57
6.2.4 Azimuth and dip of potentially illuminated reflectors .....	59
6.3 Extensional plaster model.....	62
6.3.1 Strike- and dip survey at 1 km depth using Ricker zero 30 Hz frequency. ....	64
6.3.2 Strike- and dip survey at 3 km depth using Ricker zero 20 Hz frequency. ....	65
6.3.3 Strike- and dip survey at 5 km depth using Ricker zero 10 Hz frequency. ....	66
6.3.4 Azimuth and dip of potentially illuminated reflectors .....	68
<b>7 Discussions .....</b>	<b>70</b>
<b>8 Conclusions.....</b>	<b>78</b>
<b>References .....</b>	<b>80</b>
<b>APPENDIX A .....</b>	<b>82</b>
<b>APPENDIX B.....</b>	<b>87</b>



# 1 Introduction

## 1.1 Aim and motivation

Seismic data is an essential tool for petroleum exploration and reservoir characterization. In order to obtain accurate subsurface imaging from seismic data, a seismic survey must be carefully designed and precisely carried out. However, real seismic measurements are influenced by many uncertainties that limit a correct image of the subsurface. Hence, analysis that may add to our understanding of the seismic response from various subsurface scenarios are important.

Seismic modeling is a process to study how seismic data in terms of travel times, amplitudes, frequency and attenuation responds to various geological scenarios represented by parameters describing the elastic properties of the rock, such as velocity- and density models. Figure 1.1 illustrates the link between elastic properties and seismic data where seismic modeling generates synthetic seismic data when elastic properties of a geological model are known. For instance, in petroleum exploration, one might want to model the seismic response in a pre-defined geological scenario outlining a reservoir system that one suspect to be present in an area. A real geological model may therefore be subsequently implemented and transformed into a velocity- or density model.

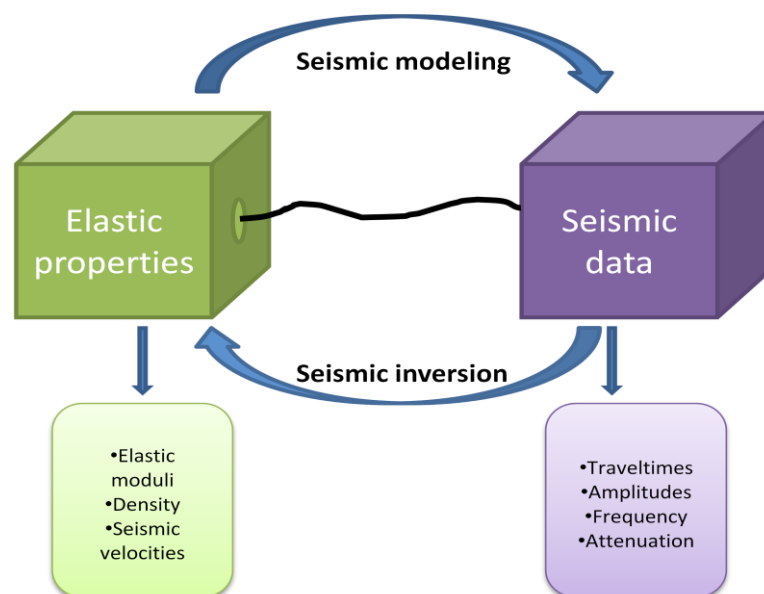


**Figure 1.1:** A simple workflow scheme that shows how the seismic data and elastic properties are linked by seismic modeling and inversion. Example of model parameters within each domain are given in the lowermost boxes (Modified from Bredesen, 2012).

Several different techniques have been applied to reconstruct structurally deformed areas. When creating geological models in the laboratory, different modeling materials have been used, like clay (Cloos, 1955), sand (McClay & Ellis, 1987) and combinations of sand-silicone (Brun & Tron, 1993). Clay and sand are in many ways well-suited modeling materials, but their inability to develop and preserve the finest geological structures is an important limiting factor. Sales (1987) suggested using plaster as a modeling material. Based on the fact that plaster is a very fine-grained material that solidifies quickly when mixed with water, plaster allows for the development and preservation of complex structures. Hence, it has proven to be well suited for modeling tectonic structures.

Many plaster experiments have been performed at the Structural Geological Laboratory at the Department of Earth Science at the University of Bergen in the period 1990-2000, some of which are described in Gabrielsen and Clausen (2001) and Fossen and Gabrielsen (1996), and more recently in conjunction with ongoing master projects.

Usually, seismic data is acquired by a seismic survey, and the elastic properties are established by studying well logs. In this study, plaster models deformed in extension and contraction have been investigated and corresponding seismograms have been modeled with various configurations such as frequency and target depth.

From a geological point of view, the main focus of this study is to observe how subsurface geological structures are displayed when the elastic properties and structure is known. By varying the depth and frequency based on the subsurface stratigraphy, the seismic imaging (i.e. resolution and illumination) of the seismic sections are exceptionally different.

## **1.2 Main objectives**

- Model seismograms from plaster models.
- Study how the structural aspects change based on different configurations.
- Study how varying frequencies of seismic waves influence the seismograms.
- Study how the survey direction (strike- or dip) affects the seismograms.

## 2 Geological background theory

### 2.1 Introduction

This chapter describes basic structural geological background theory for contractional- and extensional regimes, mainly focusing on faults and fault geometries seen in the plaster models. In addition, the Brent Group, Dunlin Group, Statfjord Formation and Draupne Formation will be briefly reviewed, since these North Sea stratigraphic units and their properties will be utilized stratigraphically and used as an analogue for elastic properties in the synthetic seismic modeling.

### 2.2 Contractional regimes

Contractional faults are most commonly found in the contractional tectonic regime, particularly along convergent plate boundaries. Not only are contractional faults important when it comes to understanding the development of orogenic zones, but also when it comes to improved petroleum exploration methods since many hydrocarbon accumulations are found in thrust and fold belts.

When an area is shortened by some tectonic or gravitational force, the development of contractional deformation structures occurs mainly in the form of folds or faults. The faults, which are of particular interest to this thesis, are named based on the dip angle: reverse faults have dips larger than  $30^\circ$  and thrust faults have dips less than  $30^\circ$ . Reverse faults are generally smaller (i.e. smaller displacement) than thrust faults, but there is a gradual transition between them (Fossen, 2010).

### ***Fault geometries***

*Imbrication zones* (Figure 2.1) are contractional faults typically found in the foreland of an orogenic zone. Imbrication zones are series of reverse faults with similar orientation that is connected by a low-angle floor thrust (Fossen, 2010). Repeated layers of strata, duplexes and multiple thrust faults are expected to be seen in a thrust environment (Boyer & Elliott, 1982).

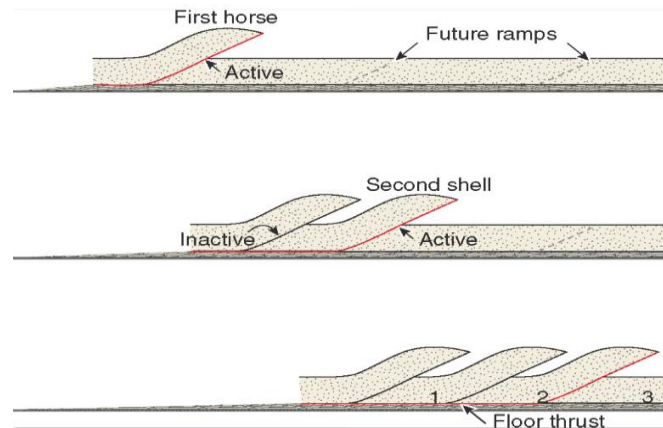


**Figure 2.1:** The "standard" formation of an imbrication zone, known as "in sequence thrusting". The horses get younger towards the foreland (right) in this model. Deviations from this model is known as "out of sequence thrusting". (From Fossen, 2010).

When two flat thrust segments are connected through a reverse fault which is steeper than the thrust faults, we get a structure called *flat-ramp-flat* (Figure 2.2).

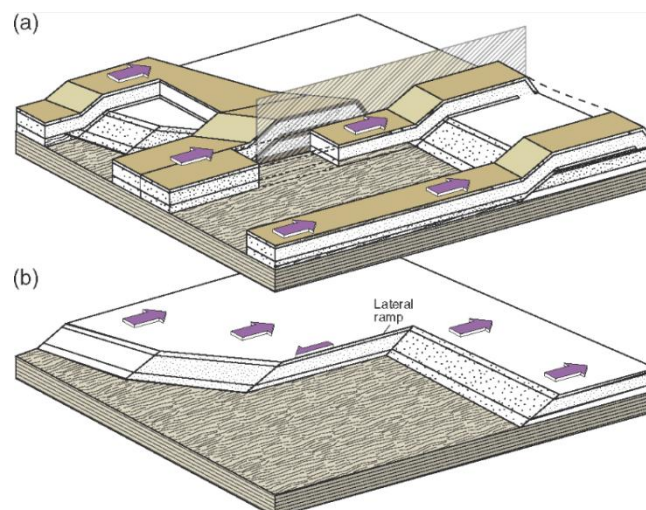


**Figure 2.2:** Various thrust ramps and their geometries. (a) Hanging-wall strata included, with ramps appearing as folds. (b) Hanging wall removed. (From Fossen, 2010).

The reverse faults (ramps) may lead to thrusts or reverse faults with displacement in the opposite direction, known as *back-thrusts* (Figure 2.3), that form due to geometric differences. Back-thrusts are generally associated with steep ramp structures (Fossen, 2010).

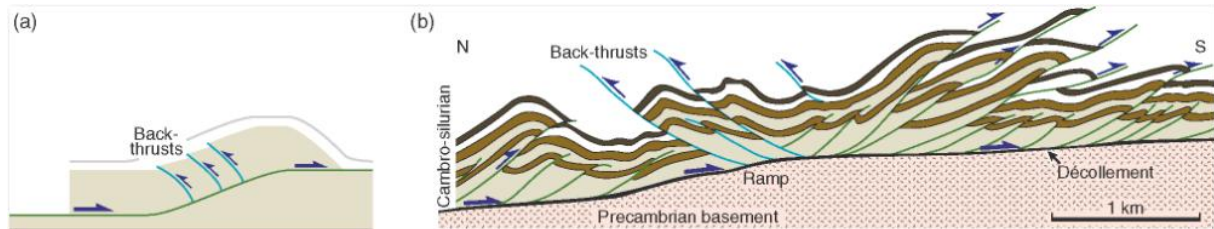


**Figure 2.3:**(a) Principal sketch of back-thrust formation, based on experiments and field observations. (b) Back thrusts generated above a ramp in the Caledonian sole thrust. The main thrusting direction is forward to the right. North of Oslo, Norway. Based on Morley (1986). (From Fossen, 2010).

### 2.3 Extensional regimes

Extensional faults have received lot of attention since the 1980's, when it came to knowledge that a number of faults that were previously thought to be thrust faults actually were low-angle extensional faults. Extensional faults are found in many places and are widespread in orogenic belts. Also, extensional faults are interesting regarding the petroleum industry, as many hydrocarbon resources are found in rift settings controlled by normal faults. Extensional faults generally show displacements smaller than thrust faults, but low-angle extensional detachments can still have offsets up to a hundred kilometers or so, e.g. the Nordfjord-Sogn Detachment (Norton, 1986).

#### *The domino model*

When parts of the upper crust are extended, rotated fault blocks tend to form. The fault blocks are arranged and rotated to look like domino bricks (Figure 2.4), hence the name *domino model*. Ideally, there is no internal strain in each rotated fault block, and all faults have the same dip, offset, rotation and rotation rate. The Gullfaks Field in the northern North Sea consists of such a domino system, limited by a horst complex to the east (Fossen, 2010).

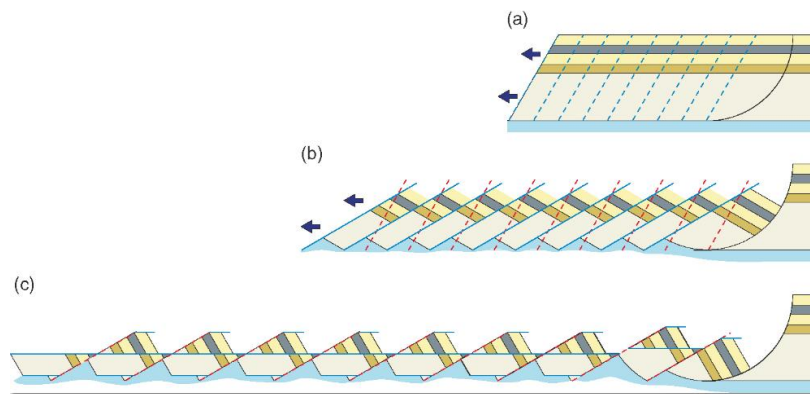


**Figure 2.4:** Schematic illustration of the development of a domino system. (a) The transition to the undeformed footwall is accommodated by a listric fault. (b) A new set of faults develops at high extension. (c) The resulting fault pattern can become quite complex. (From Fossen, 2010).

### ***Horst and graben complexes***

Fault zones are defined as multiple faults or slip surfaces close enough to each other to define a zone. There are different scenarios of faults in a zone, for instance *grabens* and *horst*. Where two separate normal faults are dipping towards each other and the block in between them is lowered, it is called a graben. Horst on the other hand is defined as two separate normal faults dipping away from each other, and the block in between them is elevated.

Some faults are bigger than others in a faulted area, and the largest faults are often referred to as *master faults*. Commonly, *minor faults* are associated with a master fault, referred to as *antithetic-* or *synthetic faults*, based on their dip direction: antithetic faults dips toward the master fault, while synthetic faults dips in the same direction as the master fault (Fossen, 2010).

## **2.4 Geological analogue**

In order to make the synthetic seismic modeling as realistic as possible, representative well log values from the Draupne Formation, Dunlin Group., Statfjord Formation and Brent Group have been used. The well logs have been provided by Statoil ASA, in form of three different wells displayed in Appendix A.

Based on the well logs, approximate mean values of velocities and densities were chosen for use in the synthetic seismic modeling (Table A.1), also displayed in Appendix A. In the following, a brief introduction of each stratigraphic unit is made.

### ***The Draupne Formation***

The Draupne Formation of Upper Jurassic age is located in the North Viking Graben. In regards to source rocks, the Draupne Formation is one of the most studied ones and also the source of most oils in the North Sea (Keym et al., 2006). The black shales found in the Draupne Formation are highly radioactive, and according to Vollset and Doré (1984) having values of ~185 API. The shales are inter-bedded with siltstones and sandstones, making the gamma ray response lower than for a clean shale. However, the gamma ray log in Appendix A displays a much lower average value (~75 API, and maximum value of 150 API) for the Draupne Formation shales than what Vollset and Doré (1984) suggested.

### ***The Brent Group***

The Brent Group, of Middle Jurassic age, is located in the northern part of the North Sea, more specifically at the western margin of the Viking Graben. The Brent Field in itself comprises two reservoirs; The Brent Group and the Statfjord Formation, both being excellent reservoirs. The Brent Group is divided into five different formations, from bottom to top being (1) Broom; (2) Rannoch; (3) Etive; (4) Ness and (5) Tarbert, which spells BRENT using the first letters in each formation. These formations vary lithologically from fine-grained to coarse-grained sandstones, mudstones, siltstones and coals (Struijk & Green, 1991).

### ***The Dunlin Group***

The Lower Jurassic Dunlin group consists of five different formations of Late Sinemurian - Toarcian age; (1) Johansen Formation (sandstone unit); (2) Amundsen Formation (shale unit); (3) Burton Formation (shale unit); (4) Cook Formation (sandstone unit) and (5) Drake Formation (shale unit). All of these formation, except the Johansen Formation on the Horda Platform, is found on the western and eastern sides of the North Viking Graben (Marjanac & Steel, 1997). The alternation of sands and shales are easily recognized in the gamma-ray log in Appendix A, as it fluctuates a lot.

### ***The Statfjord Formation***

The Statfjord Formation of Lower Jurassic/Triassic age is located in the northern part of the North Sea. It consists of 180-200 meters of sandstones that was deposited in an alluvial environment (Fossen & Hesthammer, 1998).

## 3 Geophysical background theory

### 3.1 Introduction

This chapter explains the basics of wave propagation and the physical principles that goes along with it. Different elastic moduli will be discussed, as well as the different types of seismic waves and velocities. Furthermore, reflectivity at rock interfaces will be mentioned in addition to seismic imaging with a main focus on pre-stack depth migration (PSDM).

#### 3.1.1 Stress, strain and elastic moduli

When a rock body is subjected to a force of any kind, it reacts by building up balanced internal forces. *Stress* is the term used as a measure of the intensity of these balanced internal forces (Kearey, Brooks, & Hill, 2002), and can be divided into two separate components. These are *shear-* and *normal stress* which acts parallel and perpendicular to the surface of a rock, respectively. When a rock body is subjected to stress, any change in volume or shape is described by the *strain*. Depending on the amount of stress, the rock may (1) return to its original form (elastic field), (2) be permanently deformed (ductile field) or (3) get fractured as the stress is removed (fracture point). Point (1) represents the linear elastic stress field (see Figure 3.1) which is the domain relevant for elastic and seismic waves.

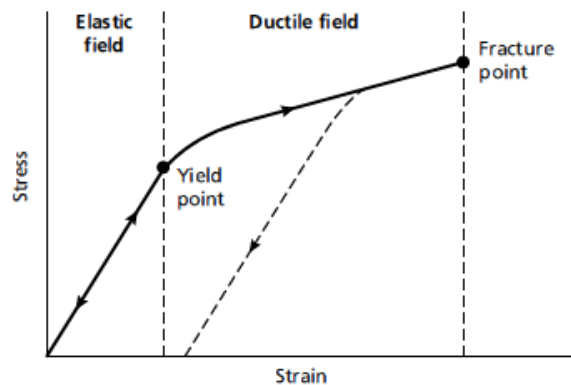


**Figure 3.1:** A typical stress-strain curve for a solid body (From Kearey, Brooks, & Hill, 2002).



The relation between stress  $\sigma$  and strain  $\varepsilon$  within the elastic field is described by Hooke's law

$$\sigma = c\varepsilon \quad (3.1)$$

where  $c$  denotes the elastic moduli of a rock material, i.e. its stiffness. Typical elastic moduli used are the Young's modulus, Poisson's ratio, bulk modulus and shear modulus, which is described in the following.

The linear relationship between stress and strain in a body/material is often expressed by *Young's modulus*, where  $F$  is the stretching force,  $A$  is the cross-section area,  $l$  is the original length and  $\Delta l$  is the length after stretching.

$$E = \frac{\text{longitudinal stress } F/A}{\text{longitudinal strain } \Delta l/l} \quad (3.2)$$

When a rod is stretched, the diameter  $d$  of the rod will decrease by a decrement  $\Delta d$ . The ratio between the lateral and longitudinal strain is described by *Poisson's ratio*  $\sigma$ .

$$\sigma = \frac{\text{lateral strain } \Delta d/d}{\text{longitudinal strain } \Delta l/l} \quad (3.3)$$

The *rigidity* or *shear modulus*  $\mu$  of a body is defined as the ratio between the shear stress ( $\tau$ ) and the shear strain ( $\tan\theta$ ).

$$\mu = \frac{\text{shear stress } \tau}{\text{shear strain } \tan\theta} \quad (3.4)$$

The *incompressibility* or *bulk modulus*  $K$  is defined as the stress-strain ratio where a cubic shaped body undergoes a hydrostatic pressure change  $\Delta P$  and the resultant volume strain is given by the volume change  $\Delta V$  divided by the original volume  $V$ .

$$K = \frac{\text{volume stress } \Delta P}{\text{volume strain } \Delta V/V} \quad (3.5)$$

### 3.1.2 Seismic waves and seismic velocities

When seismic sources, such as explosions, earthquakes or air guns from a seismic vessel occurs within or at the Earth's surface, some of the energy that is released takes the form of *elastic waves* that travel through the Earth's interior. There are two types of elastic waves, surface waves and body waves, where the latter will be further explained.

#### *Body waves*

There are two different types of body waves; longitudinal waves (P-waves) and transverse waves (S-waves), which travel through the Earth (Figure 3.2).

*P-waves* deforms the rock as it travels through by compressing and dilating different parts of the rock body, analogous to how a sound-wave would propagate through air. The particle motion is parallel to the propagating wave direction, which leads to changes in the rock volume.

*S-waves* deforms a rock in a transverse matter,- where the particle motion is perpendicular to the propagating direction. This movement leads to a change only in the shape of the rock body, making it oblique.

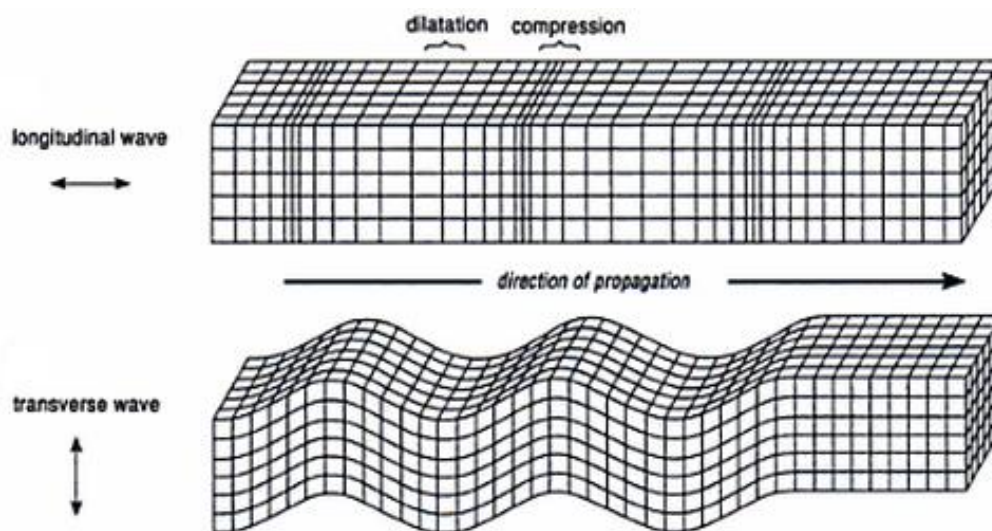


**Figure 3.2:** Longitudinal and transverse waves in rocks (From Fowler, 1990).

***Body wave velocities and lithology***

The elastic moduli described in section 3.1.1 and density controlling seismic velocities has a functional relationship to the rock microstructure and its geological properties like porosity, lithology and fluid saturation. In addition, one can use this information to convert seismic travel-time into depth measurements.

Rocks essentially consist of (1) connected mineral grains called the matrix and (2) a pore volume with porosity  $\phi$  which fluids may occupy. If the matrix consists of a mixture of non-uniform minerals, one may use an average of their constituent properties. As such, the bulk density of a rock can be accurately expressed through the simple relation

$$\rho_b = \rho_f \phi + (1 - \phi)\rho_m \quad (3.6)$$

where  $\rho_b$ ,  $\rho_m$  and  $\rho_f$  is the effective density, matrix density and pore fluid density, respectively (Kearey et al., 2002).

In isotropic and homogeneous rocks where the elastic and seismic properties are the same in any given direction, the P- and S-wave seismic velocities can be respectively expressed through the following formulas.

$$V_P = \sqrt{\frac{\kappa + \frac{4}{3}\mu}{\rho}} \quad (3.7)$$

and

$$V_S = \sqrt{\frac{\mu}{\rho}} \quad (3.8)$$

where  $\mu$  is the shear modulus,  $\rho$  is the density and  $\kappa$  is the bulk modulus.

As such, the shear and bulk modulus of the rock can be derived via

$$\mu = \rho V_S^2 \quad (3.9)$$

and

$$\kappa = \rho V_P^2 - \frac{4}{3}\mu \quad (3.10)$$

Since the bulk modulus  $\kappa$  is always positive,  $V_P$  is always larger than  $V_S$ . Thus, the P-waves always travel faster than the S-waves. The shear modulus is always zero for any fluid, thus the S-waves cannot propagate through fluids, such as the ocean or the outer core in the Earth's interior (Fowler, 1990).

By doing velocity studies in the laboratory, some key observations have been made. (1) P-wave velocities increase with confining pressure; (2) Due to cementation and progressive compaction, shale and sandstone velocities show an increase with burial depth and age; (3) The density and P-wave velocity can be related in many sedimentary rocks, hence you can predict the density of subsurface layers by examining their seismic velocity; (4) Elastic moduli,  $V_P/V_S$ -ratio and Poisson's ratio is reduced when gas is present in sedimentary rocks.  $V_P/V_S$ -ratios larger than 2 points to unconsolidated sands, while ratios smaller than 2 points to either a consolidated sandstone or an unconsolidated gas-filled sand (Kearey et al., 2002).

### ***Velocity and density relations***

Bulk rock density ( $\rho_b$ ) is directly related to the mineral density and porosity. In well-log analysis, velocity-porosity transforms are used, in which velocity-density relationships can be obtained (the best known being the Wyllie's time-average equation). One of the most important equations which expresses density in terms of velocity for an average of all rock types is the Gardner, Gardner, and Gregory (1974) equation

$$\rho_b = 1.741 V_P^{0.25} \quad (3.11)$$

where  $V_P$  is expressed in km/s. The Gardner equation fits a variety of different velocities and porosities of rocks and therefore takes into account the variations in consolidation and effective stress of a rock. The Gardner equation tends to underestimate and overestimate the density of shales and sandstones, respectively, but the lithologic variations may be taken into account by using different variants of the Gardner equation for each lithology.

### **3.1.3 Attenuation of seismic energy in homogeneous media**

As seismic waves propagate through the Earth's interior, their energy  $E$  will gradually decrease. There are three different reasons for this energy loss: (1) *Geometrical spreading*, (2) *Intrinsic absorption* and (3) *Transmission losses*, which is described in section 3.1.4, as it is only relevant where there is a layered medium with varying properties.

In a homogeneous media, geometrical spreading is attenuation of energy due to being

distributed over a spherical wave front with increasing radius. The amount of energy in an area of the spherical wave front is given as  $E/4\pi r^2$ , if the radius of the wave front is  $r$ . The rays energy decreases with  $1/r^2$  as the distance increases along the ray path, due to geometrical spreading of the energy. Since wave amplitude is proportional to the square root of wave energy, it decreases by  $1/r$ . Geometrical spreading also occurs in heterogeneous media, but the wave front will not be spherical.

The second cause of energy attenuation along a ray path is intrinsic absorption. The energy loss is due to internal friction, which may lead to total loss of the seismic disturbance. The proportion of energy that is lost during transmission through a distance is equivalent to the wavelength  $\lambda$ , and is termed *the absorption coefficient*  $a$ . The absorption coefficient ranges from 0.25 to 0.75  $\text{dB}\lambda^{-1}$  for common Earth materials. Thus, two pulses of different frequencies travelling the same distance, will lead to attenuation of the highest frequency (shorter wavelength) more rapidly than a pulse with low frequency (Kearey et al., 2002).

#### **3.1.4 Ray paths in layered media**

Since different rocks have different physical properties, there will be a change in the propagating velocity at layer interfaces. The incident seismic energy is partitioned into transmitted and reflected energy, and the respective amplitudes are attenuated at every interface it encounters. This phenomenon is known as transmission losses, and the amplitude of the transmitted and reflected pulses are dependent on the velocity and density between the interfaces and the incident angle of the seismic pulse.

##### ***Reflection and transmission of normally incident seismic rays***

A normally incident P-wave with amplitude  $A_0$  meets an interface between two layers with different densities and velocities. The P-wave will form a reflected- and transmitted ray of amplitudes  $A_1$  and  $A_2$ , respectively, where the reflected ray propagates in the opposite direction of the incident ray, and the transmitted ray travels through the interface and continues in the same direction as the incident ray (Figure 3.3).

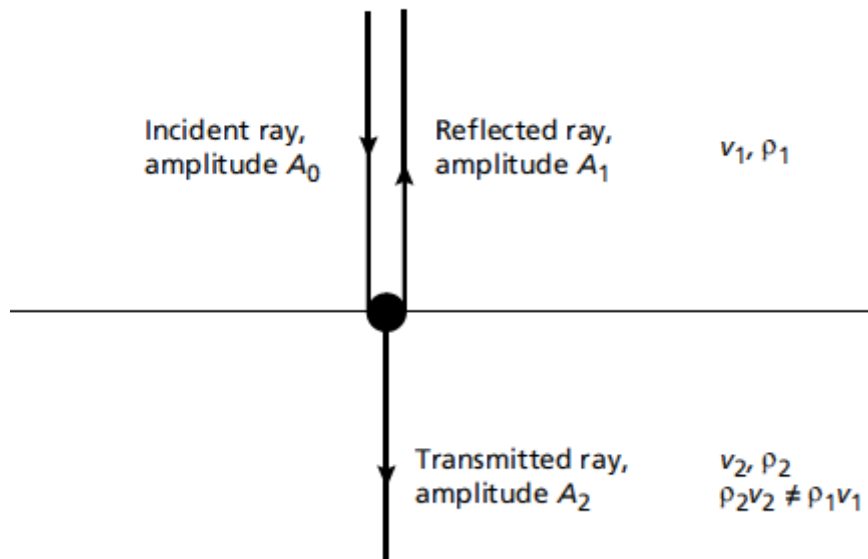


**Figure 3.3:** Reflected and transmitted rays related to a ray of normal incidence on an interface of acoustic impedance contrast. (From Kearey et al., 2002).

The energy of the reflected and transmitted ray equals the energy of the incident ray. How much of the energy that is reflected and transmitted depends on the acoustic impedance  $Z$  across the interface, which again depends on the rocks density and velocity.

$$Z = \rho v \quad (3.12)$$

where  $\rho$  and  $v$  are the density and velocity of a rock, respectively.

A general rule is that, harder rocks, have higher acoustic impedance. Where you have a small contrast in acoustic impedance across an interface, the amount of energy transmitted is higher than the energy reflected. Also, where the acoustic impedance contrast is high, the amount of energy reflected is higher than the energy transmitted. In order to measure the amount of reflected energy across an interface, the *reflection coefficient*  $R$  is used and given by

$$R = \frac{A_1}{A_0} \quad (3.13)$$

where  $A_1$  and  $A_0$  are the amplitudes of the reflected and incident ray, respectively.

### ***Reflection and transmission of oblique incident seismic rays***

As in the case of normally incident rays, reflected and transmitted P-waves are generated at interfaces where the incident ray is oblique. In addition, some of the incident seismic energy from the P-wave generates refracted (transmitted) and reflected S-waves (Figure 3.4).

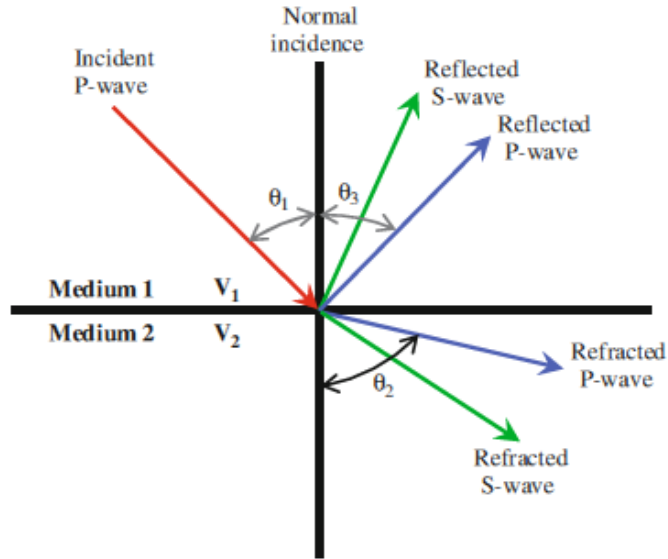


**Figure 3.4:** A schematic diagram of reflected and refracted waves generated from an incident P-wave. The angle between the normal to the interface of two media and an incident P-wave is the angle of incidence ( $\theta_1$ ), and is equal to the angle of reflection ( $\theta_3$ ) in isotropic media. The angle of refraction ( $\theta_2$ ) depends on the velocity of the wave in that medium (From Bjorlykke, 2010).

When the incident P-wave encounters the interface, the transmitted P-wave travels through the underlying layer with a different angle, and is termed a *refracted ray*. In this case, *Snell's Law of Refraction* applies, where Snell defined a *ray parameter*  $p$ .

$$p = \frac{\sin\theta}{v} \quad (3.14)$$

where  $\theta$  is the inclination angle of the ray and  $v$  is the velocity of the layer it travels through.

When applying Snell's Law for a refracted P-wave shown in Figure 3.4, it states that

$$\frac{\sin\theta_1}{v_1} = \frac{\sin\theta_{r1}}{v_1} = \frac{\sin\theta_2}{v_2} \quad (3.15)$$

where  $\theta_1$ ,  $\theta_{r1}$  and  $\theta_2$  are the angles of incidence for the incident-, reflected- and refracted ray, respectively.

When the lower layer (Medium 2) in Figure 3.4 has a higher velocity than the overlying layer (Medium 1), the incident ray is refracted away from the interface. Thus, a certain incident angle will cause a refraction of  $90^\circ$ , making the ray travel along the interface with a higher velocity. This phenomenon is called *critical refraction*, and the corresponding incident angle is called the *critical angle*  $\theta_c$ . This means that any angle larger than the critical angle will lead to total reflection of the incident P-wave energy. The critical angle formula is calculated by

$$\frac{\sin\theta_c}{v_1} = \frac{\sin 90^\circ}{v_2} = \frac{1}{v_2} \quad (3.16)$$

thus

$$\theta_c = \sin^{-1}\left(\frac{v_1}{v_2}\right) \quad (3.17)$$

The reflection coefficient for non-normal incidence rays are more complicated to derive than in cases of normal incidence rays as seen previously. This is due to mode conversion between P- and S-waves described by the Zoeppritz equations (see Zoeppritz (1919) for details). The equations are used to determine the amplitudes of reflected and refracted rays for incident P-waves at a planar interface as a function of angle, known as *angle dependent reflectivity*.

When discussing transmission and reflection, it is assumed that the interfaces between two layers are relatively planar and continuous. As this is not always the case, since abrupt discontinuities often are present, the laws of refraction and reflection does not apply. This is because the curvature radius is shorter than the wavelength of the incident waves. *Diffraction* is the name of *radial scattering* of incident seismic energy, which occur for instance at edges of faulted layers in the subsurface (Figure 3.5). Diffraction is common, but can be difficult to discriminate from refracted and reflected pulses on seismic records.

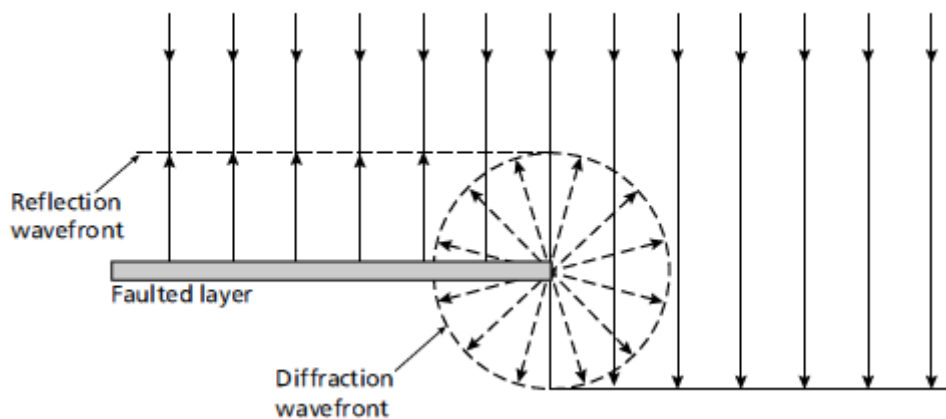


**Figure 3.5:** Diffraction caused by the truncated end of a faulted layer. (From Kearey et al., 2002).



## 3.2 Geophysical exploration

When investigating the Earth's interior, geophysical exploration is of great importance. Both in the search for mineral resources and hydrocarbons, various exploration equipment is crucial to get a proper image of subsurface structures, and seen from an economic perspective it is critical. This sub-chapter will briefly discuss the survey methods of importance to this study.

### *Seismic surveying*

Seismic surveying is probably the most important geophysical exploration method there is, and was first introduced in the 1920's. Here, a controlled source will generate seismic waves that propagate through the Earth's subsurface. The waves will either be reflected or refracted at geological subsurface boundaries, and measuring equipment at the surface will detect the travel times and ground motions caused by these waves. The travel times may be converted into depth values if needed, and different geological features and structures can be mapped and interpreted (Kearey et al., 2002).

#### 3.2.1 Seismic reflection survey

Seismic reflection surveying is the most used geophysical exploration method today and is highly valued in the petroleum industry. Seismic energy pulses are reflected at subsurface interfaces and recorded at the surface. The main purpose of a seismic reflection survey is to collect data of reflected pulses with varying distance to the source. Since velocity not only varies vertically, these surveys are commonly carried out where layers are shallowly dipping. Raw seismic data is collected, processed and displays a seismic section of the subsurface when completed. A seismic section is fundamentally different from a depth section, and only by fully understanding how seismic reflections work a geologist can make its interpretations.

#### *2D and 3D surveying*

A *two-dimensional survey* (also called *reflection profiling*) provides a lower degree of resolution than a three-dimensional survey. In two-dimensional surveys, data is collected along survey lines that consist of shot points and receivers. The path of the reflected rays are assumed to lie beneath the survey line in the vertical plane, which implies that when layers are dipping in the cross-line direction, the resultant seismic section will not display a real subsurface image. 2D surveys are thus limited and only adequate when mapping structures like cylindrical faults and folds where the geometry remains the same along strike.

When it comes to source-receiver configurations in a 2D survey, the *single-ended*

*spread* and the *split spread* are most common. Using single-ended spread, the receivers are located at one side of the shot point, which is the preferred configuration in marine surveys. The split spread places the receivers on both sides of the shot point, and is mostly used for land surveys (Figure 3.6).

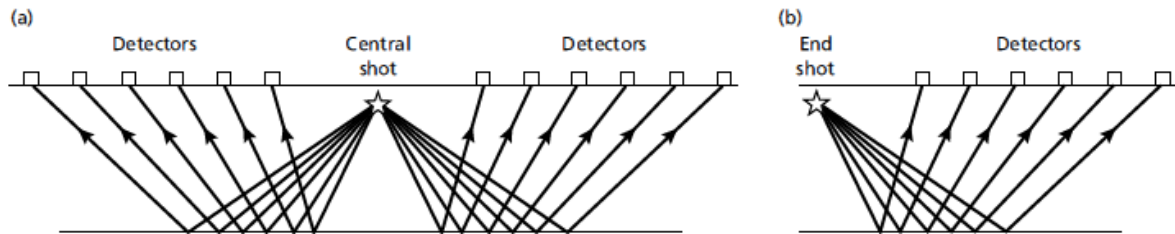


**Figure 3.6:** Shot-detector configurations used in multichannel seismic reflection profiling. (a) Split spread (b) Single-ended spread. (From Kearey et al., 2002).

In *three-dimensional surveys*, the field data is collected in a way that the recorded arrivals are not limited to rays that have travelled in a single vertical plane. Thus, arriving rays from outside the vertical plane are also recorded. The shots and receivers are placed so that arrivals at each receiver is sorted into a representation of reflected rays from each interface. Hence, a 3D survey samples a volume of the subsurface as opposed to a profile-area sampling in 2D surveying. Also, using a 3D survey, a horizontal slice, known as a *time-slice*, can be constructed (Figure 3.7).

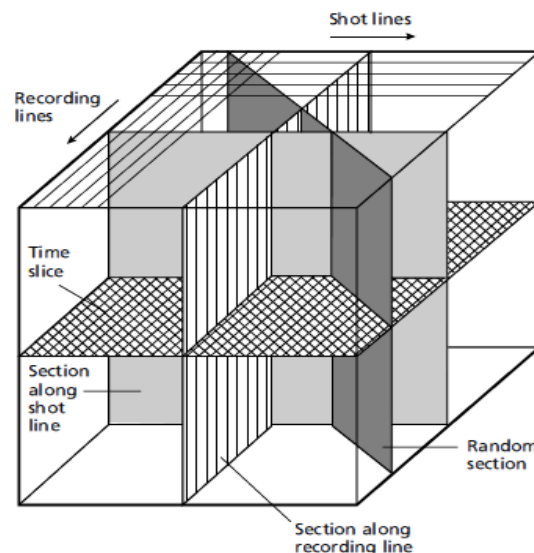


**Figure 3.7:** The reflection data volume obtained from a three-dimensional seismic survey. By taking vertical slices through this data volume, it is possible to generate seismic sections in any azimuthal direction; by taking horizontal slices (*time slices*), the areal distribution of reflection events can be studied at any two-way reflection time (From Kearey et al., 2002).

A 3D marine survey can be conducted in two different manners. The first one comprises collecting three-dimensional data along parallel vessel tracks where the streamer is towed obliquely behind the vessel. This way, it covers a swath of the seafloor so that when adjacent vessels cover swaths of the seafloor which overlap, areal coverage of the subsurface reflectors is provided. The second survey alternative is referred to as the *dual source array method*, where sources are placed on each side of the hydrophone streamer and fired alternately (Figure 3.8). Additionally, one can use several streamers to get a wider and denser fold of 3D data (Kearey et al., 2002).

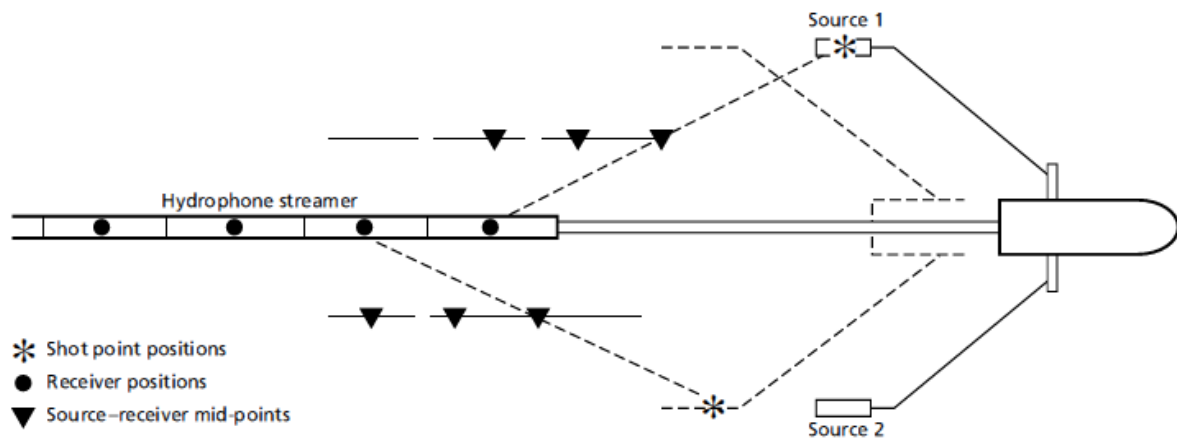


**Figure 3.8:** The dual source array method for gathering marine seismic data in 3D. Sources 1 and 2 fire alternately towards the streamer and thus create two parallel sets of source-receiver midpoints. (From Kearey et al., 2002).

### ***Strike and dip streamer shooting for 3D multi-streamer acquisition***

There are not many published experiments on conducting "strike" and "dip" 3D surveys over the same structure. Some say that acquiring data in the dip direction yields better data compared to strike direction acquisition, which is mainly due to the fact that the cross-line CMP (common mid-point) spacing is coarser than the inline sampling. Still, there are advantages and disadvantages when acquiring data both in the strike direction and dip direction.

Deciding the appropriate shooting direction has always been an issue, but there are a few recently established key issues one can follow: (1) Survey cost and logistics regarding the operation, (2) the illumination coverage of the target, (3) data resolution and imaging quality and (4) processing practicalities.

As for the study in this thesis, the most ideal seismic experiment combine high quality illumination of the subsurface and dense spatial sampling. By choosing the correct shooting strategy, the differences observed between "strike"- and "dip" shooting may be prevailed (Long, Ramsden, & Hoffmann, 2004).

Several publications regarding multi-streamer shooting direction have been made (Durrani, French, & Comeaux, 1987; Egan, Dingwall, & Kapoor, 1991; Manin & Hun, 1992), and there are some common features to be noted. In general, variations in the lateral velocity can cause strong variations in transmission losses and geometrical spreading (section 3.1.4) when shooting in dip direction. In regards of illumination, dipping structures are shown to be more regular when shooting in the strike direction, whereas ray paths can be more complicated when shooting in the dip direction. Also, a common feature regards different obstacles like logistics, cost, acquisition technology, resolution and processing.

### ***Seismic equipment***

As mentioned, in any seismic survey there has to be some kind of source and receiver. In marine surveys, the most common source is the air gun. The air gun releases highly compressed air into the surrounding water as it is towed behind a vessel at 5-15 meters depth. One can use only one air gun or an array of air guns, termed *tuned array*, which are several air guns of different sizes combined.

*Hydrophones* or *geophones* are used as receivers for the seismic signals generated by the air gun and is used to detect pressure changes in water. Several hydrophones are combined to form *streamers* that are also towed behind the vessel. A streamer is 4 - 6 km long, where each receiver is ~75 meters long and contain 96 hydrophones grouped in arrays of 12.5 - 25 meters (Bjorlykke, 2010).

### **3.2.2 Displaying seismic reflection data**

As hydrophones and geophones measure the energy reflected at subsurface boundaries, they are converted into an electrical signal displayed as a *seismic trace* (Figure 3.9). One or more of the seismic traces can be plotted next to each other in a *seismogram*, where the vertical axis and the horizontal axis represent travel-time and source-receiver distance, respectively.

Figure 3.9 shows the relationship between geological layering, acoustic impedance and reflection coefficient as a function of depth. The receivers at the surface detects reflected pulses which are scaled in amplitude based on the travelled distance and the reflection

coefficients of the layer boundaries of the subsurface. The pulses will arrive at different times depending on the boundary depths and the propagating velocities between them. Again, assuming that the shape of the pulses does not change during its travel through the layered subsurface, the resulting seismic trace can be regarded as a convolution. The input pulse is convolved with a time series (*reflectivity function*) composed of a series of spikes. Each of the spikes will have amplitudes directly related to the reflection coefficient and the two-way reflection time of a boundary, which represents the *impulse response* of the layered subsurface (the output for a spike input). As the pulses propagate it elongates due to loss of higher frequencies by absorption. Then, the seismic trace may be regarded as a convolution of the reflectivity function with a *time-varying* seismic pulse. Due to noises of different variants, seismic traces can be difficult to recognize without proper processing techniques (Kearey et al., 2002).

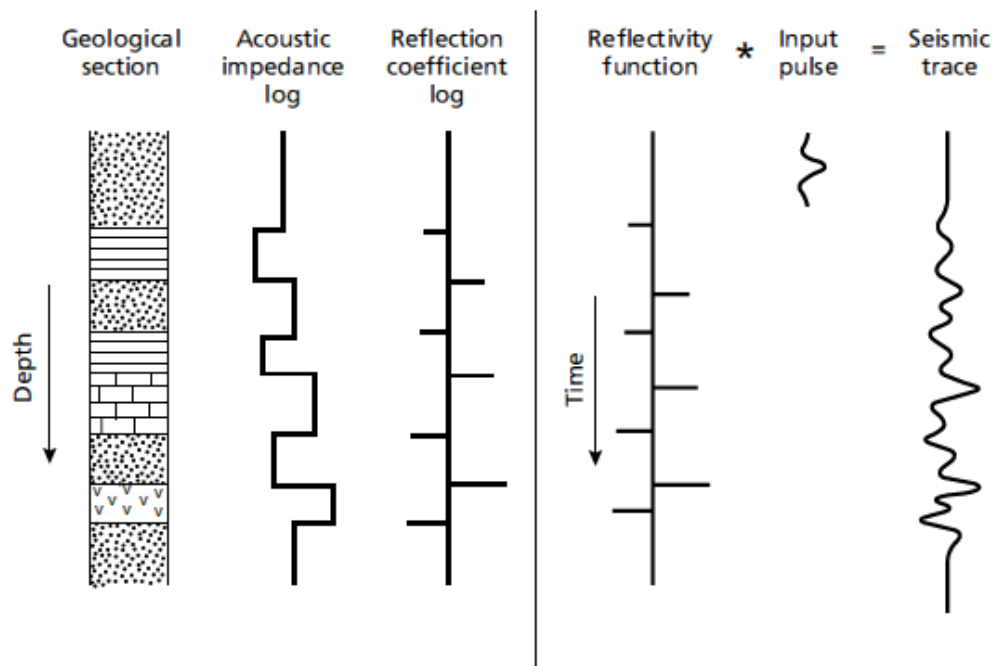


**Figure 3.9:** The convolutional model of the reflection seismic trace, showing the trace as the convolved output of a reflectivity function with an input pulse, and the relationship of the reflectivity function to the physical properties of the geological layers (From Kearey et al., 2002).

### 3.2.3 Seismic resolution

When it comes to the seismic method, the ability to resolve small anomalies is limited. When speaking of small anomalies, one refers to the *seismic wavelength*, which is given by

$$\lambda = v/f \quad (3.18)$$

where  $v$  is the ratio of phase velocity and  $f$  is the temporal frequency. A rock's seismic velocity cannot be changed, but the seismic wavelength can be changed by altering the temporal frequency. Hence, by increasing the frequency the wavelength will reduce and improve both the vertical and horizontal resolution (Lines & Newrick, 2004).

A measure of how large an object need to be in order to be seen in seismic data is termed *seismic resolution*. Based on the wavelength of the sound-wave from the originating source, the *vertical resolution* is calculated by  $\lambda/4$ . Layers can be discerned when their thickness is below  $1/4$  wavelength, but one can also detect layers down to  $1/32$  wavelength (Rafaelsen, 2006).

*Horizontal resolution* describes how small a spatial anomaly can be and still be resolved on seismic data. This is directly related to the Fresnel zone, which is the subsurface area where energy is collected to cause a seismic reflection (Figure 3.10). The horizontal resolution is also controlled by the detector spacing in a seismic reflection survey, where decreasing detector spacing increases the resolution (Kearey et al., 2002). The diameter of the Fresnel zone changes due to offset changes between the source and receiver both in inline and horizontal dimensions, and a smaller Fresnel zone width implies a better resolution. Also, the Fresnel zone alters in shape when the reflection surface is not a plane. In two dimensions, the Fresnel zone shrinkage is only in the seismic profile direction, leaving a Fresnel zone that is elliptical. This means that the horizontal resolution is directional and dependent on the orientation of the seismic line and subsurface features, and may not show the horizontal features of interest. This problem can easily be avoided by using three dimensional data and migration (Lindsey, 1989).

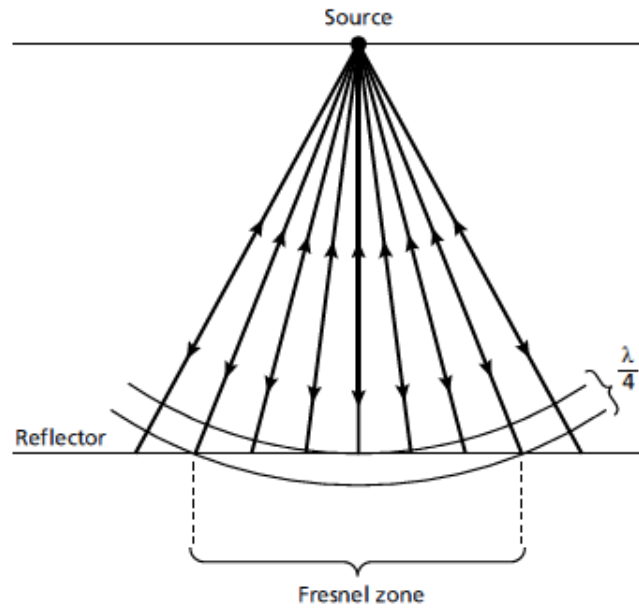


**Figure 3.10:** Energy is returned to source from all points of a reflector. The part of the reflector from which energy is returned within half a wavelength of the initial reflected arrival is known as the Fresnel zone (From Kearey et al., 2002).

### 3.3 Seismic processing

After completing seismic data acquisition, *seismic processing* is conducted. This involves a series of processing steps carried out on the raw seismic data, and the purpose is to construct a sectional slice of the subsurface in the most realistic way possible.

#### 3.3.1 Basic processing

There are some typical steps to seismic processing which usually comprises pre-processing, CMP sorting, deconvolution, muting, velocity analysis, NMO correction, stacking and migration (the latter being shortly presented in this sub-chapter). The order in which these steps are conducted are not the same for all seismic data sets and will be established based on testing of selected parts of the data set, the purpose of investigation, quality and cost.

#### *Migration*

If a reflector is not horizontal, the displacement of the position and shape of the reflector is corrected and termed *migration*. Migration is a basic seismic processing step performed on seismic data, and is fairly complicated compared to others. Still, migration can be performed both in the time domain and depth domain, depending on the purpose of use.

*Time migration* displays the vertical dimension as time, while *depth migration* displays the vertical dimension as depth, after the reflection times are converted into reflector

depths. This can only be done when using appropriate velocity information. Time- and depth migration can be performed either after or before stacking NMO corrected data, and are thus called *post-stack migration* or *pre-stack migration*, respectively (Kearey et al., 2002). More detailed information on migration is found in the following sub-chapter.

### 3.4 Seismic imaging

#### 3.4.1 Post-stack migration

In post-stack migration, a flat, horizontal and homogeneous model is assumed. Stacked seismic traces are plotted along the vertical time axis, which yields an untrue depth model. To correct the differences between time and depth, post-stack migration is used by linking together time- and space-coordinates through the wave-equation (see Gelius and Johansen (2010) for details).

#### 3.4.2 Pre-stack depth migration (PSDM)

When lateral velocity variations are considerable enough to make a non-hyperbolic moveout, *pre-stack depth migration* is needed. Therefore, performing migration directly in depth from the pre-stack data where there are various dips and lateral velocity variations, is necessary. Also, interval velocities is found by using pre-stack depth migration. This sub-chapter is mainly based on the article "Resolution and illumination analysis in PSDM: A ray-based approach" by Lecomte (2008).

#### *Resolution and illumination analyses in PSDM*

Angle-dependent depth images of the subsurface reflectivity is the ultimate goal when it comes to seismic processing, and pre-stack depth migration attempts to do so, despite some limiting factors. Instead of the grounds reflectivity being retrieved as detailed as possible, the waves identify the reflectivity of structures being blurry or not noticeable at all. Hence, the true reflectivity is filtered, and by estimating these filters the resolution of subsurface structures may be good enough to properly interpret.

#### *Scattering isochrones*

To compensate for wave propagation effects between sources and receivers down to each image point (IP), a background velocity field is needed. Figure 3.11 below illustrates the travel time information  $t_S$  and  $t_R$  for a given source/receiver pair SR, respectively, to the image points by showing the consequent wave fronts.



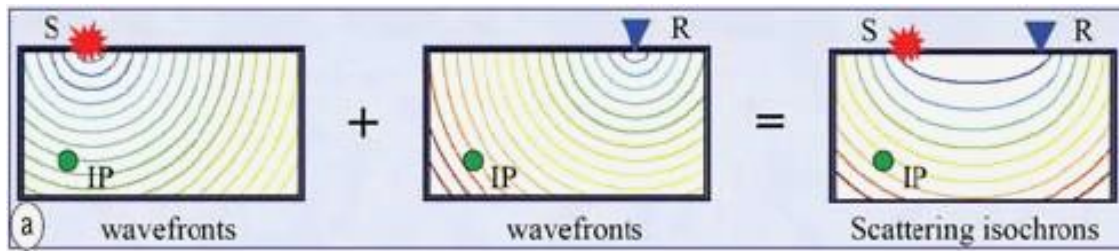


**Figure 3.11:** *Scattering isochrones in PSDM. (a) Isotropic case: formation of elliptic scattering isochrones in a homogeneous model as the sum of two traveltimes to get the scattering traveltime. These grids show circular wavefronts whose centers are shot  $S$  (red marker) and receiver  $R$  (blue triangles).  $S$  and  $R$  are the focal points of the elliptic scattering isochrones (Modified from Lecomte, 2008).*

The *scattering traveltimes*  $t_{SR} = t_S + t_R$  (meaning the backscattered energy at  $R$  due to  $S$ ) are needed at each image point in order to relate seismic energy recording time to depth. The isolines of  $t_{SR}$  are termed *scattering isochrones* and are elliptic in the isotropic homogeneous case (even though they are never elliptic in realistic cases).

### ***PSDM images and point-spread functions (PSF)***

When only one SR (source/receiver) pair is used (thus one trace), nonzero amplitudes along and near the corresponding scattering isochrones on the PSDM image will occur. If the source and receiver has zero-offset above the point scatterer (Figure 3.12a), a circle occurs at the PSDM image and has a constant thickness. Figure 3.12b also shows an elliptic pattern, only with a larger thickness which varies all over the scattering isochrone, due to an additional SR pair. In the case of several traces (several sources/receivers) in Figure 3.12c with zero-offset or as a common-shot recording in Figure 3.12d, the resulting PSDM image comes from superposition of the elementary impulse responses and interference at the point scatterer location. Figure 3.12c (zero-offset) and Figure 3.12d (common-shot recording) are very different, even though the same point scatterer and emitted pulse have been used.

The migration signature that occurs at the point scatterer is a result of interference and termed *point-spread functions (PSF)*. These signatures are shown in the recently discussed figures and depends on the source-receiver configurations.

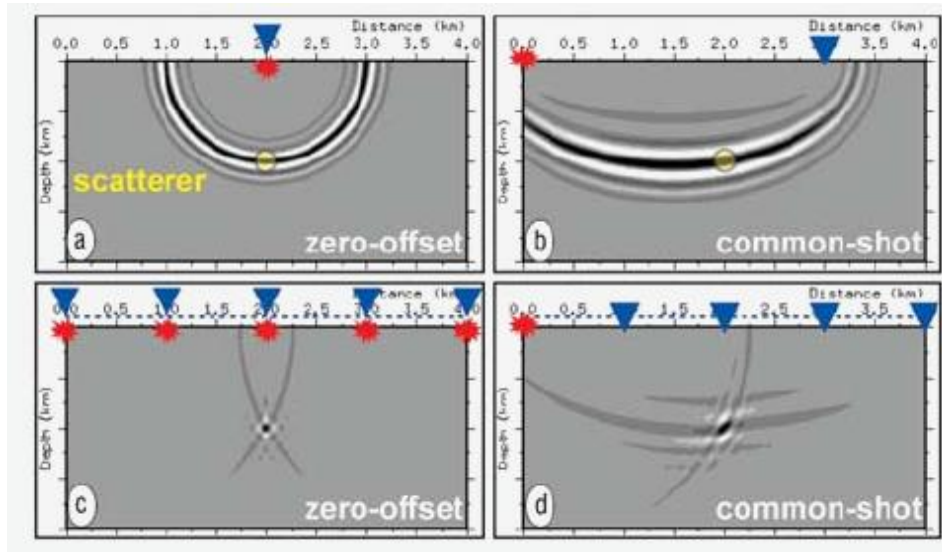


**Figure 3.12:** Scattering isochrones and PSDM. The background velocity model is homogeneous and isotropic. A point scatterer is located at the center of the image (yellow disk). Both a zero-offset survey (shot/receiver positions spread over 4 km) and a common-shot survey (one shot at 0 km and receivers along the same 4 km) are considered. (a) Zero-offset: PSDM image attached to one shot/receiver couple, i.e., the one just above the point scatterer. (b) Common shot: PSDM image attached to one receiver at 3 km. (c) Zero-offset: PSDM image attached to the whole zero-offset survey. (d) Common-shot: PSDM image attached to the whole common-shot acquisition (From Lecomte, 2008).

### ***Illumination vectors***

At a chosen image point in a background velocity model, the *illumination vector*  $\mathbf{I}_{SR}$  is defined (Figure 3.13a). Vector  $\mathbf{p}_S$  (attached to the incident wavefield) and vector  $\mathbf{p}_R$  (attached to the scattered wavefield) are known as *slowness vectors*, and the difference between them ( $\mathbf{I}_{SR} = \mathbf{p}_S - \mathbf{p}_R$ ) are shown in Figure 3.13b. In cases with no wave conversion and where the incident wave is the same type as the scattered one (P-or S-wave),  $\mathbf{I}_{SR}$  is calculated as follows

$$\mathbf{I}_{SR} = \mathbf{p}_R - \mathbf{p}_S = \frac{\hat{\mathbf{u}}_R - \hat{\mathbf{u}}_S}{V} = \frac{2\cos(\theta_{SR}/2)}{V} \hat{\mathbf{u}}_{SR} \quad (3.19)$$

where  $V$  is the incident and scattered waves velocity at the image point,  $\hat{\mathbf{u}}_S$  is a unit vector perpendicular to the incident wavefront from the source  $S$  and  $\hat{\mathbf{u}}_R$  is a unit vector perpendicular to the scattered wavefront towards the receiver  $R$ . The opening angle ( $\theta_{SR}$ ) between  $\hat{\mathbf{u}}_S$  and  $-\hat{\mathbf{u}}_R$  (Figure 3.13b) depends on the position of the  $SR$  pair and plays a very important role in regards to resolution, because it controls the length of  $\mathbf{I}_{SR}$ .

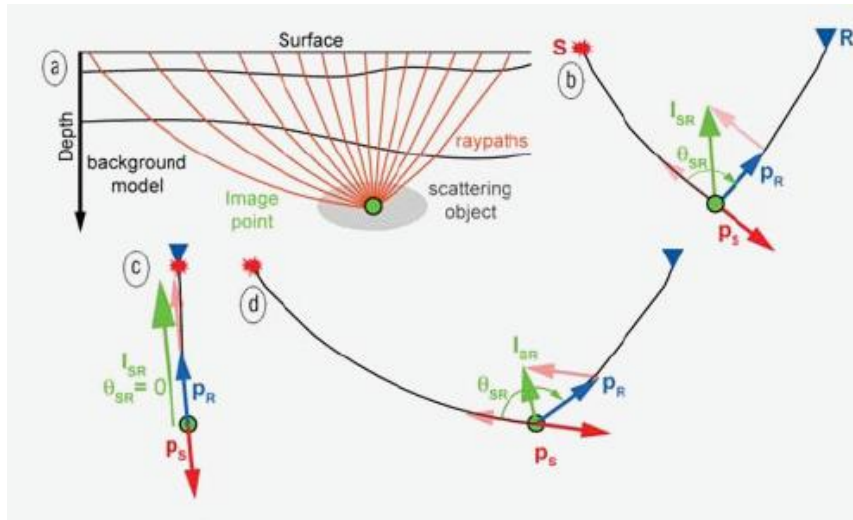


**Figure 3.13:** *Illumination vector (isotropic case without wave conversion). (a) Model with an unknown scattering object around one considered image point. Raypaths are drawn to illustrate the propagation effect in the background model. (b) Local definition of the illumination vector  $\mathbf{I}_{SR}$  as the difference of two slowness vectors, i.e.,  $\mathbf{p}_R - \mathbf{p}_S$ , where  $\mathbf{p}_S$  is attached to the incident wave (from source  $S$ ) and  $\mathbf{p}_R$  to the scattered wave (toward receiver  $R$ ).  $\theta_{SR}$  is the opening angle between  $-\mathbf{p}_S$  and  $\mathbf{p}_R$ . The orientation and size of  $\mathbf{I}_{SR}$  depend on the considered source/receiver couple and the propagation effect in the overburden: (c) Zero  $\theta_{SR}$  case, i.e., longest  $\mathbf{I}_{SR}$ . (d) Large  $\theta_{SR}$  case, i.e., small  $\mathbf{I}_{SR}$ . (From Lecomte, 2008)*

### **Scattering wavenumber vectors**

By multiplying  $\mathbf{I}_{SR}$  with the frequency  $\nu$ , the *scattering wavenumber vector* is derived:

$$\mathbf{k}_{SR} = \nu \mathbf{I}_{SR} = \nu(\mathbf{p}_R - \mathbf{p}_S) = \mathbf{k}_R - \mathbf{k}_S = \mathbf{k}_R \hat{\mathbf{u}}_R - \mathbf{k}_S \hat{\mathbf{u}}_S \quad (3.20)$$

where  $\mathbf{k}_S$  is a local plane wavenumber attached to the incident wave and  $\mathbf{k}_R$  connected to the scattered wave. Because of that,  $\mathbf{k}_{SR}$  and  $\mathbf{I}_{SR}$  is parallel and equal in length if  $\mathbf{I}_{SR}$  is multiplied by the frequency. In regards to resolution analysis,  $\mathbf{k}_{SR}$  is a key component since it defines a local plane wavefront tangent to the scattering isochrone (Lecomte & Gelius, 1998). This means that when  $\mathbf{k}_{SR}$  is mapped in the wavenumber domain, considering only one frequency, the corresponding image in the depth domain will be a monochromatic wavefront.

### **Scattering wavenumber and PSF**

For a set of selected SR pairs, all the  $\mathbf{k}_{SR}$  are calculated at one image point. This leads to an approximation of the superposition of scattering isochrones by mapping all the  $\mathbf{k}_{SR}$  in the wavenumber domain, followed by applying a Fourier transform to acquire the corresponding depth image. PSF is a function of the SR pairs used, but also depends on the background velocity model and frequency band. The PSFs in Figure 3.14 are very similar in shape to the PSDM images shown in Figure 3.12, but only in the vicinity of the point scatterer.

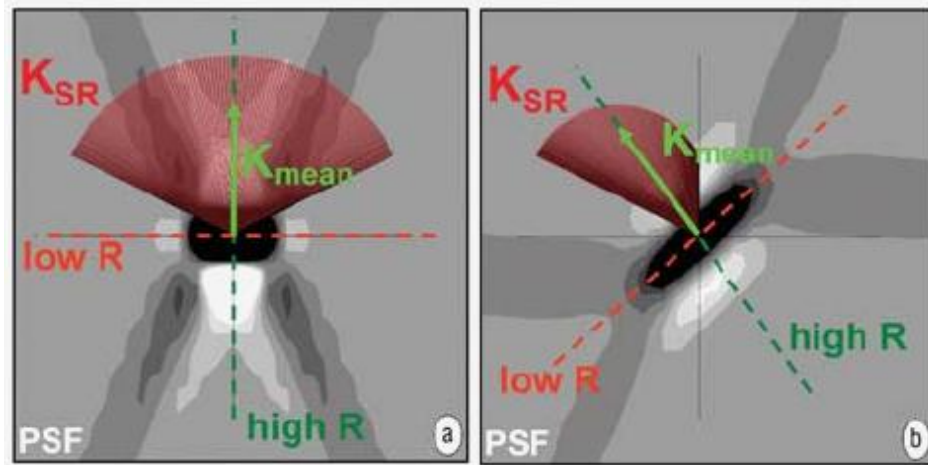


**Figure 3.14:** Scattering wavenumber vectors  $\mathbf{k}_{\text{SR}}$  superimposed on their corresponding PSF for the model used in Figure 3.12. (a) Zero-offset survey case. (b) Common-shot survey case. (a) and (b) are to be compared with Figure 3.12b and d at the location of the point scatterer, respectively. The mean  $\mathbf{k}_{\text{SR}}$  is also superimposed to show its relation to the orientation of the central lobe of the PSF. Along this vector, the resolution is at its highest (partly because of the frequency band of the pulse), while it is at its lowest perpendicular to it (Fresnel zone effect).

Both PSFs in Figure 3.14 are characterized by (1) a HR (high-resolution) axis that is parallel to the mean-scattering wavenumber vector and defines the "cross-reflector" resolution which would correspond to the "vertical" resolution ( $\lambda/4$  being the critical value), and (2) a LR (low-resolution) axis that is perpendicular to the HR axis and define the "lateral" resolution axis that correspond to the "horizontal" resolution (Fresnel zone).

### **Scattering wavenumber vector and resolution**

In order to obtain good resolution (sharp PSF), a large scattering-wavenumber band is needed. The orientation and length of  $\mathbf{k}_{\text{SR}}$  will decide the coverage in the wavenumber domain. The orientation is decided based on the wave propagation in the Earth model, whilst the length is proportional to the frequency. Thus, a large frequency band provides a large zone covered in the wavenumber domain, hence sharper resolution. On the other hand, larger velocity induces shorter wavenumber coverage that leads to poorer resolution which is a well known problem for deep structures since the velocity increases with depth. Also, shorter wavenumber coverage due to a large opening angle  $\theta_{\text{SR}}$  leads to poorer resolution.

### 3.5 Seismic forward modeling

Synthetic seismograms are the result of seismic forward modeling. The seismic response of an input earth model is generally defined in terms of either 1D, 2D or 3D variations in physical properties. Amongst other things, seismic forward modeling give interpreters the possibility to predict geology as an aid to plan a seismic reflection survey, and is conducted using specific geophysical software.

Forward modeling attempts to solve the *equation of motion* for seismic waves. The idea behind synthetic seismic traces is to enable comparison to real seismic data acquired in the field. If the two agree, the synthetic seismic section can be viewed as a reasonable model of the subsurface, and if not, new synthetic seismograms are created and compared once more. Therefore, forward modeling can be seen as an inverse modeling approach, both having the ultimate goal of determining geological structures and lithologies of the subsurface.

### 3.6 Seismic interpretation

When performing classical seismic interpretation on a data set, one focuses on seismic in-lines, cross-lines, random lines, time slices and horizon attributes (Hesthammer, Landrø, & Fossen, 2001). The main purpose of seismic interpretation is to decide if a subsurface area is a prospect for hydrocarbons. Therefore, one needs to study the rock's composition, extent, geometry and fluid content, all based on seismic interpretation.

In seismic interpretation, there are some parameters used that are particularly important: *Reflection amplitudes* shows the strength of the reflections at layer boundaries, which is dependent on the difference in acoustic impedance between them. *Reflector spacing* is the distance between the reflectors that indicates the thickness of the bed. Based on the wavelength, there is a lower limit where the thickness can be detected (Chapter 3.2.3). The *interval velocity* can provide information about the porosity and lithology of a sequence, but is not very accurate due to dependence on the stacking velocity. *Reflector continuity* is a direct response to how continuous the sedimentary beds are, and is very important for environment reconstruction. (Bjorlykke, 2010).

## 4 Plaster models

### 4.1 Introduction

This chapter will describe the different plaster model experiments and the technicalities around it. A brief description of the development of the geological structures will be made, in addition to how the plaster models will be converted into a geophysical basis for further synthetic seismic modeling.

### 4.2 Method

The modeling setup for the plaster experiments is described in both Sales (1987) and Fossen and Gabrielsen (1996). The same setup has been used in the current experiments, with a few alterations along the way (Figure 4.1).

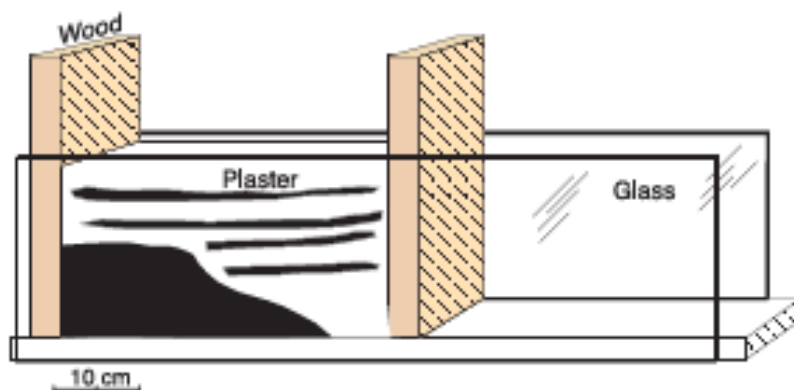


**Figure 4.1:** *Experimental set-up for the deformation rig used in the plaster experiment. (From Lindanger et al., 2004).*

A deformation box was built, consisting of a fixed wooden base, two glass side walls and two wooden end walls. One of the wooden end walls was fixed, while the other one was moveable.

Depending on what kind of structures we would like to see in our experiments, different initial basement geometries were constructed by using wet barite. The barite was smeared on the fixed wooden base with varying thickness (in general 3.5 - 4.0 cm height) and shape in each experiment. The barite was also used to seal small openings in the deformation box, to prevent leakage of liquid plaster. Next, the barite and the two glass walls were covered in canola oil, so that the plaster would glide smoothly on top of the barite and the moveable wooden wall would easily be moved due to less friction.

The plaster was mixed with water until it reached a satisfying consistency, which in general was accomplished by 9 liters of plaster and 6 liters of cold water. The plaster mixture was then poured into the deformation box on top of the barite basement. Since the plaster is homogeneous and no physical layering is present, we had to add markers onto the two glass walls before the plaster solidified, using a toothbrush. The markers consisted of carbon powder in some experiments, and blue acrylic paint in others. The markers do not affect the plaster in any physical way and was strictly used in order to observe and describe the deformation of the plaster. Even though there is no physical layering in the plaster models, the vertical direction of the plaster models may be affected by a water pressure gradient (Fossen & Gabrielsen, 1996).

When the plaster had reached sufficient shear strength and stiffness for fractures to form, the moveable wooden end wall would be pulled away from the fixed wall in extensional experiments, or pushed towards the fixed wall in contractional experiments. The experiments were all done by hand, so the rate of deformation would not be consistent throughout the experiments. According to Fossen and Gabrielsen (1996), this inconsistent deformation rate is to some extent similar to what happens along seismogenic faults.

All of the recent plaster experiments were photographed digitally every ~0.25 second, while older experiments were photographed at longer and less regular intervals, using 35 mm analog film. In this way we could observe and interpret the structural development at any given time of deformation.

#### ***Limitations and advantages in using plaster as a modeling material***

The advantages of plaster experiments in general is the simplicity of the model setup. Very little equipment is needed and the model is fairly easy to assemble. When executing plaster experiments, some problems may arise, as with any other modeling material. The plaster solidifies gradually after being poured into the deformation box, and according to Fossen and Gabrielsen (1996) this, in addition to expulsion of water, will provide changes in the physical properties of the plaster during the deformation. Also, because the plaster experiments are performed in a short time-frame due to rapid solidification, the plaster may not allow the water to drain fast enough. This may lead to some component of ductile deformation before brittle faulting (Fossen & Gabrielsen, 1996).

### 4.3 Contractional plaster model development

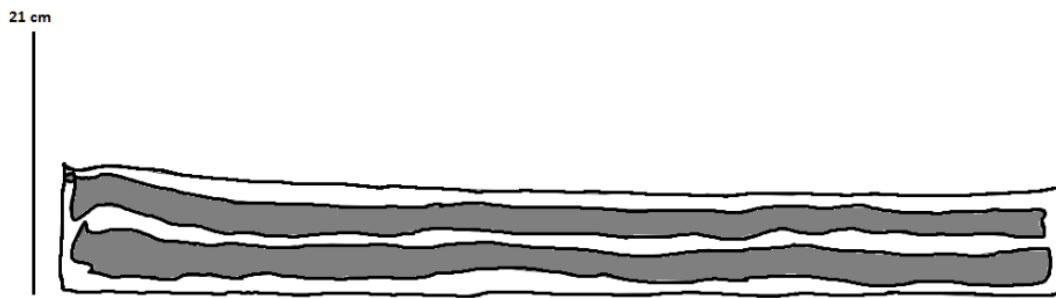
The contractional plaster model (Figure 4.2) was made in cooperation with Haakon Fossen and Eivind Bastesen at the Structural Geological Laboratory, Department of Earth Science at the University of Bergen in 2013. The experiment was executed as described in section 4.2 based on the experiments of Fossen and Gabrielsen (1996).



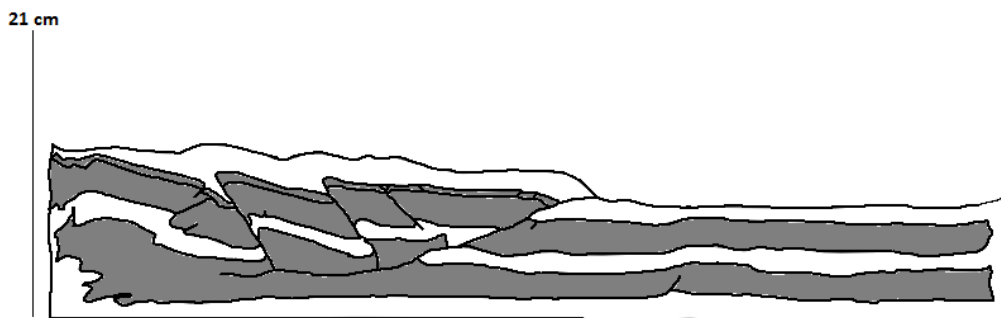
**Figure 4.2:** *The contractional plaster model.*

Figure 4.3 - Figure 4.6 shows the structural development of the contractional plaster model. After 50 % contraction (Figure 4.4), a master thrust fault has already started to develop in addition to backthrusts and a small reverse fault in the upper left corner. The thrust fault makes a ramp as the hanging wall overrides the footwall. After 75 % contraction (Figure 4.5), the backthrusts developed at an earlier stage have become much more evident, and even more so after 100 % contraction (Figure 4.6). The master thrust fault now stretch through the entire model, clearly making the hanging-wall mostly deformed. As understood by Boyer and Elliott (1982) a thrust environment contain duplexes, repeated layers of strata and multiple thrust faults. The contractional plaster model shows a definite repetition of layers (in the middle section) and also the beginning of a second thrust fault (or reverse fault) at the bottom right side of the model. Figure 4.2 is the contractional model that is used in the synthetic seismic modeling, as it displays numerous interesting structures.





**Figure 4.3:** *Contractional plaster model at 0 % contraction. The grey coloring represent the carbon powder used to create an artificial layering in the plaster.*



**Figure 4.4:** *Contractional plaster model at 50 % contraction.*

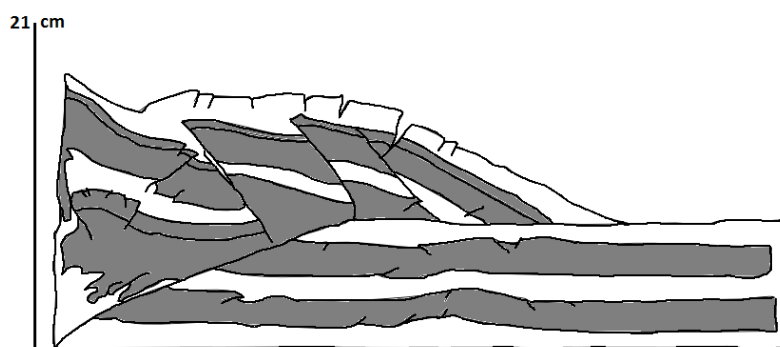


**Figure 4.5:** *Contractional plaster model at 75 % contraction.*

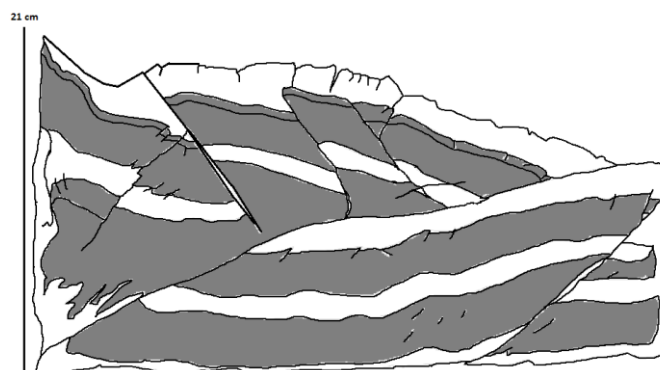


**Figure 4.6:** *Contractional plaster model at 100 % contraction. This is the model-stage used in the seismic modeling.*

#### 4.4 Extensional plaster model development

The extensional plaster model (Figure 4.7) was made in 1994 by Haakon Fossen and Roy Gabrielsen and is described in Fossen and Gabrielsen (1996). The model was chosen because it shows structures similar to those found in the Gullfaks area in the North Sea.



**Figure 4.7:** Extensional plaster model from 1994, made by Fossen and Gabrielsen (Picture by Simon Buckley).

Figure 4.8 below shows the structural development of the plaster model. Figure 4.8 (h) is the extensional model used in the seismic modeling in Chapter 5. A detailed structural description is found in Fossen and Gabrielsen (1996).

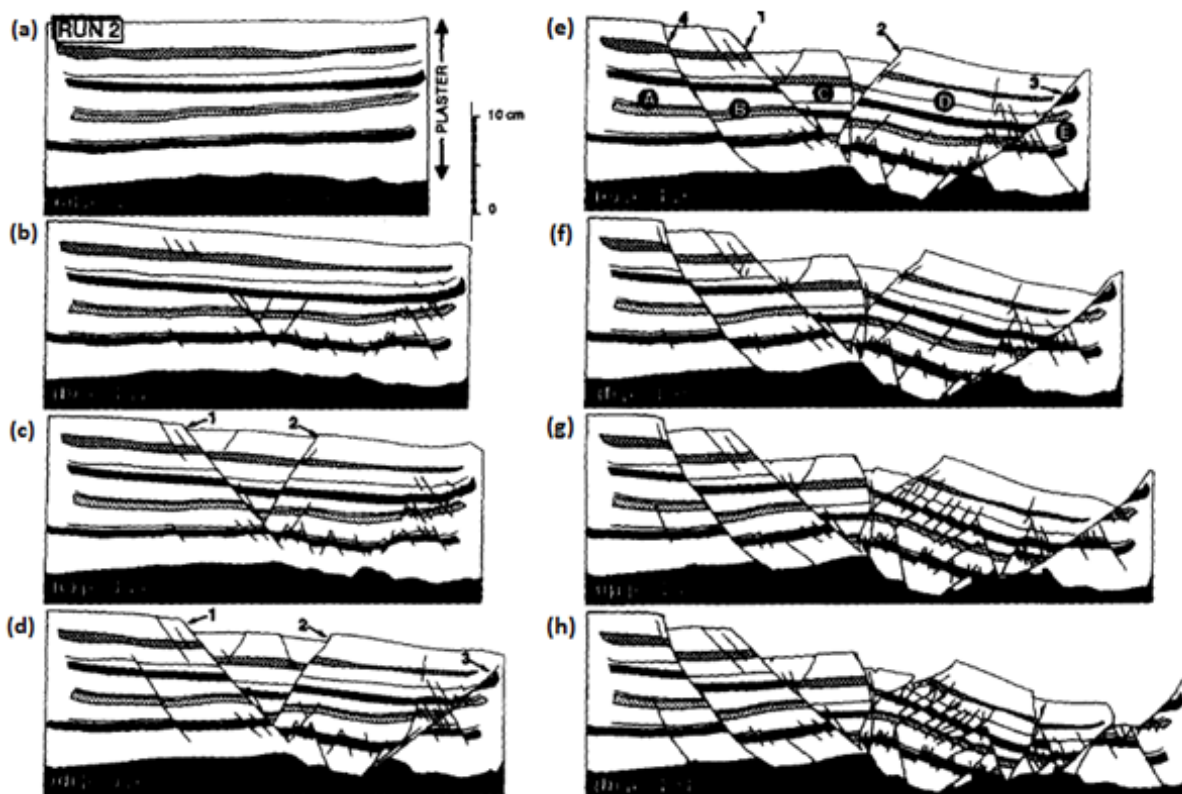


**Figure 4.8:** Run 2, incremental stages, beginning with (a) and ending at (h). Redrawn from side series taken during the experiment (From Fossen and Gabrielsen, 1996).

## 5 Modeling software and methods

### 5.1 Introduction

There are four main steps to follow before building a complete SeisRoX model: (1) define the modeling project and section area in NORSAR-2D's Console Window; (2) define the model geometry and properties in NORSAR-2D's Model Builder; (3) convert the resultant 2D model into a 2.5D model in NORSAR-3D's Model Builder; and (4) store the model as a SeisRoX 3D model and import it to SeisRoX for further modeling.

This chapter describes the main aspects of the NORSAR-2D/3D- and SeisRoX modeling tools with associated figures of plaster models.

### 5.2 NORSAR-2D model building procedure

The very first step in the model-building process is to open the NORSAR-2D's Console Window (Figure 5.1). Here, the background image of the plaster model is uploaded and a proper coordinate system is defined. The plaster models were then defined in terms of thickness and length (Figure 5.2).

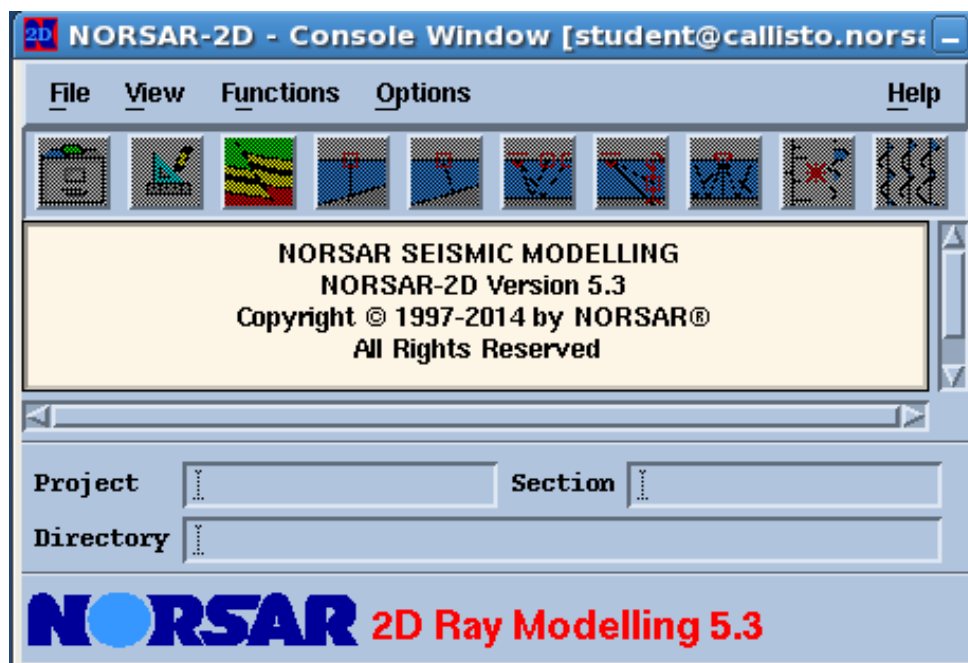


**Figure 5.1:** NORSAR-2D Console Window. This is the main window in NORSAR-2D, and the Model Builder function is the third icon from the left.

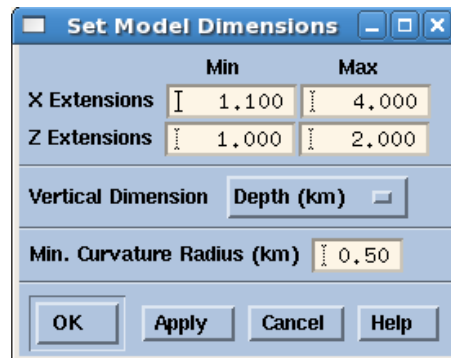


**Figure 5.2:** Model dimensions chosen in the X- and Z directions in NORSAR-2D.

The horizons of interest are drawn using a vector based drawing function, named NORSAR-2D Digitizer Tool. Here, all the horizons and major faults were defined as accurately as possible (Figure 5.3).

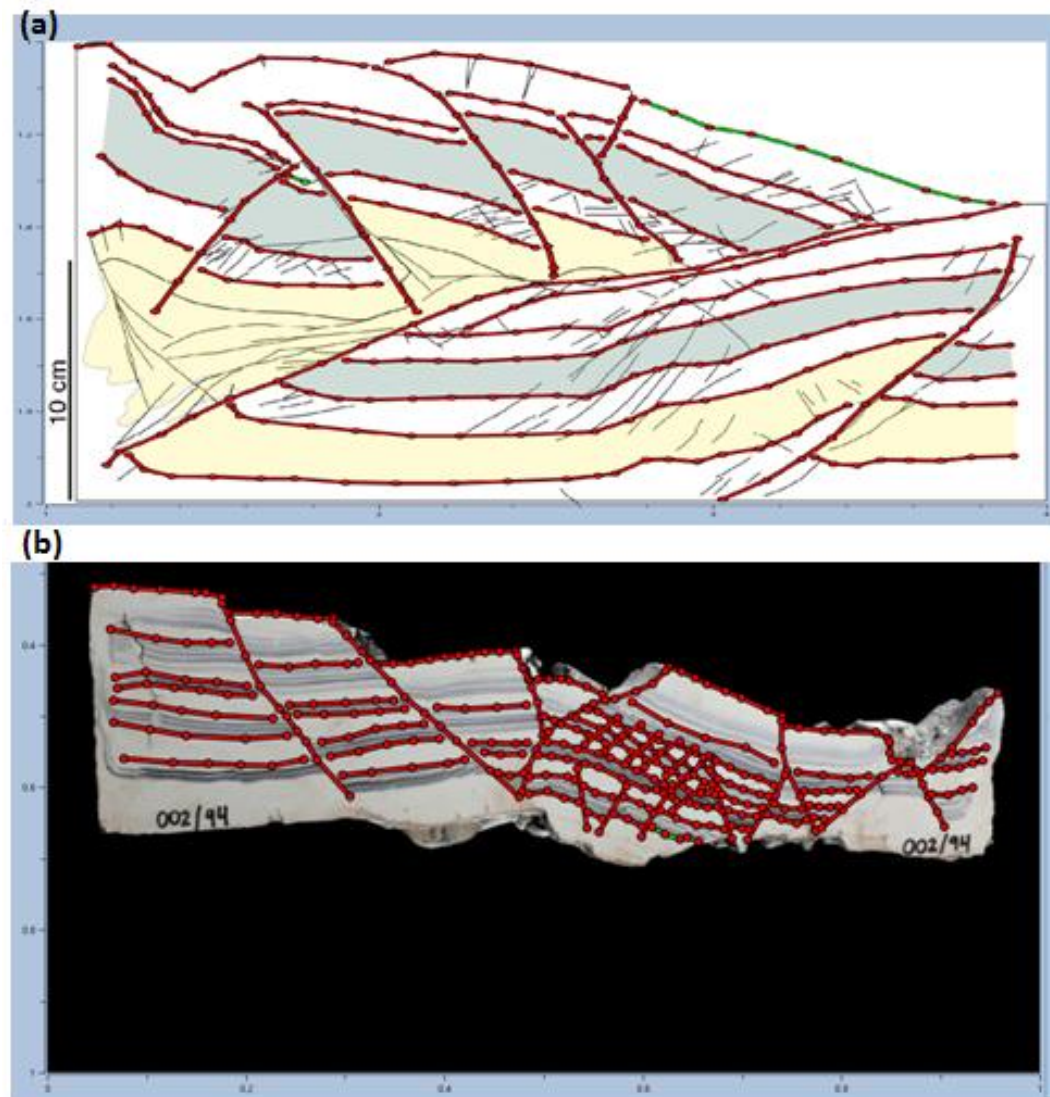


**Figure 5.3:** Horizons and faults of the (a) contractional plaster model and (b) extensional plaster model, defined using NORSAR-2D's digitizer tool.

In NORSAR-2D's Model Builder (third icon from the left on Figure 5.1), the recently drawn horizons are loaded and ready for further editing. In order to generate blocks so that each block can be assigned with specific elastic properties ( $V_P$ ,  $V_S$  and  $\rho$ ), the system needs to be closed, and therefore all the loaded horizons (hereafter named line-segments) must cross (Figure 5.4).

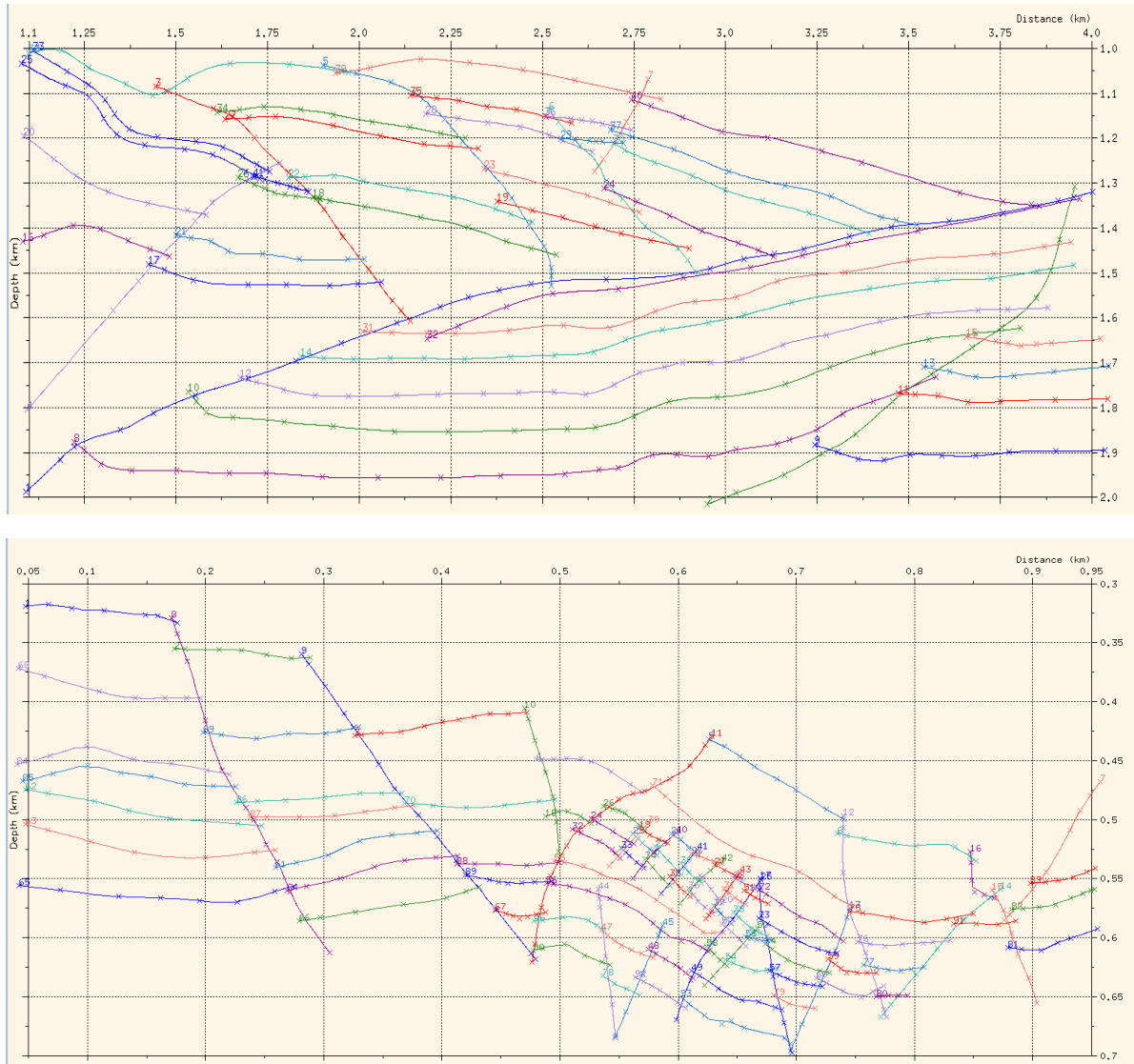


**Figure 5.4:** All line-segments crossing in NORSAR-2D. Upper: Contractional plaster model, lower: Extensional plaster model.

Due to memory limitations in NORSAR-2D, some line-segments had to be deleted in order to generate blocks in the extensional model. The maximum number of line-segments was set to 90, while 96 were originally drawn. Hence, the original plaster model is slightly altered.

To generate blocks assigned with elastic properties from the well logs in Appendix A, the VelRock module in NORSAR-2D was used, and five different layers with corresponding values of  $V_P$ ,  $V_S$  and density were made. Also, calculations of the matrix shear- and bulk modulus had to be made. All properties are displayed in Table 1.1.

**Table 1.1:** *Properties collected from well logs shown in Appendix A. The properties are central in the model building process.*

Formation/ Group	Core depth (m)	Shear modulus (GPa)	Bulk modulus (GPa)	Gamma- ray (API)	Acoustic impedance (kPa s/m)	Density (g/cm <sup>3</sup> )	$V_P$ (km/s)	$V_S$ (km/s)	$V_P/V_S$
Overburden		2.5410	9.7370			2.10	2.50	1.10	2.27
Unknown Fm.	-2390	3.4560	12.8880	80	7700	2.40	2.70	1.20	2.25
Draupne Fm.	2710-2820	7.6140	8.2720	75	7500	2.35	2.80	1.80	1.80
Brent Gr.	2400-2610	4.9500	9.4380	70	6000	2.20	2.70	1.50	1.80
Dunlin Gr.	2610-2850	6.5280	14.2460	85	6900	2.55	3.00	1.60	1.90
Statfjord Fm.	2850-3070	7.0805	18.4664	70	7550	2.45	3.40	1.70	1.80

Figure 5.5 - Figure 5.7 display the extensional- and contractional model after each block have been assigned with P-wave velocity, S-wave velocity and density. Each layer has constant values without any form of gradient, and the same values were used for both models.

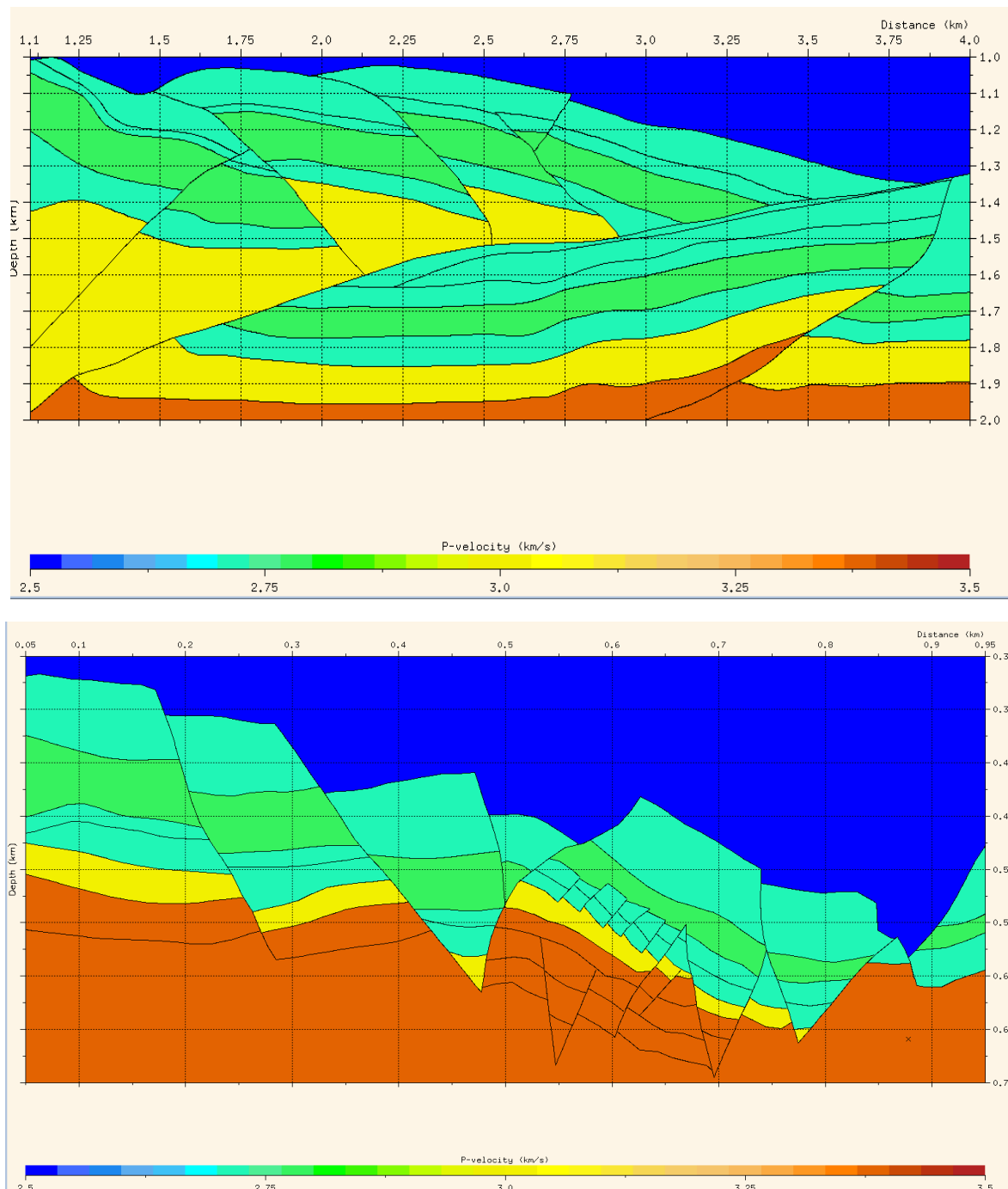


**Figure 5.5:** P-wave velocity from 2.5 km/s - 3.5 km/s assigned to each block in NORSAR-2D Model Builder. Upper: Contractional plaster model, lower: Extensional plaster model. Orange color: Statford Fm; Yellow color: Dunlin Group; Turquoise color: Brent Group; Green color: Draupne Fm; Light blue color: Unknown Fm; Dark blue color: Overburden (see Table A.1 in Appendix A).

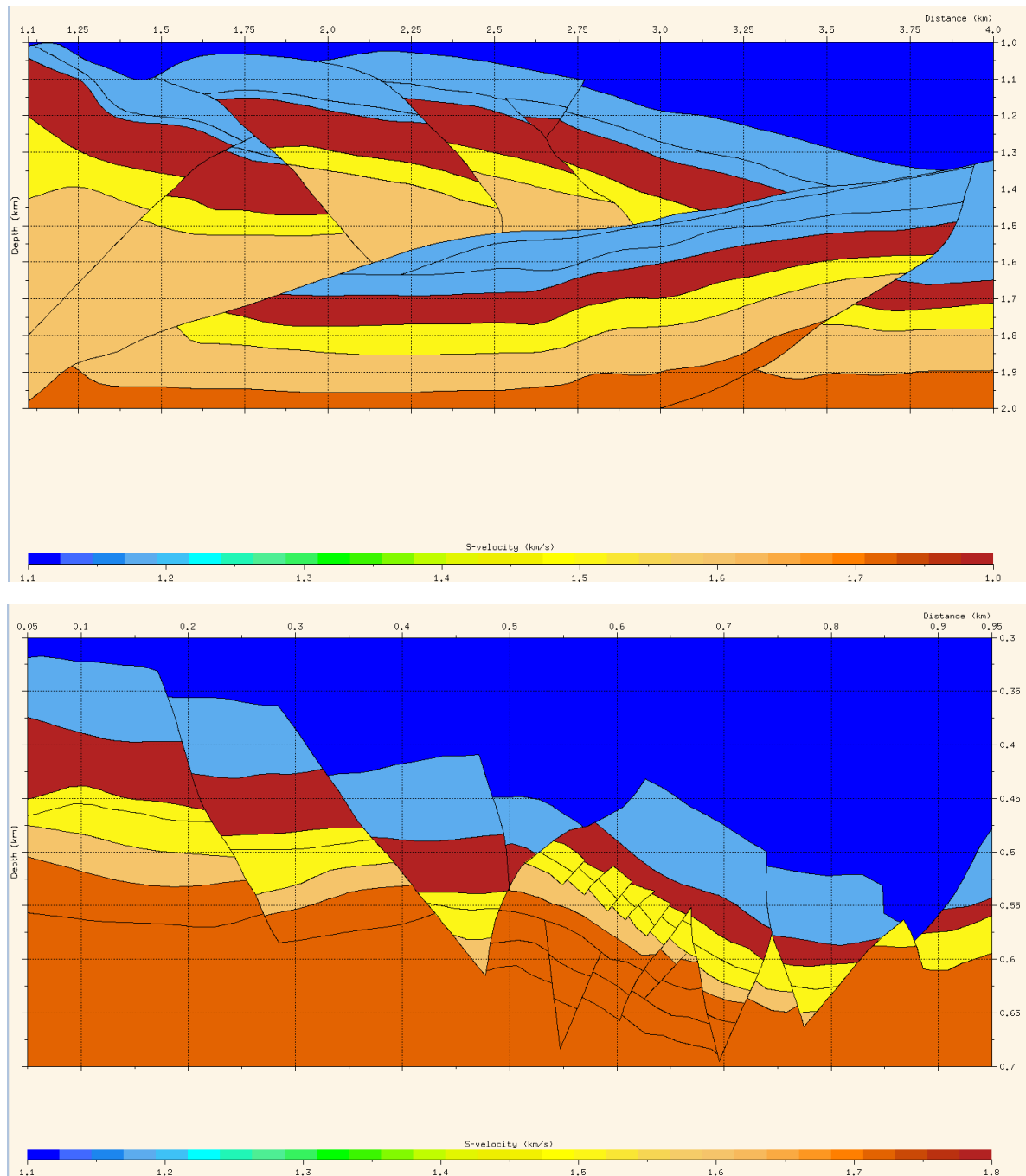


**Figure 5.6:** *S-wave velocity from 1.1 km/s - 1.8 km/s assigned to each block in NORSAR-2D Model Builder. Upper: Contractional plaster model, lower: Extensional plaster model. Orange color: Stafford Fm; Beige color: Dunlin Group; Yellow color: Brent Group; Red color: Draupne Fm; Light blue color: Unknown Fm; Dark blue color: Overburden (see Table A.1 in Appendix A).*



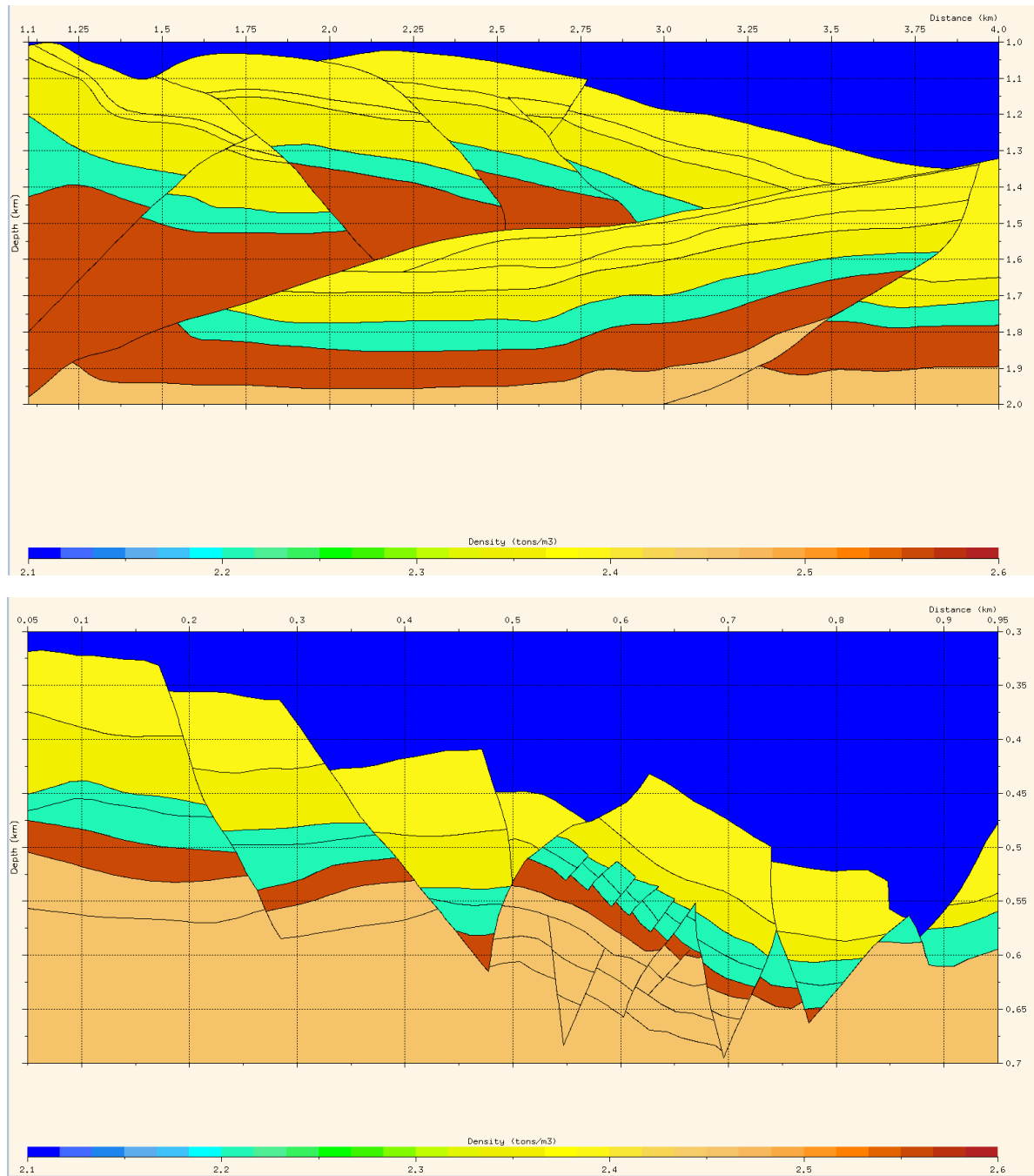


**Figure 5.7:** Density from  $2.1 \text{ tons/m}^3$  -  $2.6 \text{ tons/m}^3$  assigned to each block in NORSAR-2D Model Builder. Upper: Contractional plaster model, lower: Extensional plaster model. Beige color: Statfjord Fm; Brown: Dunlin Group; Turquoise color: Brent Group; Yellow color: Draupne Fm; Second yellow color: Unknown Fm; Dark blue color: Overburden (see Table A.1 in Appendix A).

### 5.3 From 2D model to 2.5D model

Once the 2D model is created in NORSAR-2D's Model Builder, it is converted into a 2.5D model in NORSAR-3D. In order to do so, a SMIF (Seismic Model Interchange File)-file is generated in NORSAR-2D, which is compatible with NORSAR-3D.

NORSAR-3D's Console Window is opened and the Model Builder option selected. Under the File menu one can choose "load 2D model from SMIF" and generate a 2.5D model. The reason why it's termed a 2.5D model is that there is no lateral variation in property or geometry along one of the axis. Still, it can be considered a 3D model, and will be in the next section.

### 5.4 From 2.5D model to a SeisRoX 3D model

When the 3D (previously termed 2.5D) model has been created in the NORSAR-3D Model Builder it can be stored as a compatible SeisRoX 3D model. Before being able to select and view the created 3D model in a SeisRoX 3D Depth Viewer window, a proper project- and section area have to be defined in SeisRoX. This procedure is the same as the one done in the NORSAR software.

### 5.5 SeisRoX<sup>TM</sup> modeling software

SeisRoX<sup>TM</sup> is a software suite developed by NORSAR, where the new workflow for PSDM simulation use spatially varying Point Spread Functions (PSF) (NORSAR, 2014), see Chapter 3. The software can be applied when modeling overburden, survey consistent seismic response and other seismic attributes for any given reservoir model. The software provides several useful tools for building 3D- and 4D models and also contain flexible workflows for PSDM simulation. By varying different geological and seismic properties, in addition to reservoir geometry, great control over the resulting seismic image is gained. The software is useful on both large scale and small scale models where both survey characteristics and effects of any potential overburden can be incorporated. In this way, SeisRoX is useful when studying how simple variations in model properties can affect the seismic sensitivity.

There are some key elements of SeisRoX that are represented in Figure 5.8 and is further explained in Chapter 5.5.1.

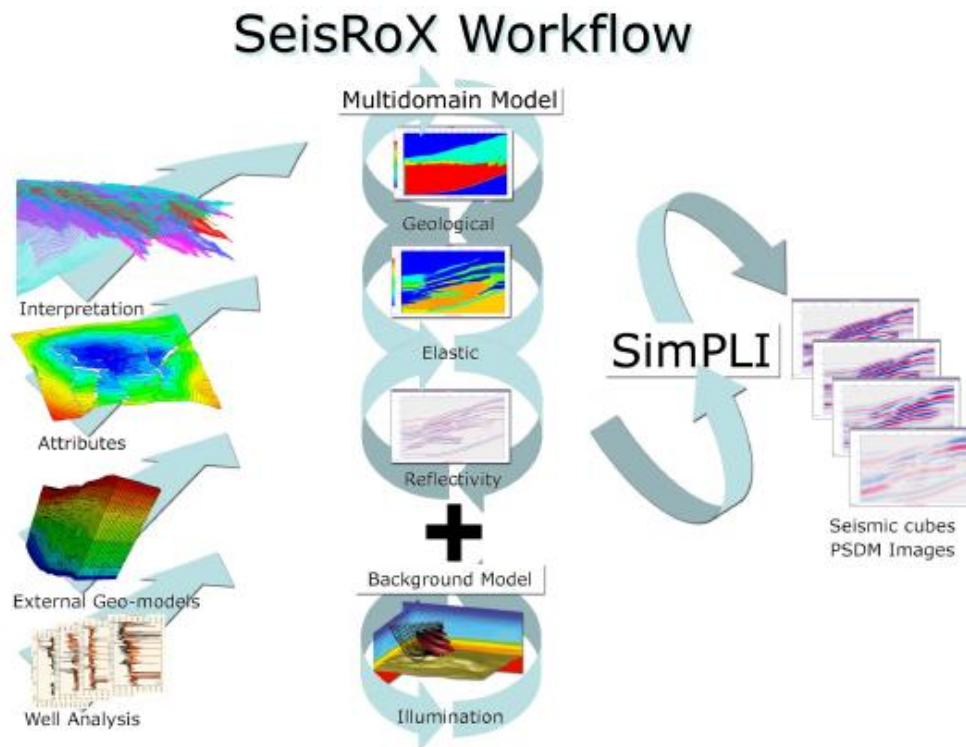


**Figure 5.8:** An overview of the main elements of the SeisRoX modeling package (NORSAR, 2011).

#### 5.5.1 The multi-domain model

One of the most important aspects of the SeisRoX software, is the *multi-domain model*, where the model is going from a *geological domain* to the *elastic domain* and further to the *reflectivity domain*. The geological domain include rock-related properties such as lithology, porosity, fluid type etc. The elastic domain include rock-related properties like seismic velocities, elastic moduli, density, seismic impedances etc. The reflectivity domain include properties related to the horizons like reflection coefficients, AVO parameters, etc. (NORSAR, 2011).

This thesis involve all parts of the multi-domain model. The geological domain is defined by the plaster models, where lithologic aspects are defined based on the geological analogues seen in Chapter 2. The elastic domain is entered when assigning the elastic properties seen in Table A.1 to the separate blocks in the plaster models.

### 5.5.2 The SimPLI (Simulated Prestack Local Imaging) method

The SimPLI method is a seismic modeling method that simulates the PSDM (pre-stack depth migrated) seismic response from a given target within the SeisRoX model (NORSAR, 2011). The key parameter in the SimPLI method is the scattering wavenumber, calculated by using the background velocity field (Chapter 3.4.2), and has contributed to the SimPLI method being a great tool for obtaining pre-stack depth migrated images.

Simulated pre-stack migrated sections are easily obtained as functions of a survey, wave models, emitted pulses, etc., and enable interpreters to monitor the illumination, time-lapse evolution and resolution of a section during production. Interpreted horizons with various attributes, property grids or other hypothetical models are used as input, and pre-stacked migrated sections displayed either in depth or time is the resulting product. The SimPLI method is a convolution technique, but unlike 1D convolution, this method allows the user to predict both 2D and 3D effects of illumination and resolution without the need of modeling and migration. Also, the 1D reflectivity techniques are failing compared to the 2D/3D techniques (Lecomte, Gjøystdal, & Drottning, 2003).

## 5.6 General modeling setup in SeisRoX

In order for the SeisRoX modeling process to work, some additional elements have to be defined. This section describes the general modeling setup in SeisRoX, applied to both plaster models.

### 5.6.1 Definition of background model

The background model takes into account the seismic wave propagation effects from the survey geometry, source wavelet and overburden. When creating a background model, one can either chose a homogeneous 1D model or a layer 1D model. 1D implies that property variations only exist in one direction. A layered 1D overburden model was chosen for this thesis, containing three different layers with increasing elastic values ( $V_P$ ,  $V_S$  and  $\rho$ ) with depth, layer 1 being the water column (Figure 5.10). Figure 5.9 shows the object list in SeisRoX, where the 1D background model is created, along with several other elements that need to be defined.

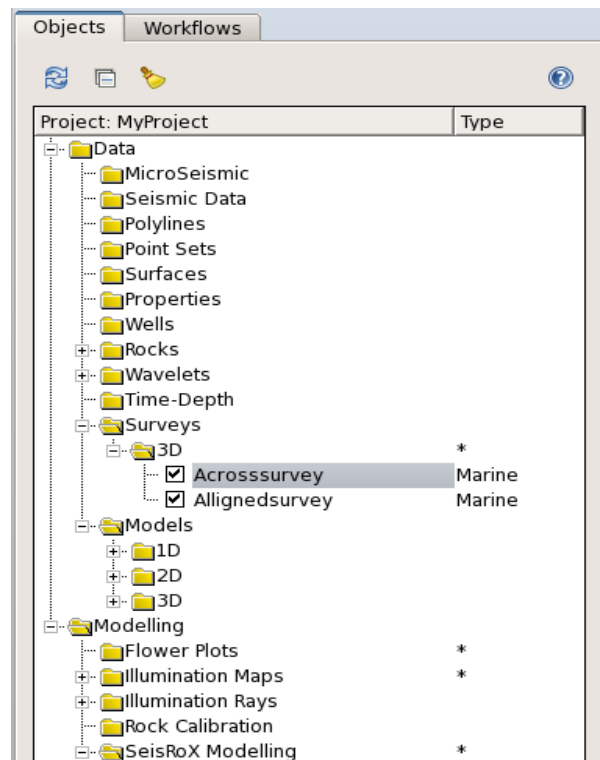


**Figure 5.9:** Example of an object list. The folders contain different elements that needs to be defined. The folder named "1D" is where the background model in Figure 5.10 is created.

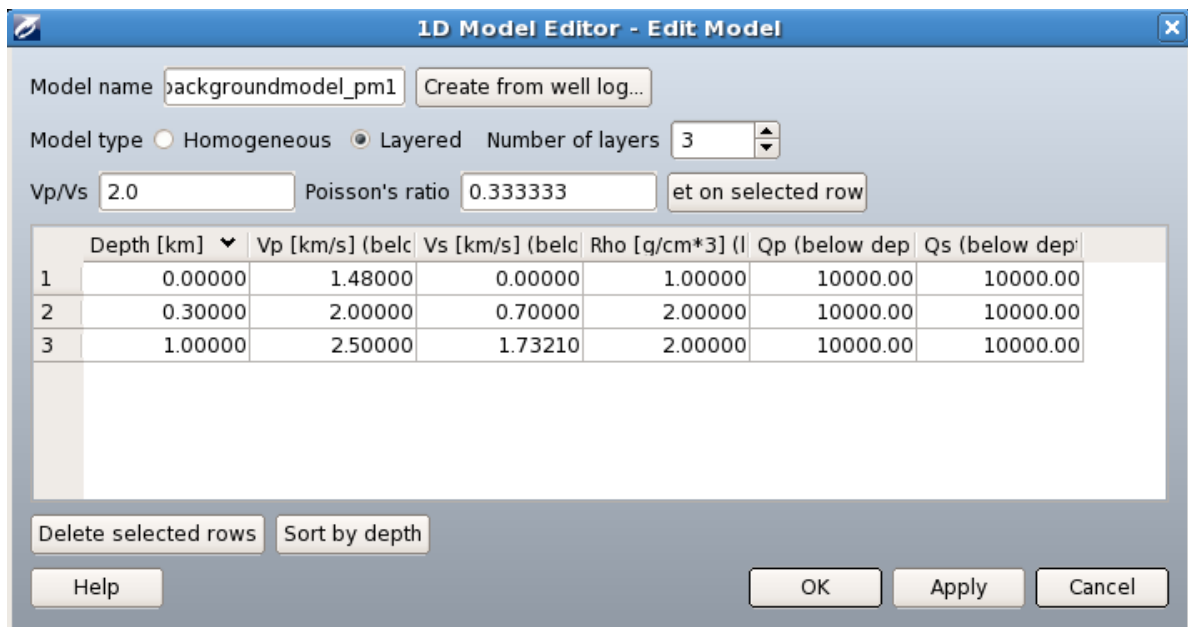


**Figure 5.10:** 1D layered background model made in SeisRoX. Three different layers were defined in terms of depth (km), P-wave velocity (km/s), S-wave velocity (km/s) and density ( $\text{g/cm}^3$ ).

### 5.6.2 Survey definition

When conducting a seismic survey, the source/receiver geometry is defined in terms of number of sources and receivers, in addition to the spacing between them. Seismic modeling is a very affordable approach when the target and subsurface geology is recognized, (Lines & Newrick, 2004) as for this thesis.

There are three survey type options in SeisRoX; *fixed*, *marine* and *coil*, where the preferred survey type is the marine for this thesis.

An important part of the survey definition is the shot- and streamer/receiver configuration, which is shown in Table 5.1. The center (x, y) defines the horizontal coordinates of the survey center point, which in this case is given in local coordinates. The shots are placed at a certain depth, and the rotation describes the shot line angles relative to the x-axis. Also, one can decide the number of shot lines, the shot line length, the shot line spacing and shot spacing. The shot line spacing is the distance between each shot line, whereas the shot spacing is the distance between each shot on one single line.

The streamer/receiver configurations are similar to the shot configuration. The absolute depth refers to the depth of the receivers, and the minimum offset refers to the horizontal distance from a shot to the closest receiver on the streamer. The number of streamers are chosen, along with the streamer length and streamer spacing (the distance between separate streamers). The receiver spacing defines the distance between each receiver on a streamer.

Figure 5.11 shows the 3D contractional plaster model in the SeisRoX Depth Viewer window, where the strike- and dip survey configurations are displayed. Both survey configurations consist of 10 shot lines of 8 km length and 9 streamers of 4 km length.

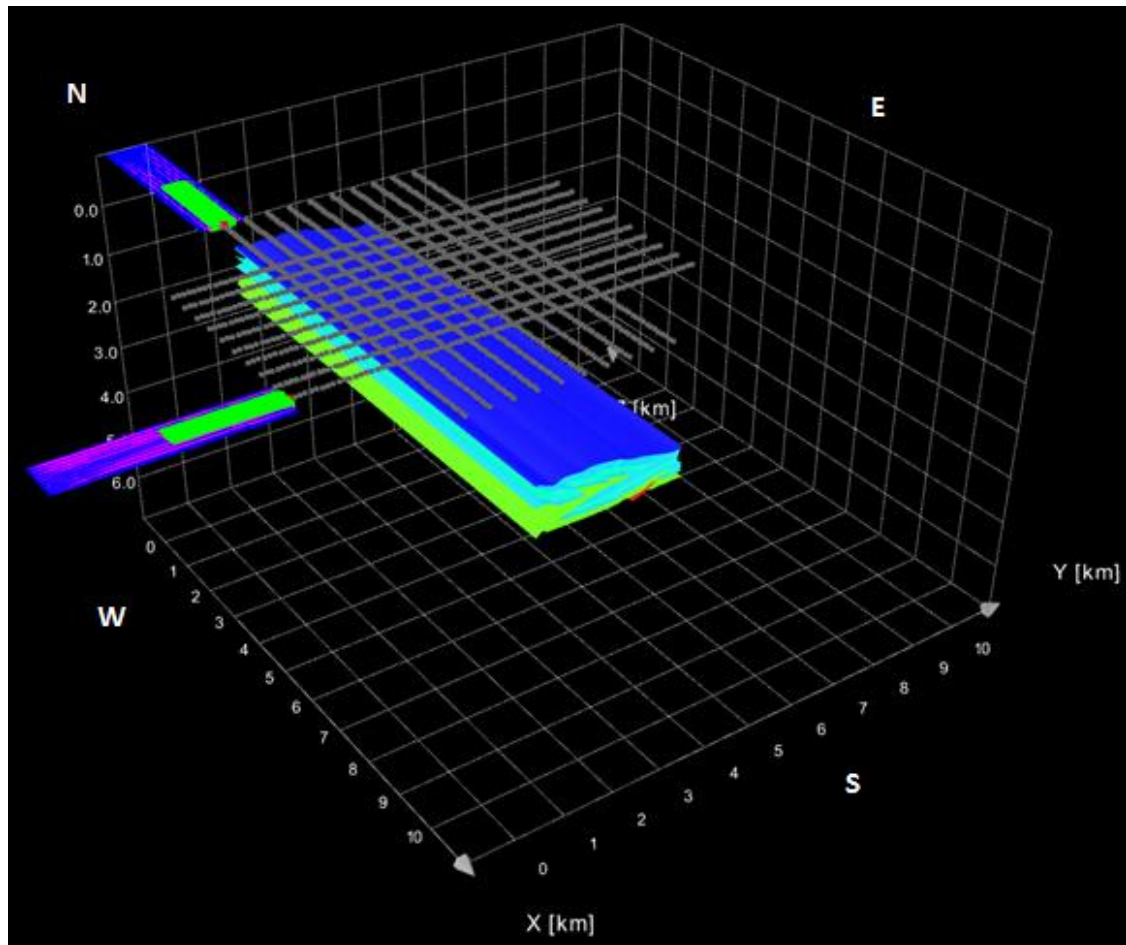


**Figure 5.11:** Two different survey configurations - one along strike with the structure (strike survey), and one across the structure (dip survey), here showing the contractional plaster model as target. The grey color represent the shot lines and the purple and blue color represent the streamers containing receivers. The target is the contractional plaster model displayed in terms of P-wave velocity, as seen in Figure 5.12.

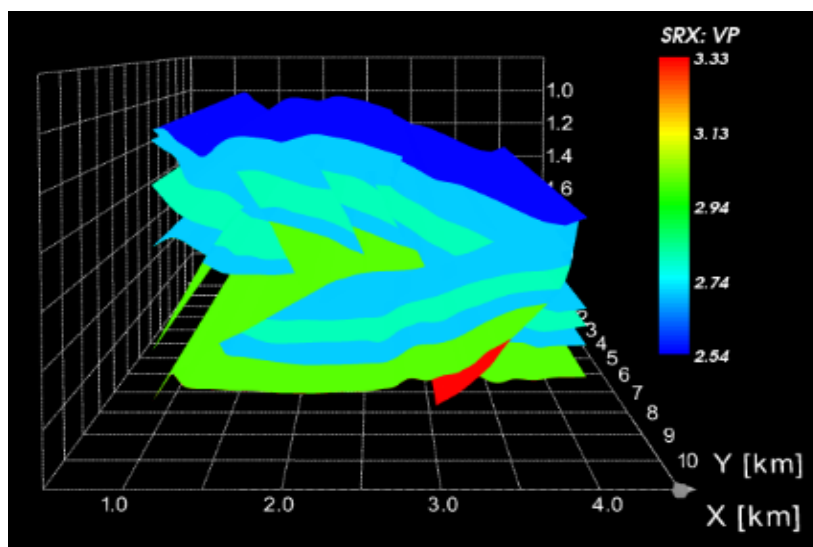


**Figure 5.12:** Contractional model displayed in terms of P-wave velocity.

**Table 5.1:** Survey- and streamer/receiver configurations. The table describes the dip survey configurations, where the only difference between the dip- and strike survey is that there is zero rotation for the strike survey.

<i>Shot configuration (units in km)</i>		
Center (x, y)	5.000	2.500
Depth		0.005
Rotation (degrees)		90.000
Number of shot lines		10
Shot line length		8.000
Shot line spacing		0.450
Shot spacing		0.100
<i>Streamer/receiver configuration (units in km)</i>		
Absolute depth		0.005
Minimum offset		0.100
Number of streamers		9
Streamer length		4.000
Streamer spacing		0.100
Receiver spacing		0.0500

### 5.6.3 Creating a workflow

In order to run a SimPLI workflow, certain inputs have to be selected. These are shown in the object list in Figure 5.9. When the objects have been properly defined, they are displayed in the workflow list shown in Figure 5.13. Here, a preferred survey type, reservoir model, background model, surveys, wavelets and simulated PSDM parameters are chosen before the simulation is conducted.



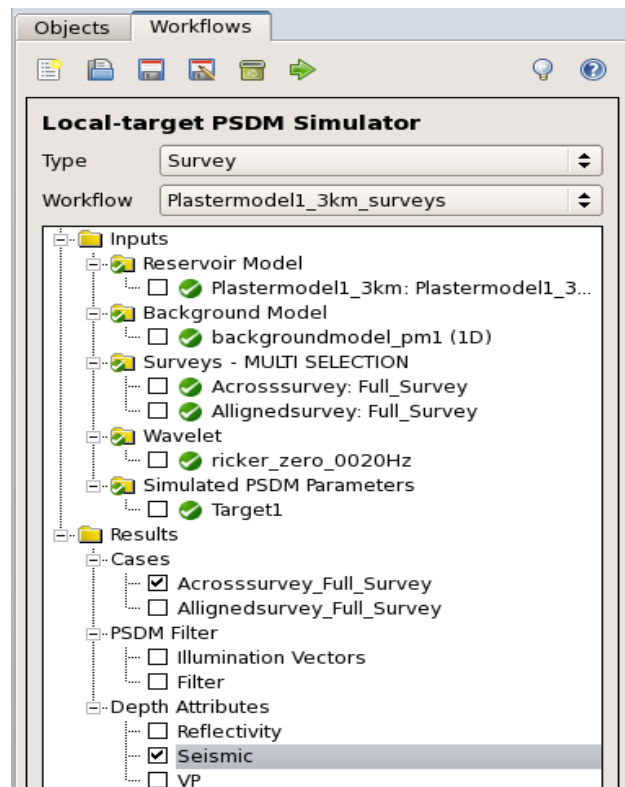


**Figure 5.13:** Example of a workflow list, where the green arrows indicate that the needed parameters have been filled in, and the simulation is ready to be run.

### **Wavelet selection**

When it comes to wavelets, the Ricker wavelet is often applied for modeling purposes as it is defined by its dominant frequency. By definition, the Ricker wavelet is zero-phased, and seems to represent a typical Earth response. Three different Ricker zero wavelets (30 Hz, 20 Hz and 10 Hz) were applied for depths of 1 km, 3 km and 5 km, respectively (Figure 5.14). The Ricker wavelet (zero-phased) was chosen because of its convenience when it comes to interpreting seismic sections, since the maximum amplitude pulses are shown at layer boundaries, with lower amplitudes in the side lobes (see Chapter 6: Results).

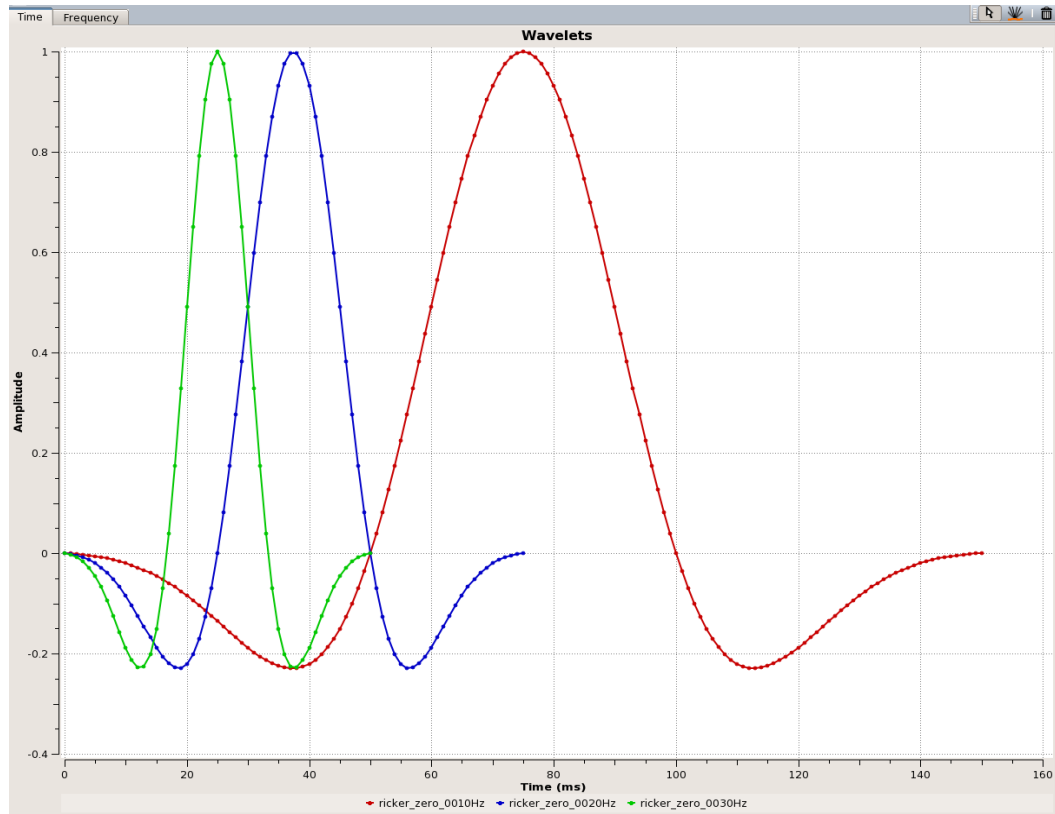


**Figure 5.14:** The different frequency wavelets used when conducting the surveys. 1 km = Ricker zero 30 Hz (green curve), 3 km = Ricker zero 20 Hz (blue curve) and 5 km = Ricker zero 10 Hz (red curve).

***Definition of remaining workflow input: Simulated PSDM parameters***

The Simulated PSDM parameters are crucial to define in order for the simulation to work. The PSDM parameters chosen for this thesis is shown in Table 5.2 and encompass definition of PSDM target, Reflectivity, Simulated PSDM Method and PSDM Filters.

**Table 5.2:** *SeisRoX workflow parameters.*

<i>Simulated PSDM Parameters</i>		
<i>PSDM Target</i>		
Center X,Y (km)		5, 2.5
Depth Z (km)		1.5
Grid type		3D
Size (km)		0.05, 3, 1.2
Sampling (km)		0.01, 0.01, 0.0025
<i>Reflectivity</i>		
Reflectivity method		Zoeppritz
Incident angle selection		Angle range
Angle range (deg)		0 - 40
Angle sampling (deg)		10
<i>Simulated PSDM Method</i>		
	Method	True amplitude
<i>PSDM Filters</i>		
	Aperture range (km)	0 - 3
	Traveltime range (s)	0 - 8

As soon as these parameters have been set, the generation of simulated PSDM images can begin. When the run is complete, the generated data is stored in the objects list and can be displayed in the viewer window as depth attributes. The depth attributes generated in this thesis is the reflectivity series and seismic (Chapter 6: Results).

---

## 6 Results

### 6.1 General result information

This chapter contains the results of the seismic modeling performed on the two plaster models described in Chapter 4. Both plaster models were assigned with the same elastic properties and identical survey configurations were applied (except for 90 degrees rotation in the dip survey).

The plaster models were placed on depths of 1 km, 3 km and 5 km and frequency wavelets of Ricker zero 30 Hz, 20 Hz and 10 Hz were correlated to each depth (Figure 5.14). A velocity increase of 10 % and 20 % was set for depths of 3 km and 5 km, respectively (see Table A.1 in Appendix A).

Illumination vectors, described in section 3.4, provide essential information regarding the seismic illumination and resolution properties. Azimuth and dip of potentially illuminated reflectors are therefore represented for each synthetic seismogram in Chapter 6.3.4.

All synthetic seismic sections are displayed in the depth domain.

### 6.2 Contractional plaster model results

Figure 6.1 and Figure 6.2 show the resulting seismograms of a dip- and strike survey where the target is placed at 1 km, 3 km and 5 km with adjoining frequency wavelets and velocities. This display clearly shows how larger burial depth as a function of frequency and velocity increase affect the seismic resolution and illumination of various structures. Further explanation regarding each depth will be displayed in the next sub-chapter.

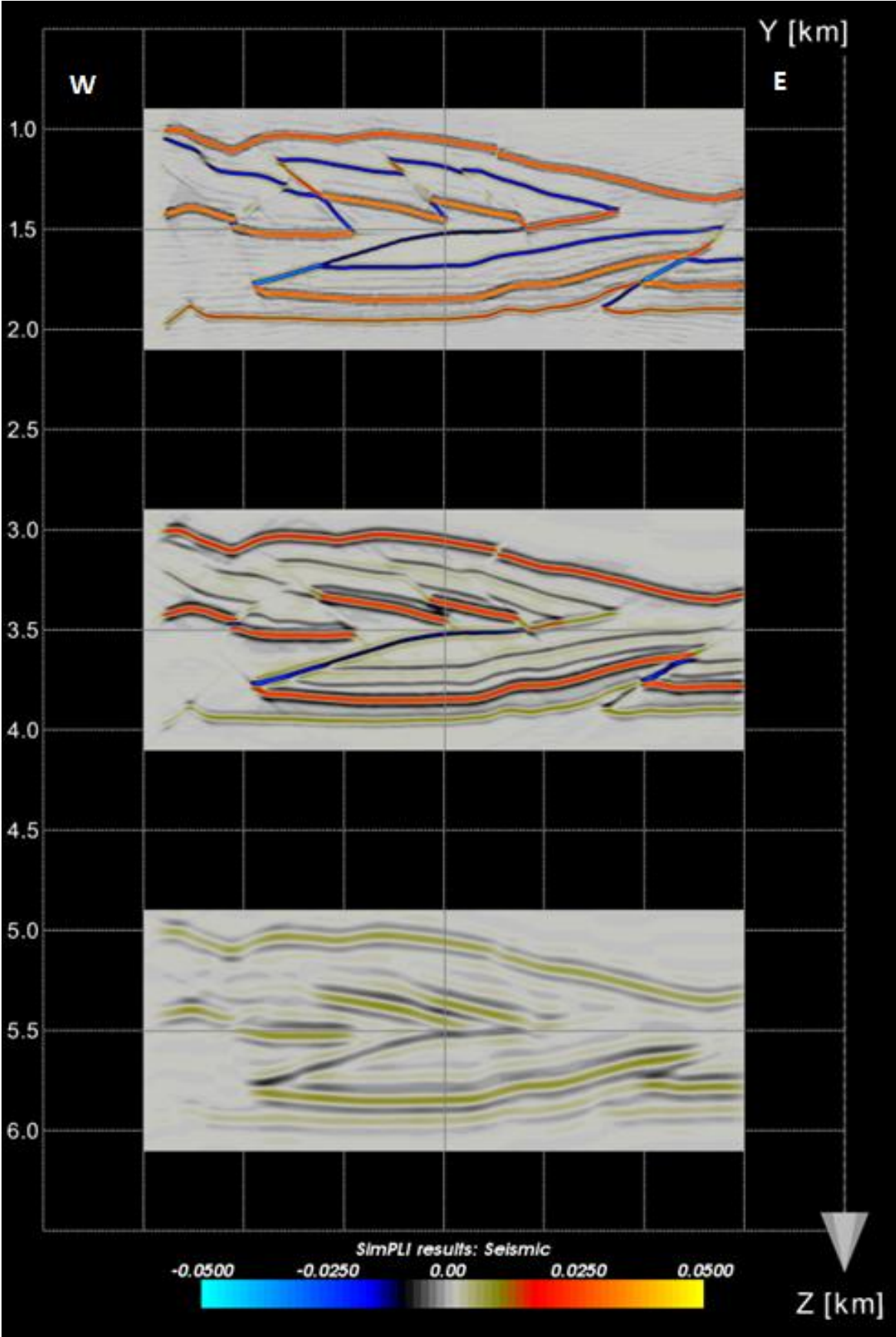


**Figure 6.1:** Contractional plaster model seismograms as a result of a dip survey, with target placed at depths of 1 km, 3 km and 5 km.

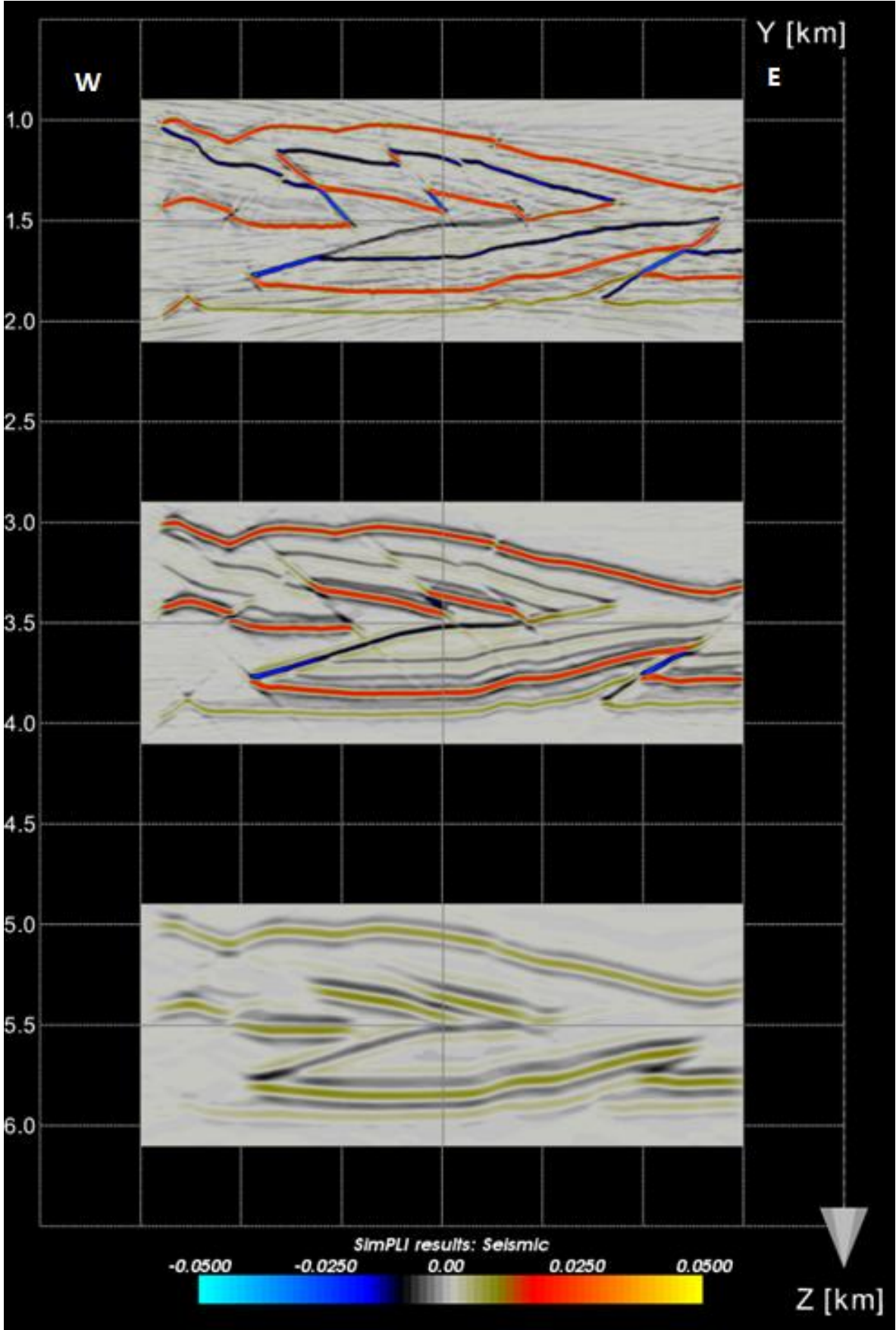
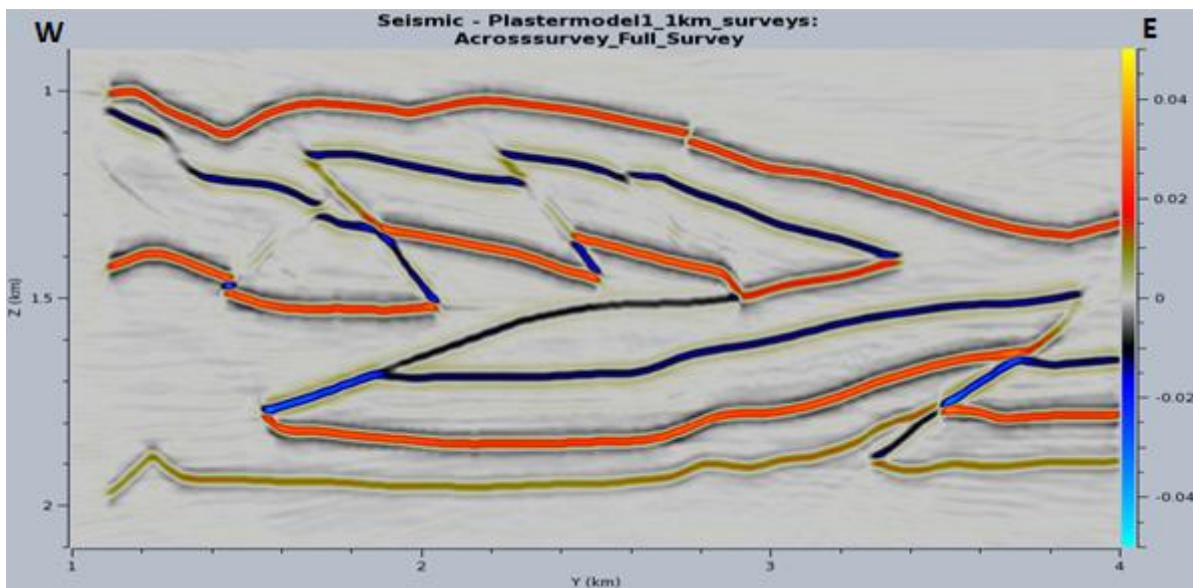


**Figure 6.2:** Contractional plaster model seismograms as a result of a strike survey, with target placed at depths of 1 km, 3 km and 5 km.

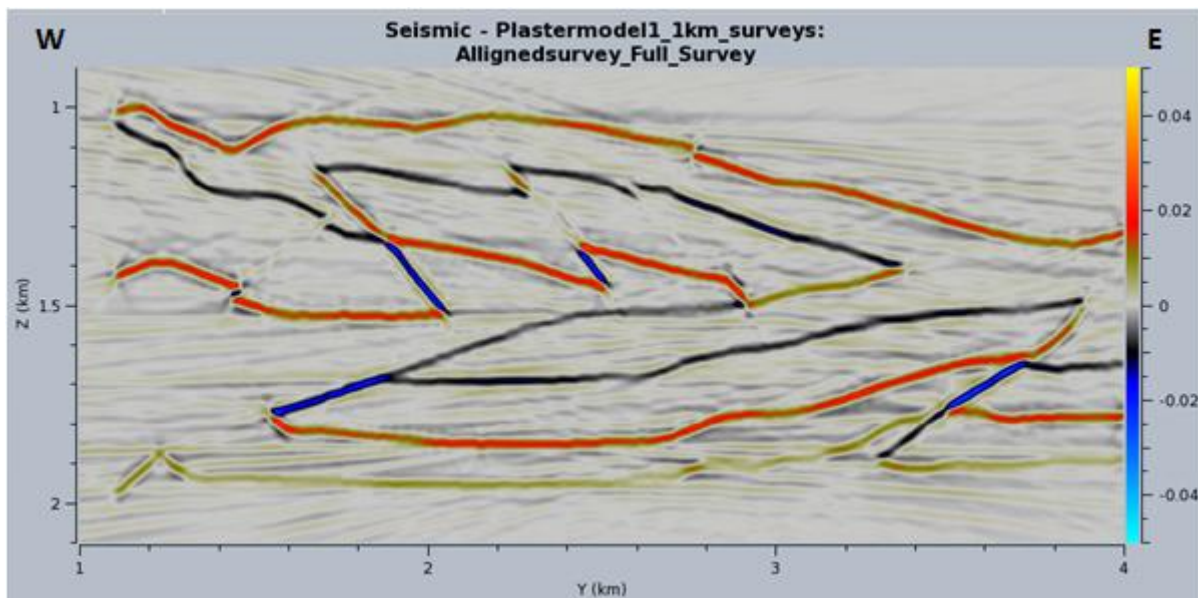
### 6.2.1 Strike- and dip survey at 1 km depth using Ricker zero 30 Hz frequency.

Figure 6.3 and Figure 6.4 show the resulting seismograms of a dip- and strike survey, where the target is placed at 1 km depth, using Ricker zero 30 Hz frequency wavelet.

There are obvious differences in regards to noise and reflection strength, where the weakest reflections in the dip survey seismogram are even weaker in the strike survey seismogram.



**Figure 6.3:** Contractional plaster model seismogram at 1 km depth as a result of a dip survey, using Ricker zero 30 Hz frequency wavelet.



**Figure 6.4:** Contractional plaster model seismogram at 1 km depth as a result of a strike survey, using Ricker zero 30 Hz frequency wavelet.

The major thrust fault, in addition to the lowermost reflector, is blurry and weak in the strike survey seismogram compared to the dip survey seismogram. The fault planes of the backthrust faults are vaguely displayed in both seismograms and can only be interpreted as faults based on breaks and offsets in the reflectors. Also, the thrust fault, that originally stretches through the entire model (Figure 4.2), is not visible on the western and eastern side (depth of ~1.8 km and ~1.5 km, respectively) in either of the seismograms. The minor reverse fault on the lower east hand side is properly displayed in both seismograms. The fault plane of the small reverse fault in the upper west corner is not displayed as a reflector, but is still noticeable based on offset and break in the reflector. Some layer boundaries that were drawn in NORSAR-2D from the original plaster model are not reflected in the two synthetic seismic sections, and if so, they are vaguely displayed.

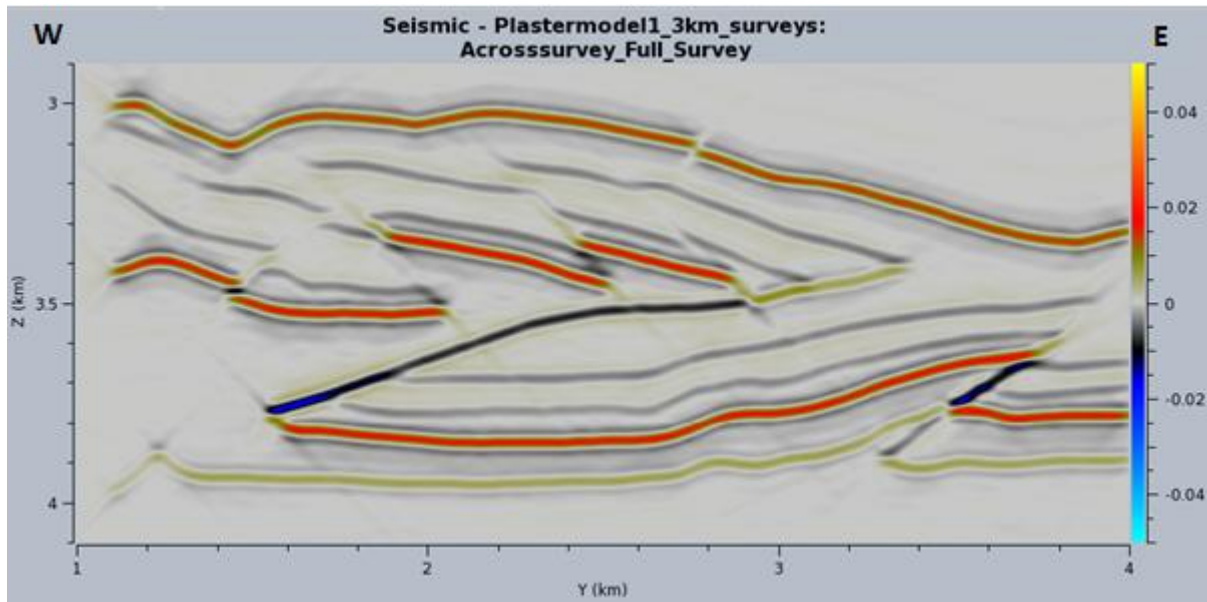
### **6.2.2 Strike- and dip survey at 3 km depth using Ricker zero 20 Hz frequency.**

Figure 6.5 and Figure 6.6 shows the resulting seismograms of a dip- and strike survey where the target is placed at 3 km depth, using Ricker zero 20 Hz frequency wavelet.

The reflectors in these seismograms are wider than in the previously discussed models, in addition to being weaker in the strike survey seismogram than in the dip survey seismogram. Also, the strike survey seismogram contain more noise than the dip survey seismogram.

If comparing the major thrust fault in Figure 6.4 (at 1 km depth) to Figure 6.6, it is slightly improved in the latter in regards to reflection strength. The minor reverse fault on the lower east side is yet again properly displayed in both seismograms. The reverse fault in the upper west corner is not represented as a reflection, but still noticeable due to offset, which also apply for the backthrust faults. All layer boundaries drawn in NORSAR-2D are present in both the dip- and strike survey resulting seismograms, although most reflections are vague.





**Figure 6.5:** Contractional plaster model seismogram at 3 km depth as a result of a dip survey, using Ricker zero 20 Hz frequency wavelet. The seismic velocities and density have been increased 10 %.

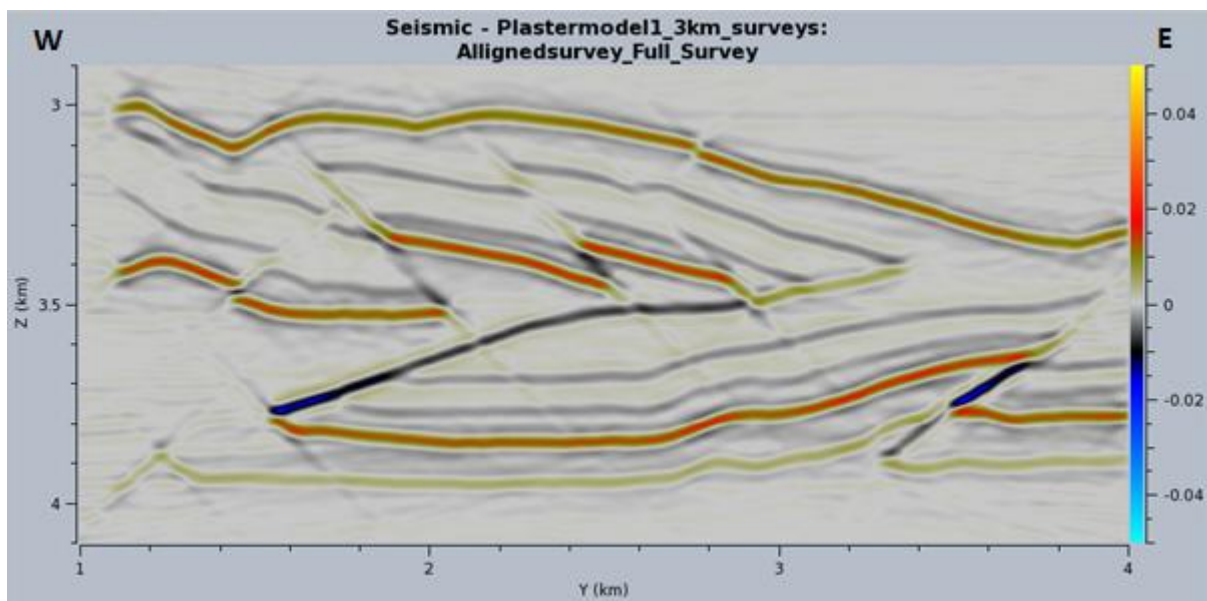


**Figure 6.6:** Contractional plaster model seismogram at 3 km depth as a result of a strike survey, using Ricker zero 20 Hz frequency wavelet. The seismic velocities and density have been increased 10 %.

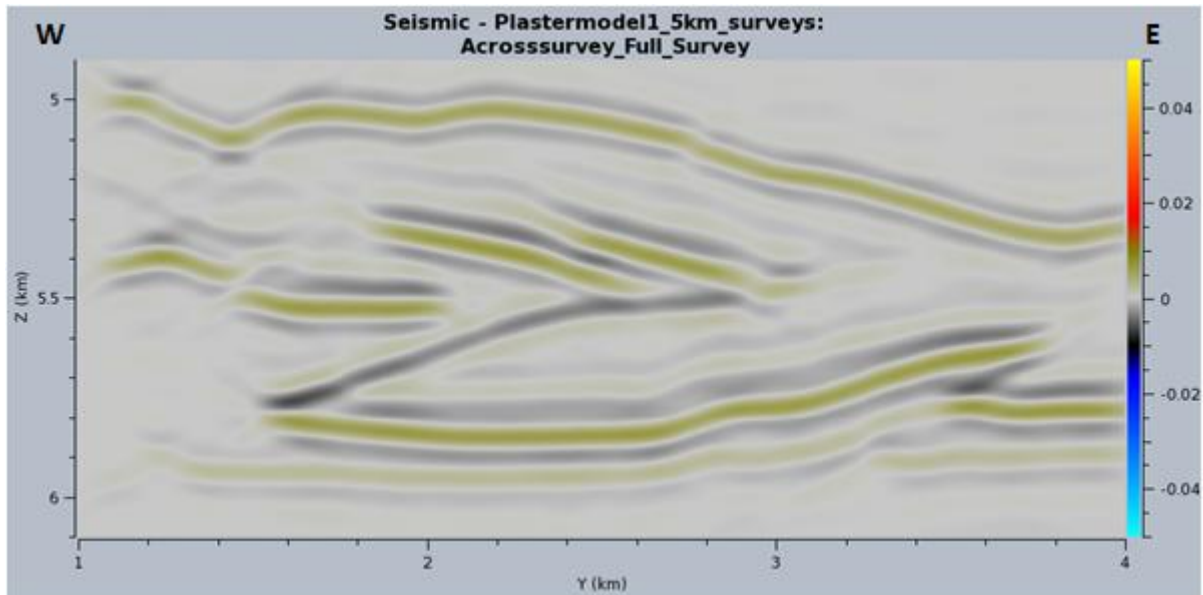
### 6.2.3 Strike- and dip survey at 5 km depth using Ricker zero 10 Hz frequency.

Figure 6.7 and Figure 6.8 shows the resulting seismogram of a dip- and strike survey where the target is placed at 5 km depth, using Ricker zero 10 Hz frequency wavelet.

Here, the reflectors, both side lobes and main lobes, are wider and have lower reflection amplitudes than the previously discussed seismograms. The noise is also smeared out even more.

Most of the faults mentioned earlier are barely evident or completely absent (i.e. the backthrusts) in these seismograms, although the major thrust fault is still visible. Still, it

displays shorter horizontal extension than in the previously. There is not such noticeable differences between the dip- and strike survey seismograms at this depth with adjoining frequency wavelet as for the other survey configurations.



**Figure 6.7:** Contractional plaster model seismogram at 5 km depth as a result of a dip survey, using Ricker zero 10 Hz frequency wavelet. The seismic velocities and density have been increased by 20 %.

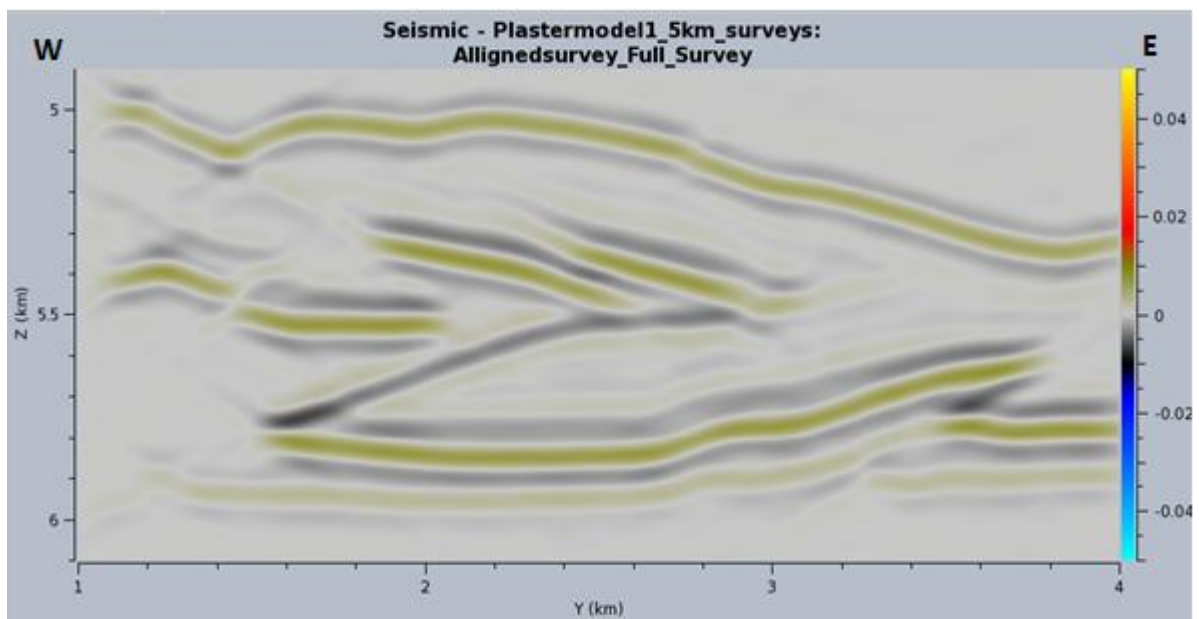


**Figure 6.8:** Contractional plaster model seismogram at 5 km depth as a result of a strike survey, using Ricker zero 10 Hz frequency wavelet. The seismic velocities and density have been increased by 20 %.

#### 6.2.4 Azimuth and dip of potentially illuminated reflectors

*Polar plots* are useful when characterizing illumination properties and are displayed in terms of illumination vectors, calculated from ray tracing (Figure 7.9). Two wavefield vectors ( $\mathbf{K}_R$  and  $\mathbf{K}_S$ ), defines the illumination vector (See Chapter 3.4.2) and each shot-receiver pair provides one vector. Hence, based on survey configurations, a collection of vectors are defined. As a result, only dips perpendicular to the vector is illuminated. Also, the vector length is proportional to the resolution limitation caused by the overburden. The vectors are associated with a dip angle and azimuth direction, which makes it easy to recognize the dips that are illuminated (Drottning, Branston, & Lecomte, 2009).

Figure 6.9 - Figure 6.11 shows the azimuth and dip of potentially illuminated reflectors for the contractional plaster model associated with the different survey directions. The dip azimuth ranges from  $0^\circ$  -  $360^\circ$ , where both represent the direction of north. The angle the reflector make with the horizontal is known as the dip angle, and ranges between  $0^\circ$  -  $90^\circ$ . The illumination vectors are perpendicular to its associated potential reflectors and the angle an illumination vector makes to the vertical is also represented by the dip angle. Each colored dot in the polar plots refer to a number of illumination vectors inside that dot, correlated to the color scale on the right hand side.

Figure 6.9 displays a polar plot from a dip survey (left) and strike survey (right) from the target placed at 1 km depth. A full range of dips and azimuths that can be illuminated are shown, where the dip angle is varying from a minimum of  $65^\circ$  in the crossline direction (N-S) to a maximum of  $70^\circ$  in the inline direction (W-E) for the dip survey polar plot. Still, the maximum dip is  $75^\circ$ , outside the inline- and crossline direction. The dip azimuth is represented in every direction ( $0^\circ$  -  $360^\circ$ ) on both polar plots. There is also a fairly dense distribution of illumination vectors on the southwestern side of the dip plot (red color), with dip ranging from  $60^\circ$  -  $65^\circ$ . The strike survey plot has a dip angle of potentially illuminated reflectors that vary from a minimum of  $65^\circ$  (crossline direction) to a maximum of  $80^\circ$  (inline direction). The densest distribution of illumination vectors are located in the northeast, southeast, southwest and northwest, also with dips ranging from  $60^\circ$  -  $65^\circ$ .

In general, the dip survey plot displays a higher number and a wider range of illuminated vectors than the strike survey plot, as seen from the color scheme.

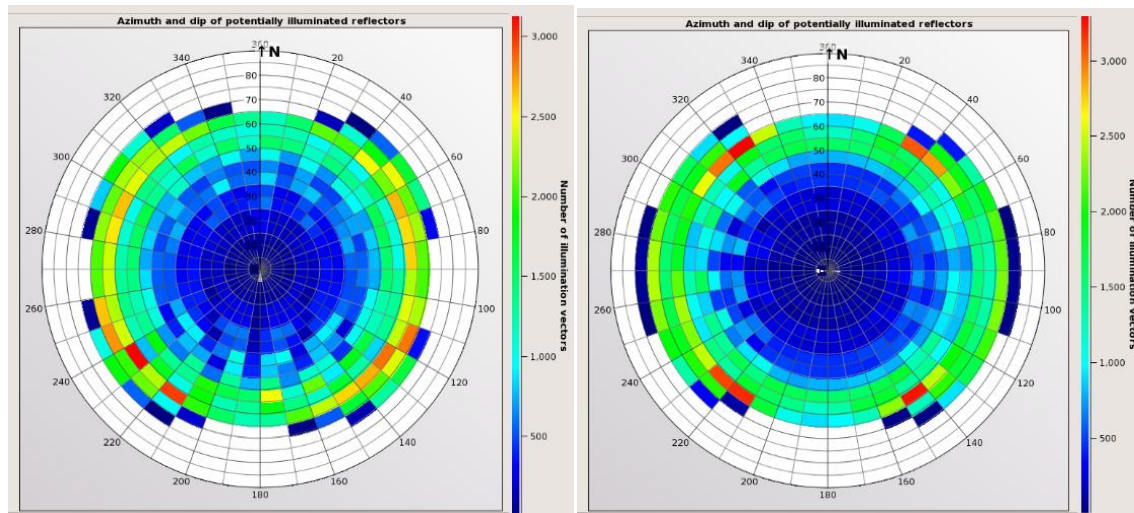


**Figure 6.9:** Azimuth and dip of potentially illuminated reflectors from a dip survey at depth of 1 km (left) and a strike survey at 1 km depth (right).

Figure 6.10 shows a less widespread plot of illuminated reflectors. The dip survey (left) with the target placed at 3 km depth shows a dip angle ranging from a minimum of  $40^\circ$  (inline direction) to a maximum of  $45^\circ$  (crossline direction), and a full range dip azimuth in both polar plots. The densest distribution of illumination vectors are present in the northeast, southeast, southwest and northwest, dip azimuth ranging from  $40^\circ - 45^\circ$ . The strike survey polar plot (right) shows a dip angle of  $45^\circ$  all around. The densest distribution of illumination vectors are located in the northern and southern part of the plot. There is a higher number of illuminated vectors in the strike survey plot than in the dip survey plot, as seen from the color scheme (particularly the red color).

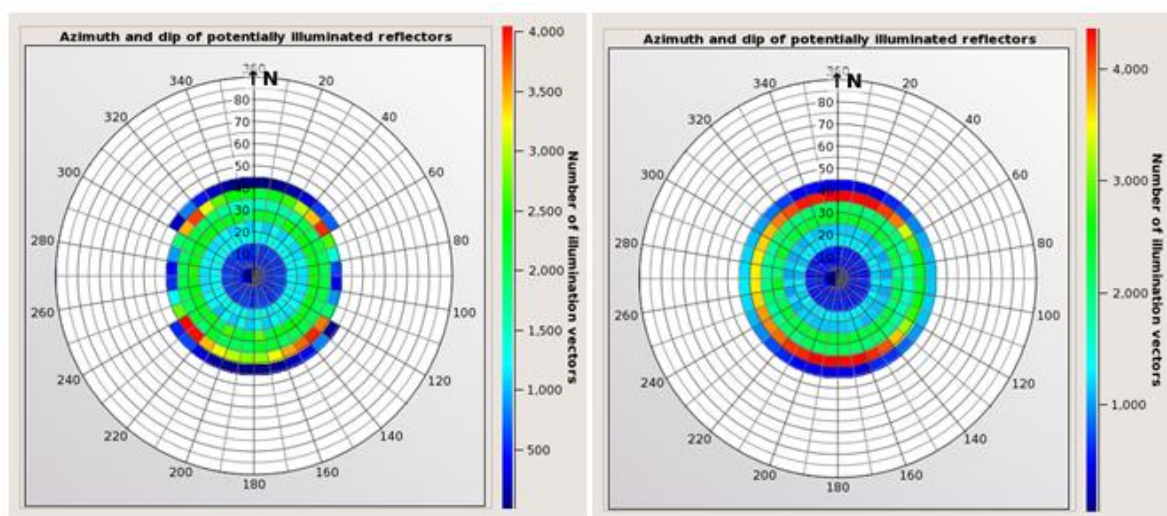


**Figure 6.10:** Azimuth and dip of potentially illuminated reflectors from a dip survey at depth of 3 km (left) and a strike survey at 3 km depth (right). Both show an increase of 10 % in regards to S-wave velocity, P-wave velocity and density.

Figure 6.11 shows a even lower widespread plot of illuminated reflectors. The dip survey (left) with the target placed at 5 km depth, shows a dip angle ranging from a minimum of  $25^\circ$  (inline direction) to a maximum of  $30^\circ$  (crossline direction), and a dip azimuth from  $0^\circ$  -  $360^\circ$ . The densest distribution of illumination vectors are present to the northeast, southeast, southwest and northwest, dip ranging from  $25^\circ$  -  $30^\circ$ .

The strike survey plot (right) shows a dip angle of  $30^\circ$  all around, with a dip azimuth from  $0^\circ$  -  $360^\circ$ . The densest distribution of illumination vectors are located to the west, dip ranging from  $25^\circ$  -  $30^\circ$ .

The largest number of illuminated vectors are found in the strike survey polar plot.

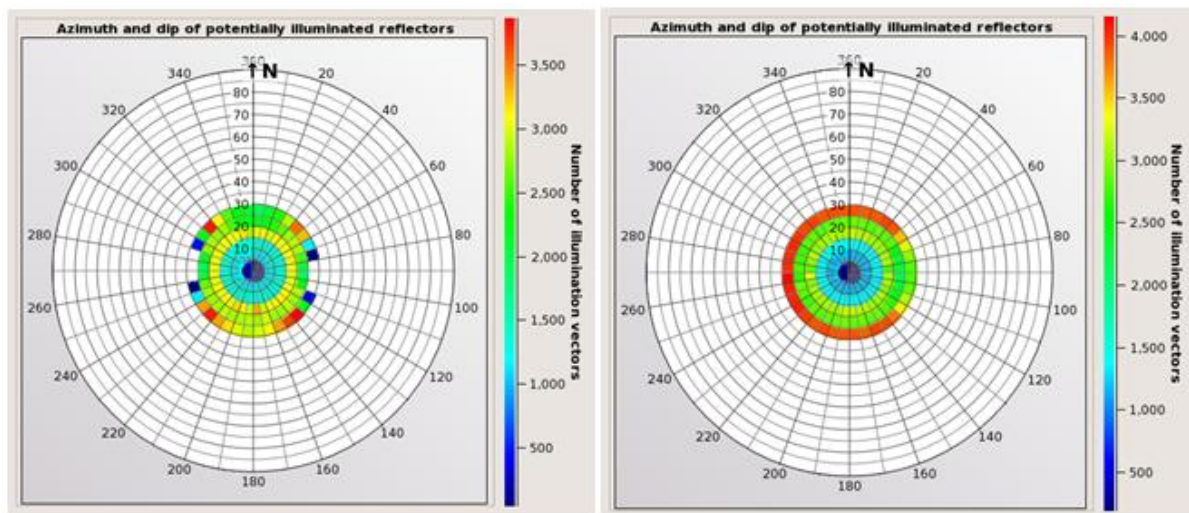


**Figure 6.11:** Azimuth and dip of potentially illuminated reflectors from a dip survey at depth of 5 km (left) and a strike survey at 5 km depth (right). Both show an increase of 20 % in regards to S-wave velocity, P-wave velocity and density.

### 6.3 Extensional plaster model

Figure 6.12 and Figure 6.13 below shows the resulting seismograms of a dip- and strike survey, respectively. The target is placed at 1 km, 3 km and 5 km, with adjoining frequency wavelets and velocities. Further discussion regarding each depth is shown in the following.

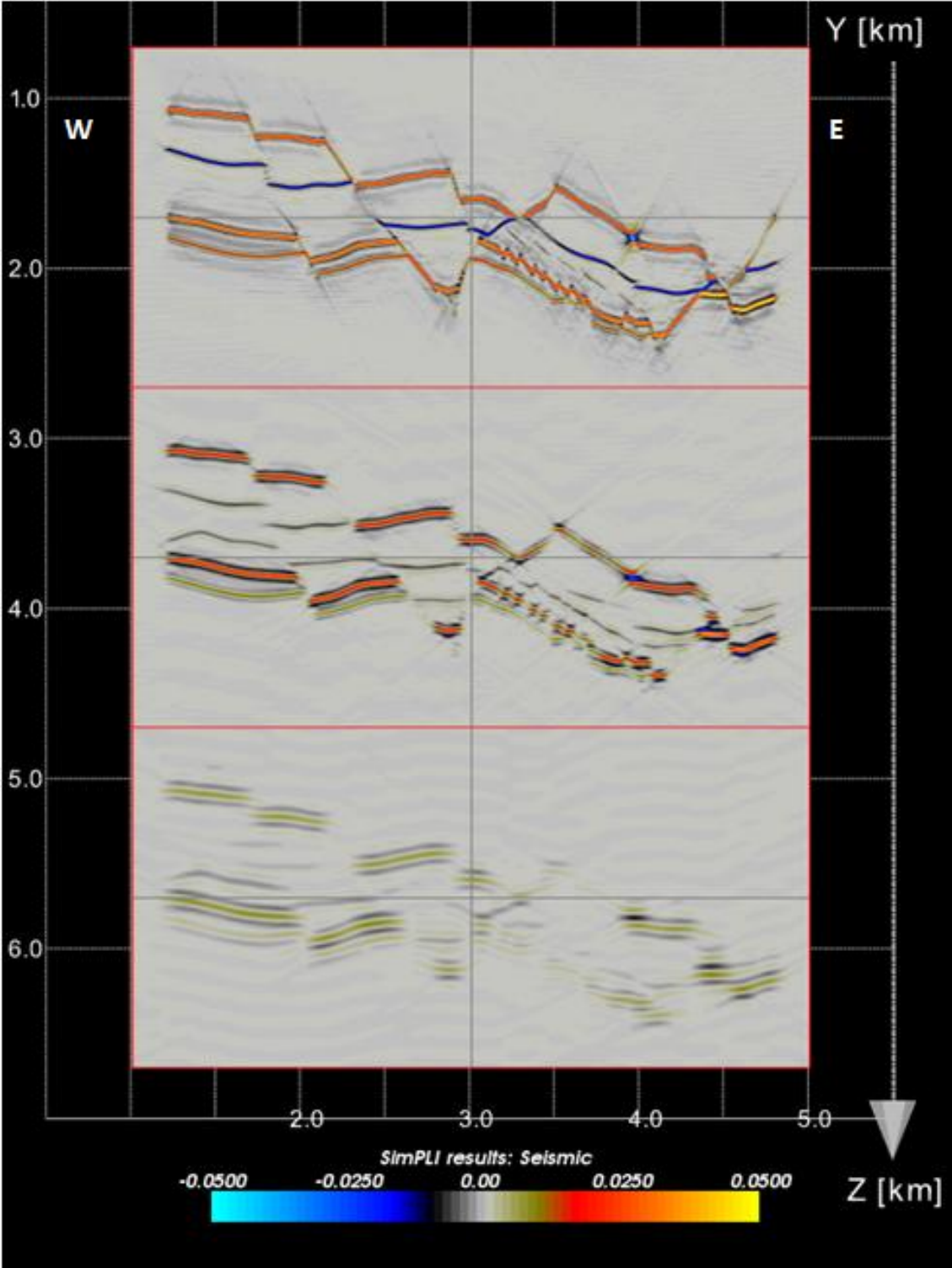


**Figure 6.12:** Extensional plaster model seismograms as a result of a dip survey, with target placed at depths of 1 km, 3 km and 5 km.

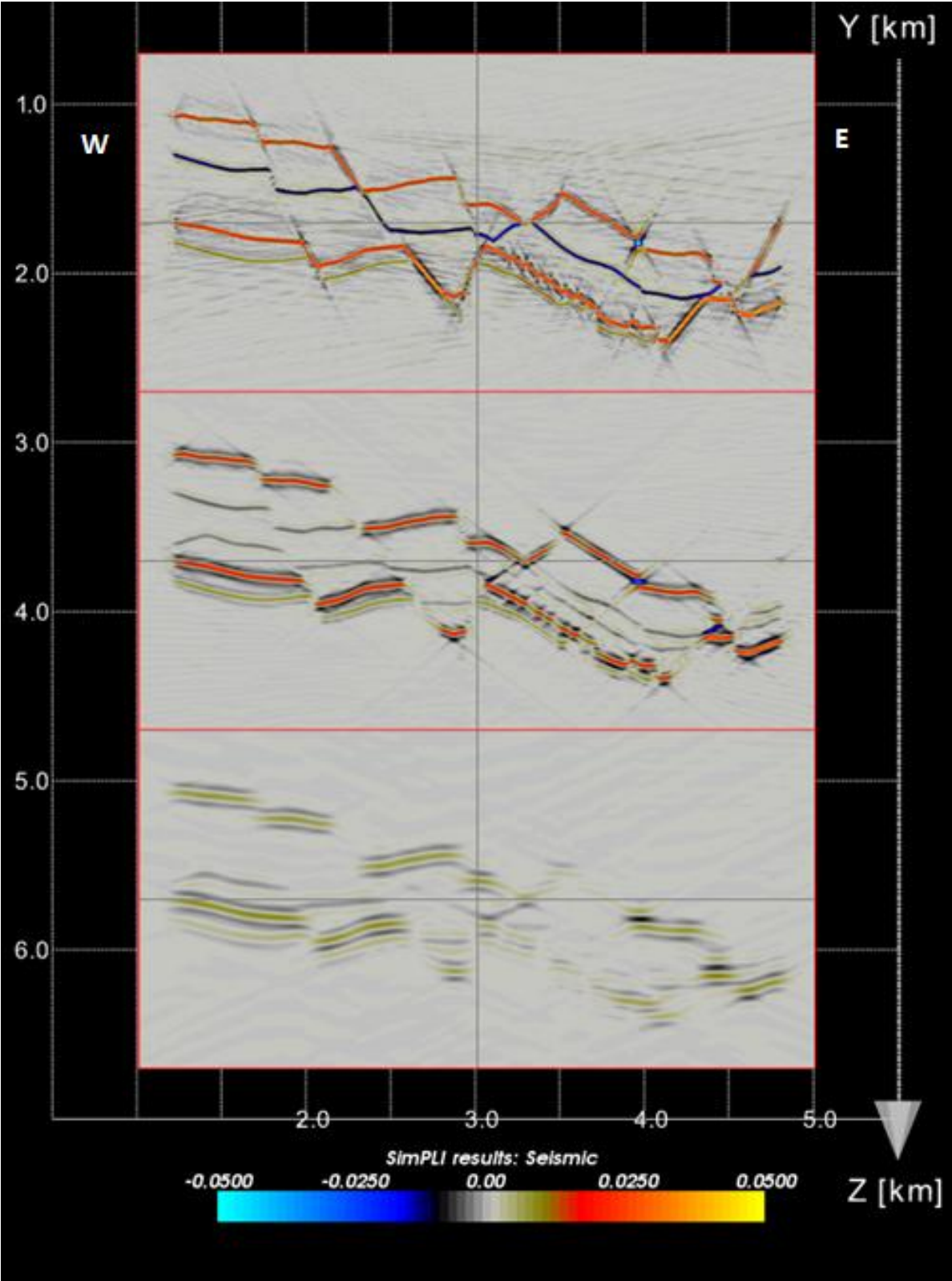
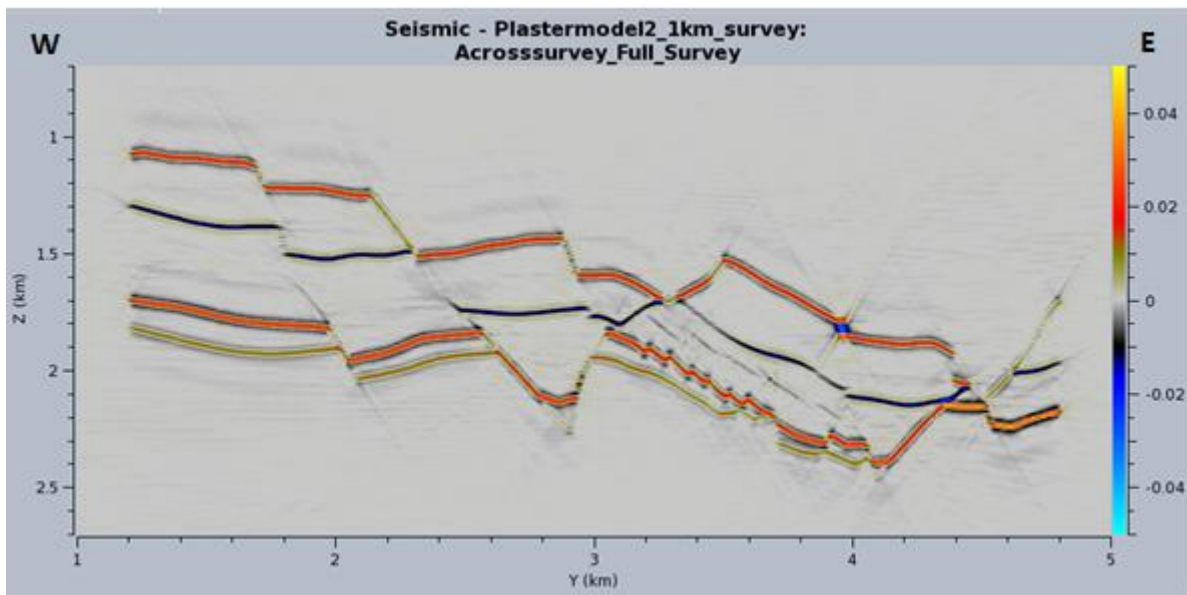


**Figure 6.13:** Extensional plaster model seismograms as a result of a strike survey, with target placed at depths of 1 km, 3 km and 5 km.

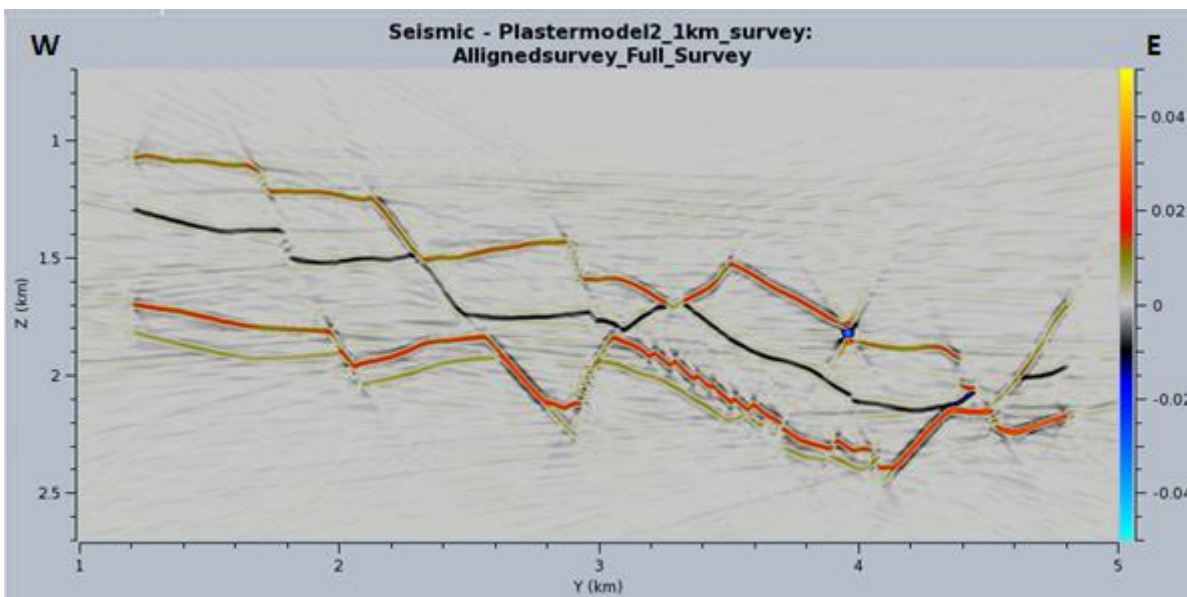
### 6.3.1 Strike- and dip survey at 1 km depth using Ricker zero 30 Hz frequency.

Figure 6.14 and Figure 6.15 below shows the resulting seismogram of a dip- and strike survey, respectively. Both models are placed at 1 km depth, using Ricker zero 30 Hz frequency wavelet.

As expected based on the previous results in section 6.2, the synthetic seismogram from the strike survey contain more noise and have weaker reflection strength than the dip survey seismogram.



**Figure 6.14:** Extensional plaster model seismogram at 1 km depth as a result of a dip survey, using Ricker zero 30 Hz frequency wavelet.



**Figure 6.15:** Extensional plaster model seismogram at 1 km depth as a result of a strike survey, using Ricker zero 30 Hz frequency wavelet.



The original model drawn in NORSAR-2D contained several layers assigned with different properties, yet all the layer boundaries are not displayed in either of the seismograms. The domino faulted area is displayed as a curvy reflector and in the middle of the section, west of the domino faults, a graben area is nicely displayed in both seismograms in addition to a horst to the east.

### **6.3.2 Strike- and dip survey at 3 km depth using Ricker zero 20 Hz frequency.**

Figure 6.16 and Figure 6.17 below shows the resulting seismogram of a dip- and strike survey, respectively. Both models are placed at 3 km depth, using Ricker zero 20 Hz frequency wavelet.

There is more noise present in the strike survey seismogram than in the dip survey seismogram. The reflectors are wider and less resolved in both seismograms at this depth, more so for the strike survey seismogram than the dip survey seismogram. Reflections along the fault planes are completely absent, but the near horizontal reflectors are still sufficiently displayed. When it comes to the domino faulted area, the strike survey seismogram provides a more consistent curvy reflector than the dip survey configuration seismogram. The graben area is still sufficiently displayed in both seismograms, but the horst can be more difficult to determine. All dipping reflectors (i.e. fault planes) that were displayed in the previous model are not represented here.

In the previous model at 1 km depth, some originally drawn layer boundaries are missing, but in this case, all layer boundaries are represented, but vaguely so.

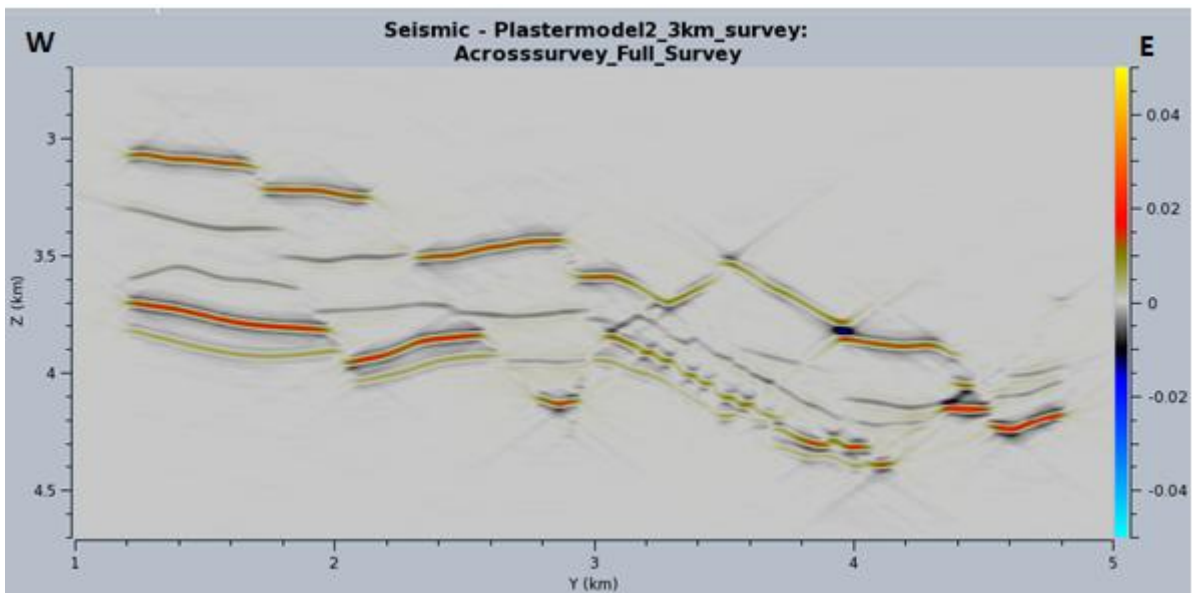


**Figure 6.16:** Extensional plaster model seismogram at 3 km depth as a result of a dip survey, using Ricker zero 20 Hz frequency wavelet.

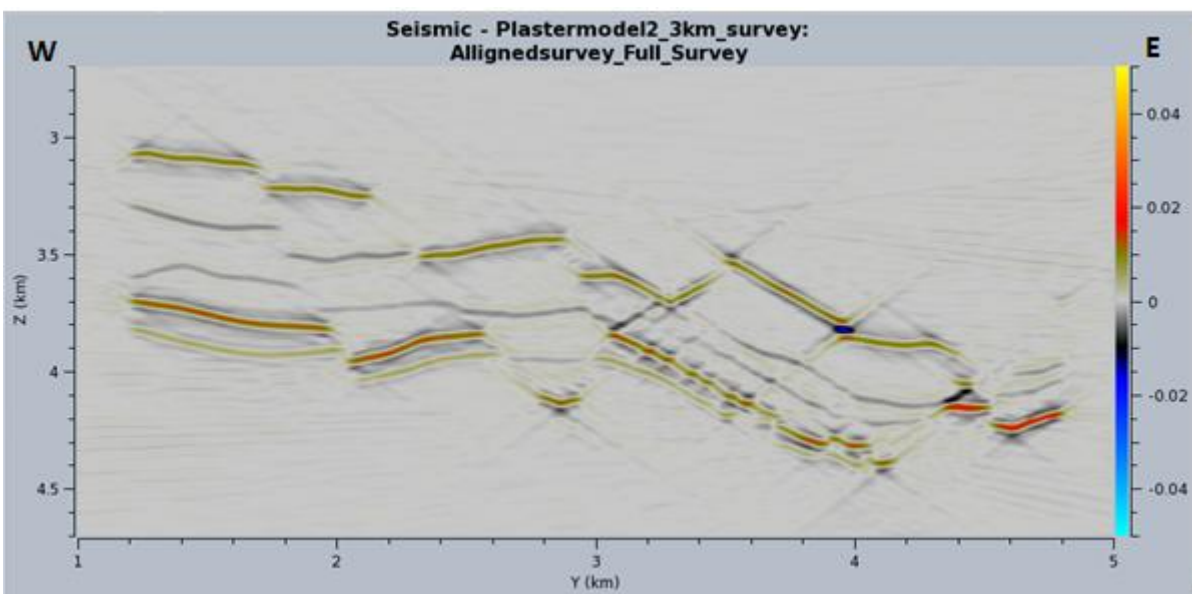


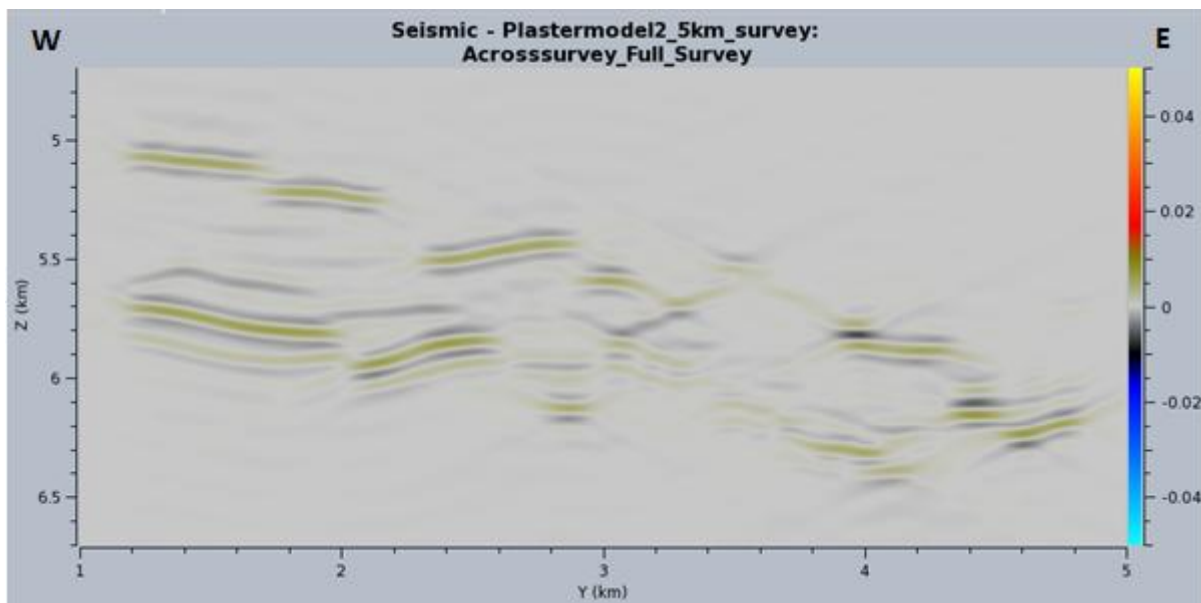
**Figure 6.17:** Extensional plaster model seismogram at 3 km depth as a result of a strike survey, using Ricker zero 20 Hz frequency wavelet.

### 6.3.3 Strike- and dip survey at 5 km depth using Ricker zero 10 Hz frequency.

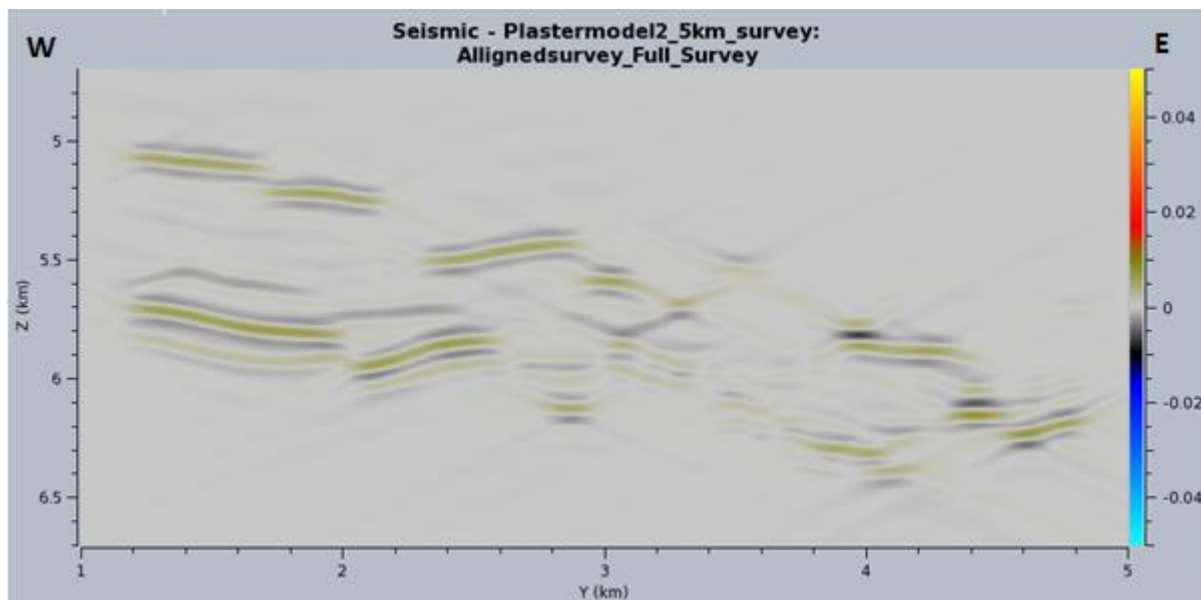
Figure 6.18 and Figure 6.19 below shows the resulting seismogram of a dip- and strike survey, respectively. Both models are placed at 5 km depth, using Ricker zero 10 Hz frequency wavelet.

The strike survey seismogram still display more noise than the dip survey seismogram, although very smeared out. The reflectors are also wider for both survey configurations.

As expected, the reflectors are more pronounced in the dip survey seismogram than the strike survey seismogram, but less evident than for previously displayed results. The domino faulted area is not visible on either of the seismograms, which makes the whole area distorted and confusing. Also, the graben area in the center may be perplexing when interpreting due to the surrounding faults that are (or should be) present on both sides of the graben, whilst the horst is completely absent.



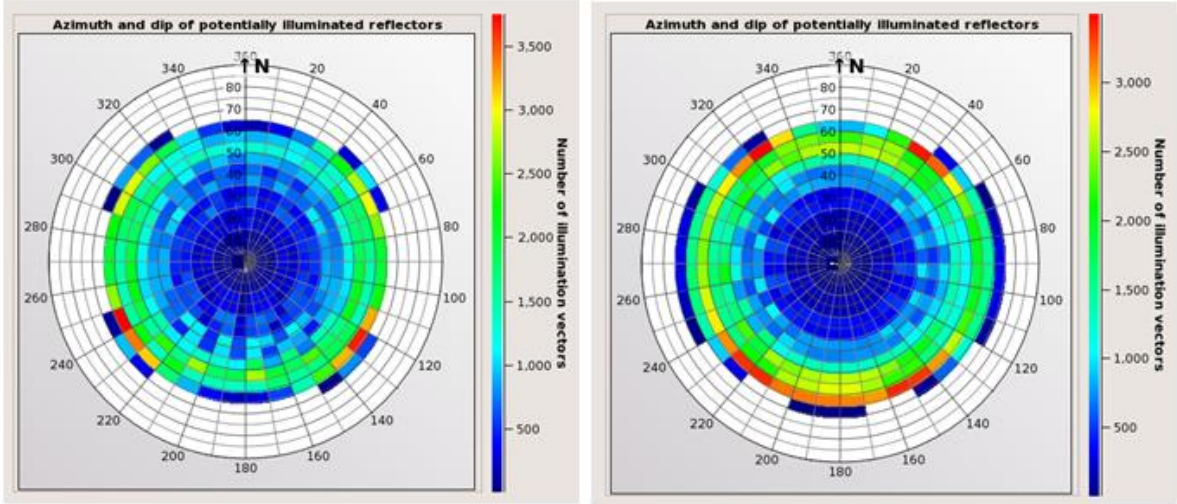
**Figure 6.18:** Extensional plaster model seismogram at 5 km depth as a result of a dip survey, using Ricker zero 10 Hz frequency wavelet.



**Figure 6.19:** Extensional plaster model seismogram at 5 km depth as a result of a strike survey, using Ricker zero 10 Hz frequency wavelet.

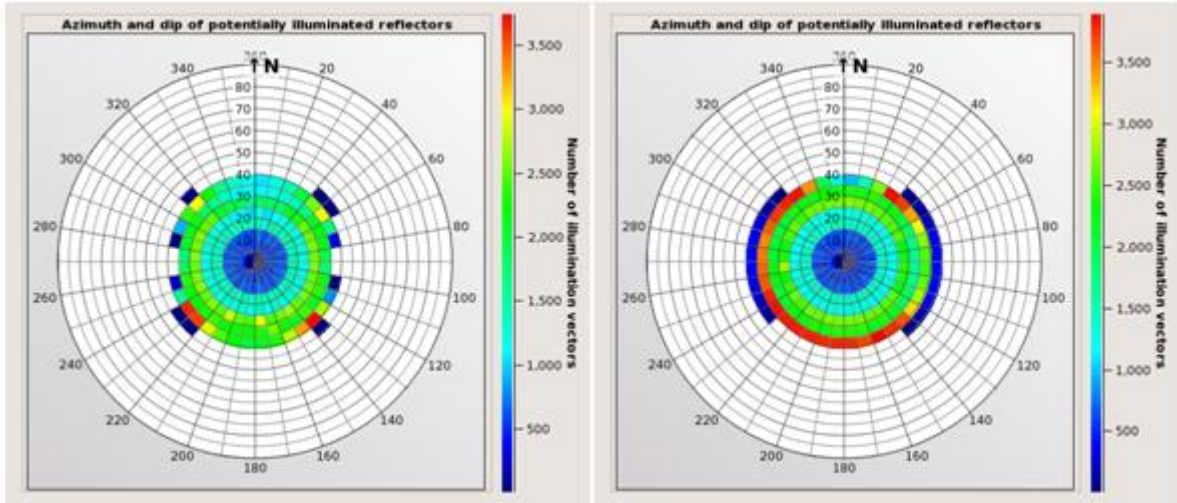
**6.3.4 Azimuth and dip of potentially illuminated reflectors**

Figure 6.20 displays a polar plot from a dip survey (left) and strike survey (right) for the target placed at 1 km depth. The dip angle of potentially illuminated reflectors are ranging from a minimum of 65° (crossline- and inline direction) to a maximum of 70° outside the crossline and inline for the dip survey polar plot. The dip azimuth is represented in every direction (0° - 360°) on both polar plots. The densest distribution of illumination vectors are found in the southeast and southwest, with a dip ranging from 60° - 65°. The strike survey polar plot shows a dip angle of potentially illuminated reflectors from 65° (crossline direction) - 75° (inline direction). The densest distribution of illumination vectors is located in the south, northwest and northeast, dips raging from 60° - 65°.



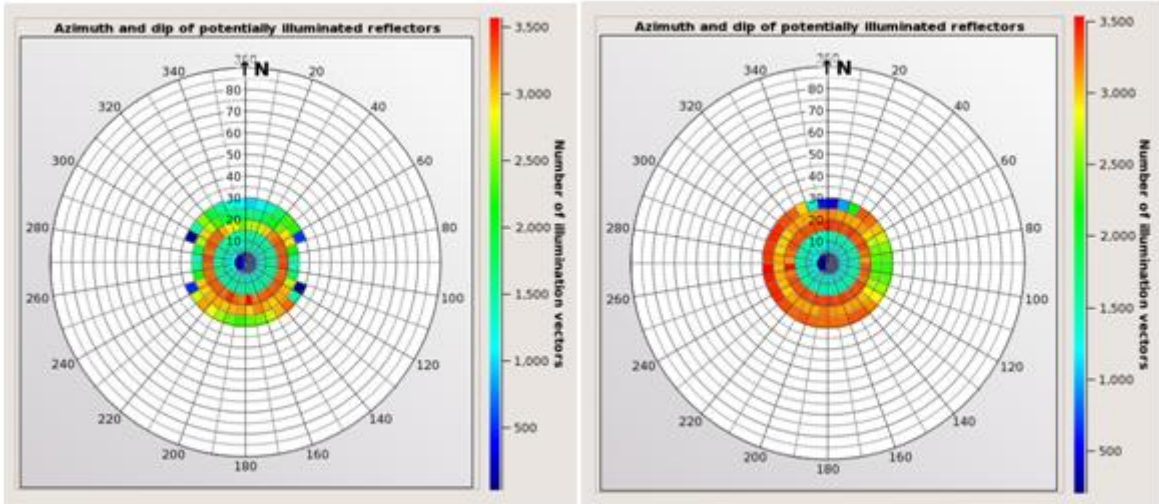
**Figure 6.20:** Azimuth and dip of potentially illuminated reflectors from a dip survey at depth of 1 km (left) and a strike survey at 1 km depth (right).

Figure 6.21 shows polar plots from the target placed at 3 km depth. Both of them are less widespread when it comes to dip angle, but the dip azimuth is full range from 0° - 360°. The dip survey polar plot (left) shows a dip angle ranging from 40° (crossline direction) - 35° (inline direction), and the largest dip represented is 45° outside the inline- and crossline direction. The densest distribution of the illumination vectors are located to the southeast and southwest, dip ranging from 35° - 40°. The strike survey polar plot (right) shows a dip of 40° in the crossline direction and 45° in the inline direction, and a much denser distribution of illumination vectors in the entire dip azimuth from 35° - 40°.



**Figure 6.21:** Azimuth and dip of potentially illuminated reflectors from a dip survey at depth of 3 km (left) and a strike survey at 3 km depth (right). Both show an increase of 10 % in regards to S-wave velocity, P-wave velocity and density.

Figure 6.22 shows an even lower widespread of illuminated reflectors. The dip survey (left) with the target placed at 5 km, shows a dip angle ranging from 25° (inline direction) - 30° (crossline direction), and dip azimuth from 0° - 360° in both polar plots. There is a fairly dense distribution of illumination vectors in the entire plot, the densest with dip angle from 15° - 20°. The strike survey plot (right) displays a dip angle of 30° through the entire plot, with nearly all illumination vectors being dense (orange and red color).



**Figure 6.22:** Azimuth and dip of potentially illuminated reflectors from a dip survey at depth of 5 km (left) and a strike survey at 5 km depth (right). Both show an increase of 20 % in regards to S-wave velocity, P-wave velocity and density.

## 7 Discussions

### *Frequencies of the wavelets*

In general, the reflectors in the seismograms become wider with depth. Higher frequencies provide better resolution than lower frequencies, but the higher frequencies have stronger attenuation with depth compared to the lower frequencies. Hence, resolution becomes poorer with depth (Rafaelsen, 2006). Reflections are strictly based on the elastic properties and densities assigned to each rock layer. The higher frequencies are reflected from relatively shallow reflectors, whilst the lower frequencies reach a larger depth before being reflected. The seismic velocity in general increase with depth due to compaction of sediments further down in the subsurface, which is why a velocity- and density increase of 10 % and 20 % were applied to depths of 3 km and 5 km, respectively.

### *Missing layer boundaries*

The repetition of layers is what have caused some layer boundaries to "disappear" due to same elastic properties above and below the layer boundary (same acoustic impedance). But, some layer boundaries that should be present due to difference in acoustic impedance are not represented in all synthetic seismograms. Figure 7.1 - Figure 7.6 shows this effect, where 6 reflectivity series with associated seismograms are displayed. Figure 7.1 shows a seismogram and reflectivity series as a result of an incident angle of  $0^\circ$ , and a IVEC (illumination vector) range of  $0^\circ - 5^\circ$ , where the layer boundaries between the Unknown Formation and Draupne Formation are missing (see Figure 5.5 - 5.7). In Figure 7.2, the incident angle is  $10^\circ$  and the IVEC range of  $0^\circ - 5^\circ$ . Here, the same horizons are missing, and the ones that are represented are slightly stronger than for  $0^\circ$ . Increasing the incidence angle to  $20^\circ$  and IVEC range to  $15^\circ - 25^\circ$ , Figure 7.3 displays all the originally drawn horizons. The reflections aren't particularly strong, but present. Further, the reflectivity series and seismogram as a result of an incidence angle of  $30^\circ$  and  $40^\circ$  (IVEC range of  $25^\circ - 35^\circ$  and  $35^\circ - 45^\circ$ , respectively) as shown in Figure 7.4 - Figure 7.5, display all originally drawn horizons, even though not particularly strong. Finally, the summation of all the previously shown seismograms and reflectivity series give the end result of Figure 7.6. This summation leads to the layer boundaries between the Draupne Formation and Brent Group missing.

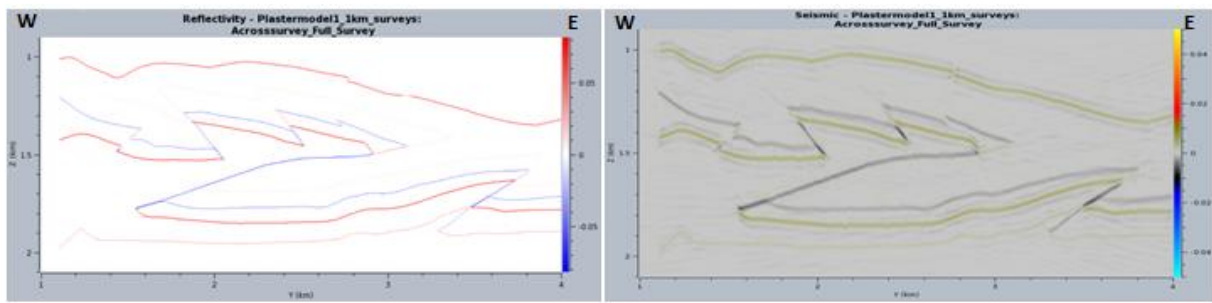


**Figure 7.1:** Incident angle:  $0^\circ$ , IVEC range:  $0^\circ - 5^\circ$ .

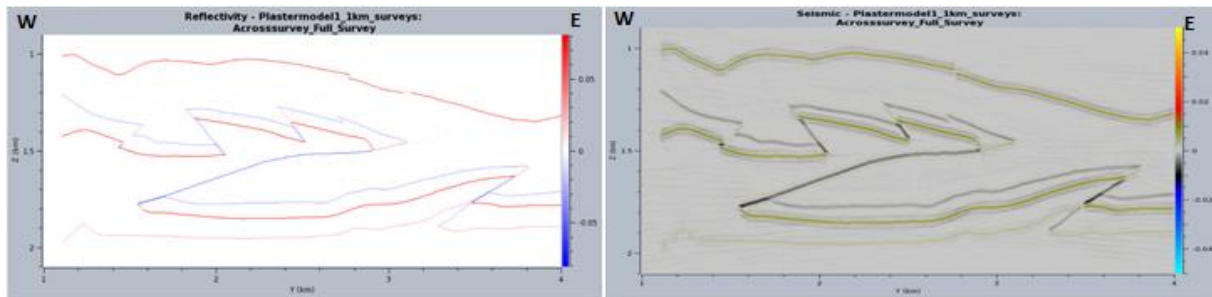


**Figure 7.2:** Incident angle:  $10^\circ$ , IVEC range:  $5^\circ - 15^\circ$ .

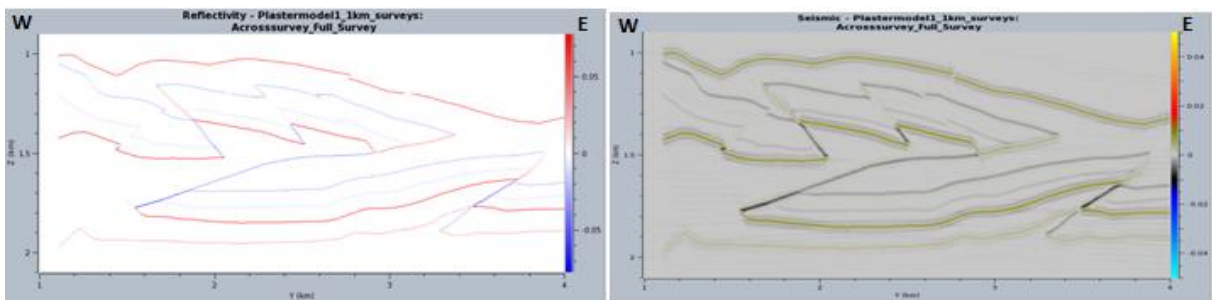


**Figure 7.3:** Incident angle:  $20^\circ$ , IVEC range:  $15^\circ - 25^\circ$ .

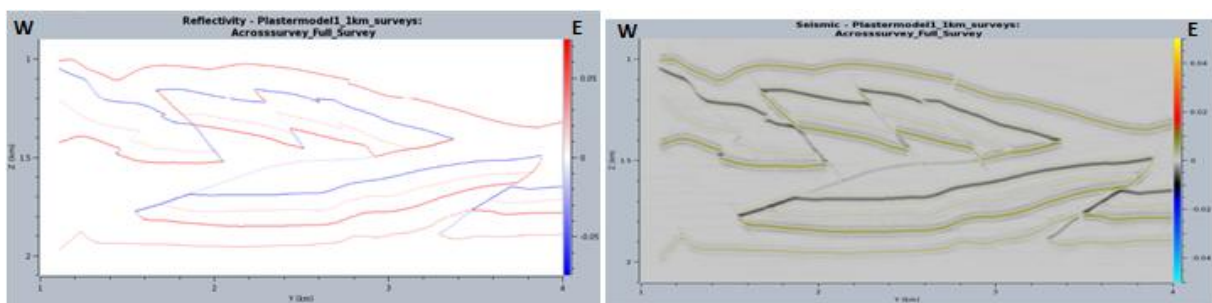


**Figure 7.4:** Incident angle:  $30^\circ$ , IVEC range:  $25^\circ - 35^\circ$ .

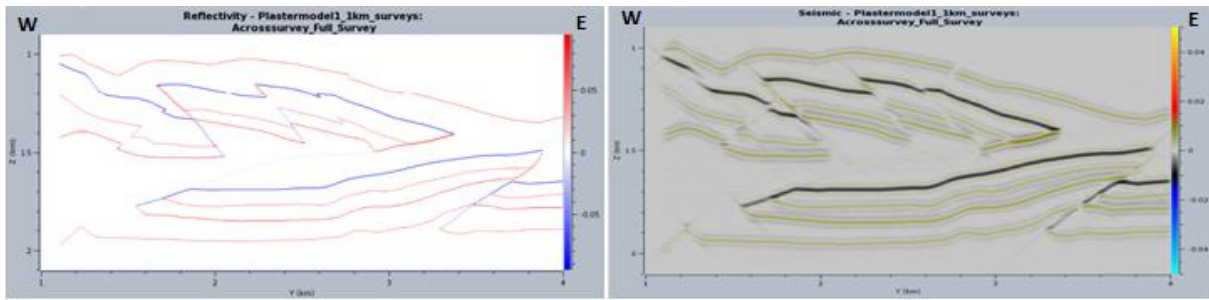


**Figure 7.5:** Incident angle:  $40^\circ$ , IVEC range:  $35^\circ - 45^\circ$ .

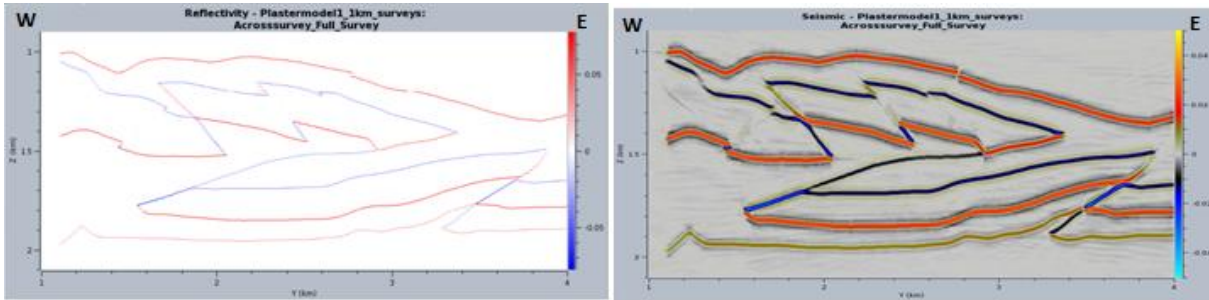


**Figure 7.6:** Average reflectivity. Incident angle sum. IVEC range:  $0^\circ - 45^\circ$ .

The CREWES Reflectivity Explorer (CREWES, 2001-2005) was used to calculate the reflection coefficient, and the resulting plot is shown in Figure 7.7 below. It displays the wavefield in form of magnitude and phase on the vertical axis and the angle of incidence on the horizontal axis.

By selecting the upper and lower velocities and density of layer boundaries with no reflection, the Draupne Formation and Brent Group (respectively) were chosen and the Zoeppritz-Knott reflection coefficient was calculated and plotted in polar form. The magnitude is either negative or positive in order so that the phase is always zero below the first critical angle. Thus, when below the critical angle, there is no change in phase. In the resulting plot in Figure 7.7, the magnitude is below zero until it reaches an angle of incidence of  $\sim 22^\circ$  (a negative value of magnitude implies a phase change of  $180^\circ$  in the reflected ray (Gelius & Johansen, 2010)). There is a negative and positive magnitude in the plot, both being approximately equal in size and may cancel each other out. Also, the magnitude is so small that only a tiny percentage of the incidence wave energy is reflected back to the receiver. This leads to a poorly noticeable reflector in the seismograms.



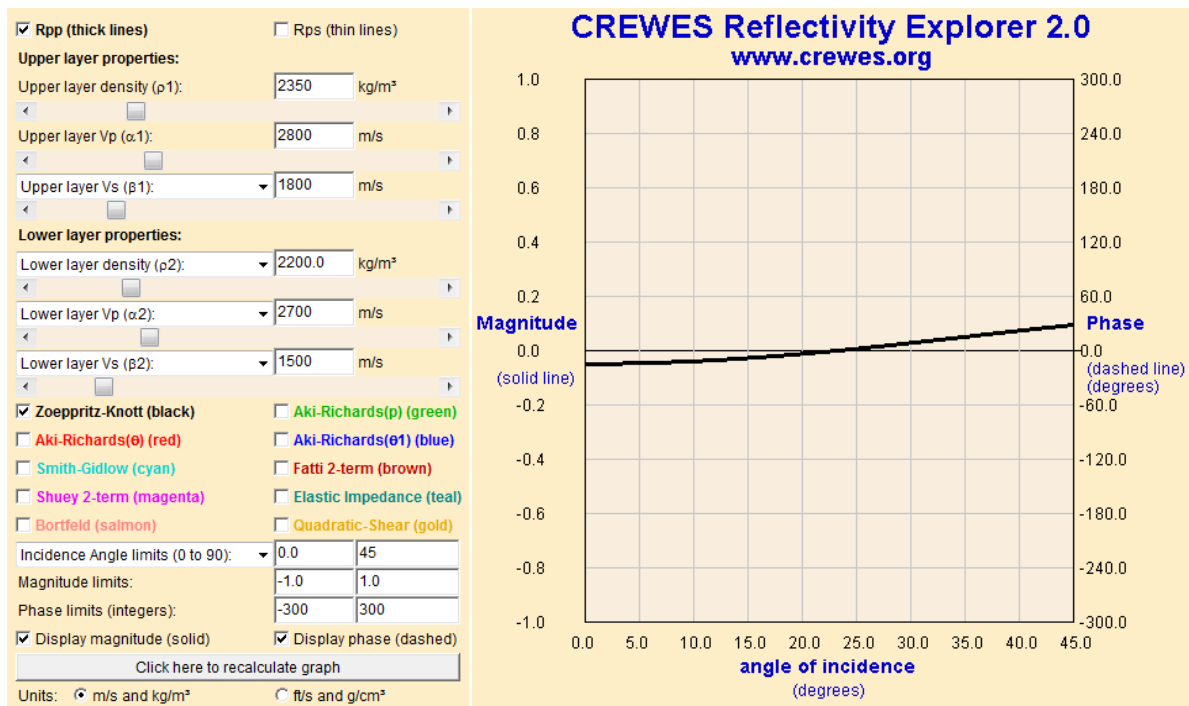


**Figure 7.7:** The control window where the elastic properties of the formations are computed (left). Here, the values of the Draupne Formation (top) and Brent Group (bottom) is shown and calculated using the Zoeppritz-equation. The resulting plot is shown to the right.

The same plot is made between two layers where the layer boundary is present in the resulting seismogram and reflectivity series. Thus, the reflection coefficient between the Unknown Formation and Draupne Formation (see Figure 5.5 - 5.7) were calculated and plotted (Figure 7.8). The plot is fairly different from the previous one, as the magnitude goes from a slightly positive value at zero-incidence to a negative value. The magnitude in this plot is somewhat larger than the previous example, meaning that more of the incidence wave energy is reflected and displayed as a reflection in the seismograms.

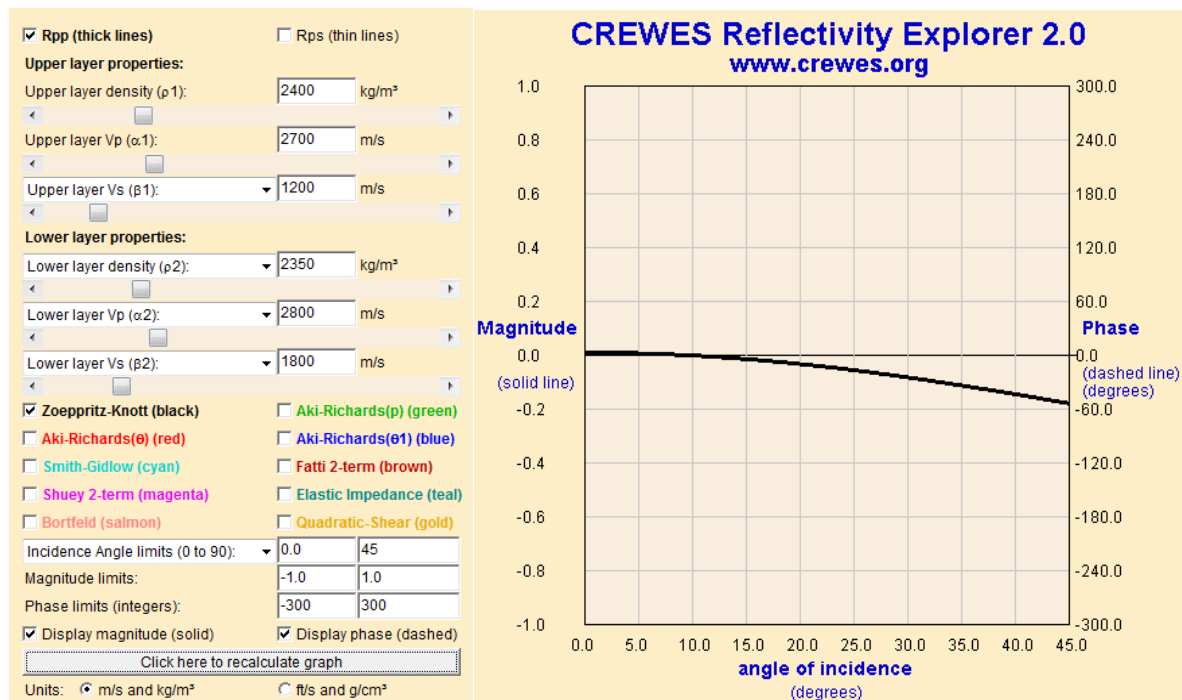


**Figure 7.8:** The control window where the elastic properties of the formations are computed (left). Here, the values of the Unknown Formation (top) and Draupne Formation (bottom) is shown and calculated using Zoeppritz-Knott. The resulting plot is shown to the right.

### "Empty" seismograms

Some of the seismograms are "empty", even though the reflectivity series are present. This occurs for both the contractional- and extensional plaster model at incidence angle of 40° (IVEC range: 35° - 45°) at 3 km depth (See Appendix B for example), both for the dip- and strike survey configurations. Also, for the contractional- and extensional plaster model at 5 km depth, the same effect is seen for both 30° and 40° incidence angle.

An explanation can be given by defining a shot S, a receiver R and a point P in the subsurface. The wavefield from S in P can be described by a vector  $\mathbf{K}_S$  and also, the wavefield from P that is registered in R can be described by a vector  $\mathbf{K}_R$  (Figure 7.9). The illumination vector (IVEC) is then the difference between the two:  $\mathbf{K} = \mathbf{K}_R - \mathbf{K}_S$ . If a shot from S is reflected in P and registered in R, a reflector in P perpendicular to  $\mathbf{K}$  in P is needed, and also, the geology in P needs a specific dip in order to provide a seismic reflection to be registered in R (i.e. no diffractions). Hence, IVEC says something about which geological dips that can be registered in a seismic survey. If we have many shots and receivers, a collection of dips is gathered and can be seismically registered. This means that if a dip does not lie in the range of IVEC, a seismic signal will not be produced despite the reflector having a strong reflection coefficient (Drottning et al., 2009).

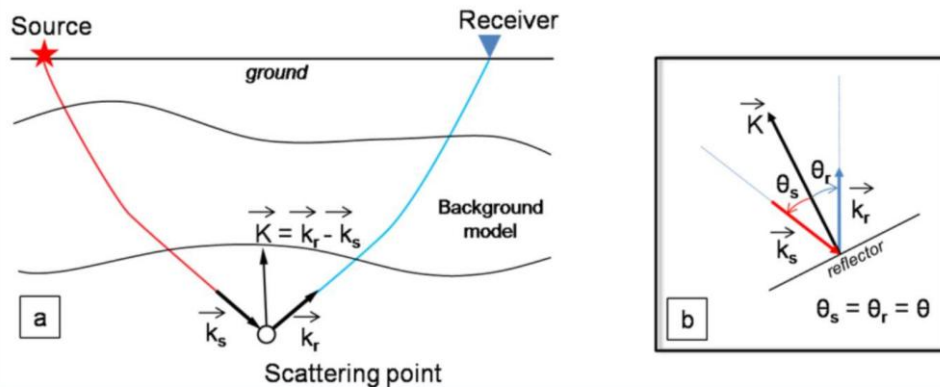


**Figure 7.9:** Definition of the illumination vector by ray tracing (From Drottning, Branston, & Lecomte, 2009).

### *Dipping reflectors*

The near horizontal reflectors are properly displayed in all resulting seismograms, but the dipping reflectors are not. If the distance between the source and receiver was larger in the seismic modeling, better target coverage could be obtained. The reflected energy from the target may not reach the receiver position since the target placed at 3 km and 5 km versus 1 km leads to longer traveling distance, hence a larger spread in the wave energy. This also depends on the dip of the rock layers, which, depending on which direction they dip, may lead to the reflected energy not being detected by the receivers. The combination of these two factors may explain why the dipping reflectors are not properly displayed in the seismograms, especially at 3 km and 5 km.

### *Seismic interpretation*

In the contractional plaster model seismograms, some of the backthrust faults are shown as reflections where the target is placed at 1 km (Figure 6.3), and assumptions based on offset in the reflectors at target depth of 3 km (Figure 6.5) is sufficient in order to interpret the section correctly. However, the target placed at 5 km depth (Figure 6.7) is not as easy to interpret due to wide- and lack of reflectors. This is also the case for the reverse faults on the eastern- and western side of the seismograms. The major thrust fault is displayed in all seismograms, although the extent is difficult to determine due to no difference in acoustic impedance of rock layers in the east and west. On seismic sections, faults are rarely directly imaged, as shown in the resulting seismograms of this thesis. More often, reflectors are truncated by faults, known as hanging-wall and footwall cut-offs, which are found by following the horizons until they terminate (Lines & Newrick, 2004).

The domino faulted area in the extensional plaster model at 1 km and 3 km depth is displayed as a curvy reflector, and should based on this be interpreted properly. At the same time, the vertical extent of the domino faults may be difficult to determine, as only the bottom faulted layer is reflected. The strong blue reflector above the "domino-reflector" is not faulted originally, as seen from the model drawn in NORSAR-2D, which means that the domino faults does not extend across that reflector. Still, if the different elastic properties below and above a layer boundary had been represented as reflectors, one could easily decide the domino faults extent. When the target is placed at 5 km depth, the area is distorted and reveals no sign of domino faults. This due to wide reflectors and lack of reflectors above a certain dip.

The resulting synthetic contractional- and extensional seismograms of 1 km and 3 km target depth using these survey configurations is not realistic seen from a resolution perspective and display the most optimal results possible. If one was to conduct a real life seismic survey, results similar to that found at target depth of 5 km would be most likely to be accomplished. Still, it provides information regarding the question of whether or not to conduct a strike- or dip survey in general, discussed in the following sections.

#### ***Azimuth and dip of potentially illuminated reflectors***

The distribution of illumination vectors implies that reflectors within a particular range will be especially illuminated in the simulated PSDM image for a survey configuration. There seems to be little connection between the distribution of illumination vectors and the seismic resolution, since the strike survey seismograms are less resolved and contain more noise than the dip survey seismograms. Yet, a larger number of illumination vectors in the strike survey polar plots are displayed in most cases. The reason for this might be that the registered illumination vectors represent every reflection information available, not only in regards to the structure, but also overburden effects.

For the dip survey polar plot of target placed at 1 km, dips larger than  $65^\circ$  the inline,- and crossline direction (W-E and N-S, respectively) will not be illuminated. Also, dips larger than  $75^\circ$  will not be illuminated in any other direction. For the strike survey polar plot, the largest dip illuminated in the crossline direction is also  $65^\circ$ , whereas in the inline direction it is  $80^\circ$ . This indicate that the strike survey have better resolution in the inline direction than in the crossline direction, whilst the dip survey have a fairly even resolution in all directions.

For the dip survey polar plot of target placed at 3 km, the maximum dip illuminated in the inline direction is  $40^\circ$  and  $45^\circ$  in the crossline direction. For the strike survey plot a maximum dip of  $35^\circ$  is illuminated in the crossline direction and  $45^\circ$  in the inline direction. Hence, there is a much larger dip range that is not illuminated in the strike survey seismograms than in the dip survey seismograms. This might explain the "clean" image obtained in the dip surveys compared to the strike surveys (i.e. noise).

For the dip survey polar plot of target placed at 5 km, dips larger than  $25^\circ$  in the inline direction and  $30^\circ$  in the crossline direction will not be illuminated. For the strike survey plot, dips larger than  $30^\circ$  in the inline direction and  $25^\circ$  in the crossline direction will not be illuminated. This indicates that both the strike survey and dip survey configuration provide relatively equal seismograms, which is also observed by looking at them.

### ***Dip-or strike survey?***

According to Long et al. (2004) and described in section 3.2.1, the shooting direction is highly dependent on the dimensions of the streamer spread, which affects the illumination coverage. The newest acquisition technology can use 12 - 16 streamers with down to 37.5 m spacing, which allows for tight 3D sampling. In this modeling, only 9 streamers with spacing of 100 meters have been used for the dip- and strike survey configuration. Hence, this should in theory lead to the same illumination coverage in both directions. Based on the previously discussed polar plots, the strike survey plots show a more regular illumination of dipping structures than the dip survey plots, which is also confirmed by previous studies. However, the polar plots represent the overall information obtained, i.e. not only information regarding the target.

Despite the resulting strike survey seismograms in this thesis being of poorer quality than the dip survey seismograms, they both reveal the same structures in a decent manner. Based on what would be expected in a real seismic survey, the strike survey seismograms are most realistic, in terms of noise and reflection amplitudes.

---

## 8 Conclusions

A 3D marine survey using two different survey configurations was modeled on two structurally different plaster models. It has been shown that the survey direction is important when it comes to illumination of dipping reflectors. It is also shown how resolution is dependent on frequency, in this study using zero phased wavelets of 30, 20 and 10 Hz center frequency.

Main findings:

- The dip survey seismograms display both higher resolution and a cleaner image than the strike survey seismograms.
- The seismograms of target placed at 1 km and 3 km are overly resolved and would not be achievable when conducting a real survey.
- The faults mainly have to be interpreted based on offsets of near-horizontal reflectors, since dipping reflectors are barely represented.
- Angle dependent reflectivity is of great importance in regards to reflectivity series and resulting seismograms, as some layer boundaries are not displayed as reflections for certain incidence angles.
- Wavelets of various center frequencies are crucial in regards to overall resolution. The wider the reflectors, the more complicated the subsurface structures are to interpret.
- The distance between source and receiver is essential in order to accomplish a correct sub-surface image, as dipping reflectors are not represented due to a longer traveling distance and therefore spread of reflected energy.
- The seismograms of target placed at 5 km depth using Ricker zero 10 Hz center frequency clearly shows the problems encountered when trying to interpret complex structures of this resolution.
- Regardless of survey direction, all seismograms display the same horizons as reflections. The only clear difference is the presence of noise and less amplitude in the strike survey seismograms. In reality, the strike survey seismograms provide a more realistic subsurface image, since the presence of noise is inevitable in real life.

The results shown are a direct product of knowledge regarding all aspects of the subsurface structures and properties. Hence, the synthetic seismograms show the absolute ideal image of a seismic section, and is most likely not achievable in real life.

*Suggested further work*

There are many possibilities when it comes to seismic modeling, and the modeling software used in this thesis can be very useful.

What if:

- the distance between the source and receiver was extended.
- If the survey configuration orientation was something other than strike/dip.
- Other frequency wavelets were applied.
- Additional horizons were drawn in NORSAR-2D.
- There was a velocity- and density change within each rock layer.
- The overburden was more complicated.

# References

- Bjorlykke, Knut. (2010). *Petroleum geoscience: From sedimentary environments to rock physics*: springer.
- Boyer, Steven E, & Elliott, David. (1982). Thrust systems. *AAPG Bulletin*, 66(9), 1196-1230.
- Brun, Jean-Pierre, & Tron, Virginie. (1993). Development of the North Viking Graben: inferences from laboratory modelling. *Sedimentary Geology*, 86(1), 31-51.
- Cloos, Ernst. (1955). Experimental analysis of fracture patterns. *Geological Society of America Bulletin*, 66(3), 241-256.
- CREWES. (2001-2005). CREWES The consortium for research in elastic wave exploration seismology. Available: <http://www.crewes.org/ResearchLinks/ExplorerPrograms/RefLEx/REcrewes.htm>. *CREWES Reflectivity Explorer 2.0*. Retrieved 14.10.2014.
- Drottning, A, Branston, M, & Lecomte, I. (2009). Value of illumination-consistent modelling in time-lapse seismic analysis. *First break*, 27(10).
- Durrani, Javaid A, French, William S, & Comeaux, Lynn B. (1987). *New directions for marine 3-D surveys*. Paper presented at the 1987 SEG Annual Meeting.
- Egan, Mark S, Dingwall, Ken, & Kapoor, Jerry. (1991). Shooting direction: A 3-D marine survey design issue. *The Leading Edge*, 10(11), 37-41.
- Fossen, Haakon. (2010). *Structural geology*: Cambridge University Press.
- Fossen, Haakon, & Gabrielsen, Roy H. (1996). Experimental modeling of extensional fault systems by use of plaster. *Journal of Structural Geology*, 18(5), 673-687.
- Fossen, Haakon, & Hesthammer, Jonny. (1998). Structural geology of the Gullfaks field, northern North Sea. *Special publication-Geological Society of London*, 127, 231-262.
- Fowler, C Mary R. (1990). *The solid earth: an introduction to global geophysics*: Cambridge University Press.
- Gabrielsen, Roy H, & Clausen, Jill A. (2001). Horses and duplexes in extensional regimes: A scale-modeling contribution. *Memoirs-Geological Society of America*, 207-220.
- Gardner, GHF, Gardner, LW, & Gregory, AR. (1974). Formation velocity and density-the diagnostic basics for stratigraphic traps. *Geophysics*, 39(6), 770-780.
- Gelius, Leiv-J, & Johansen, Tor Arne. (2010). *Petroleum Geophysics*. UniGEO as.
- Hesthammer, J, Landrø, M, & Fossen, H. (2001). Use and abuse of seismic data in reservoir characterisation. *Marine and Petroleum Geology*, 18(5), 635-655.
- Kearey, Philip, Brooks, Michael, & Hill, Ian. (2002). *An introduction to geophysical exploration*: John Wiley & Sons.
- Keym, Matthias, Dieckmann, Volker, Horsfield, Brian, Erdmann, Michael, Galimberti, Roberto, Kua, Lung-Chuan, . . . Podlaha, Olaf. (2006). Source rock heterogeneity of the Upper Jurassic Draupne Formation, North Viking Graben, and its relevance to petroleum generation studies. *Organic Geochemistry*, 37(2), 220-243.



- Lecomte, Isabelle. (2008). Resolution and illumination analyses in PSDM: A ray-based approach. *The Leading Edge*, 27(5), 650-663.
- Lecomte, Isabelle, & Gelius, Leiv-J. (1998). *Have a Look At the Resolution of Prestack Depth Migration For Any Model Survey And Wavefields*. Paper presented at the 1998 SEG Annual Meeting.
- Lecomte, Isabelle, Gjøystdal, Håvar, & Drottning, Åsmund. (2003). *Simulated Prestack Local Imaging: a Robust And Efficient Interpretation Tool to Control Illumination Resolution And Time-lapse Properties of Reservoirs*. Paper presented at the 2003 SEG Annual Meeting.
- Lindsey, J. (1989). The Fresnel zone and its interpretative significance: *The Leading Edge*, 8, 33-39.
- Lines, Laurence R, & Newrick, Rachel Therese. (2004). *Fundamentals of geophysical interpretation: Society of Exploration Geophysicists*.
- Long, Andrew S, Ramsden, Charles RT, & Hoffmann, Jurgen. (2004). On the issue of strike or dip streamer shooting for 3D multi-streamer acquisition. *Exploration Geophysics*, 35(2), 105-110.
- Manin, M, & Hun, F. (1992). *Comparison of seismic results after dip and strike acquisition*. Paper presented at the 54th EAEG Meeting.
- Marjanac, Tihomir, & Steel, Ronald J. (1997). Dunlin Group sequence stratigraphy in the northern North sea: a model for Cook Sandstone deposition. *AAPG bulletin*, 81(2), 276-292.
- McClay, KR, & Ellis, PG. (1987). Geometries of extensional fault systems developed in model experiments. *Geology*, 15(4), 341-344.
- NORSAR. (2011). SeisRoX 3.0 Training Manual. In N. I. AS (Ed.).
- NORSAR. (2014). Seismic Modelling: Products: SeisRoX. Available: <http://www.norsar.no/seismod/Products/SeisRoX/>. 3.0. Retrieved 01.10.2014.
- Norton, MG. (1986). Late Caledonide extension in western Norway: A response to extreme crustal thickening. *Tectonics*, 5(2), 195-204.
- Rafaelsen, Bjarne. (2006). Seismic resolution (and frequency filtering). Available: [http://folk.uio.no/hanakrem/svalex/E-learning/geophysics/Seismic\\_resolution.pdf](http://folk.uio.no/hanakrem/svalex/E-learning/geophysics/Seismic_resolution.pdf). Retrieved 02.10.2014
- Sales, John K. (1987). Tectonic Models, Tectonic models *Structural Geology and Tectonics* (pp. 785-794): Springer.
- Struijk, AP, & Green, RT. (1991). The Brent Field, Block 211/29, UK North Sea. *Geological Society, London, Memoirs*, 14(1), 63-72.
- Vollset, J, & Doré, Anthony G. (1984). *A revised Triassic and Jurassic lithostratigraphic nomenclature for the Norwegian North Sea*: Oljedirektoratet.
- Zoeppritz, K. (1919). Über Reflexion and Durchgang seismischer Wellen durch Unstetigkeits-flächen. *Gott. Nachr. Math. Phys. Kl*, 66-84.

# APPENDIX A

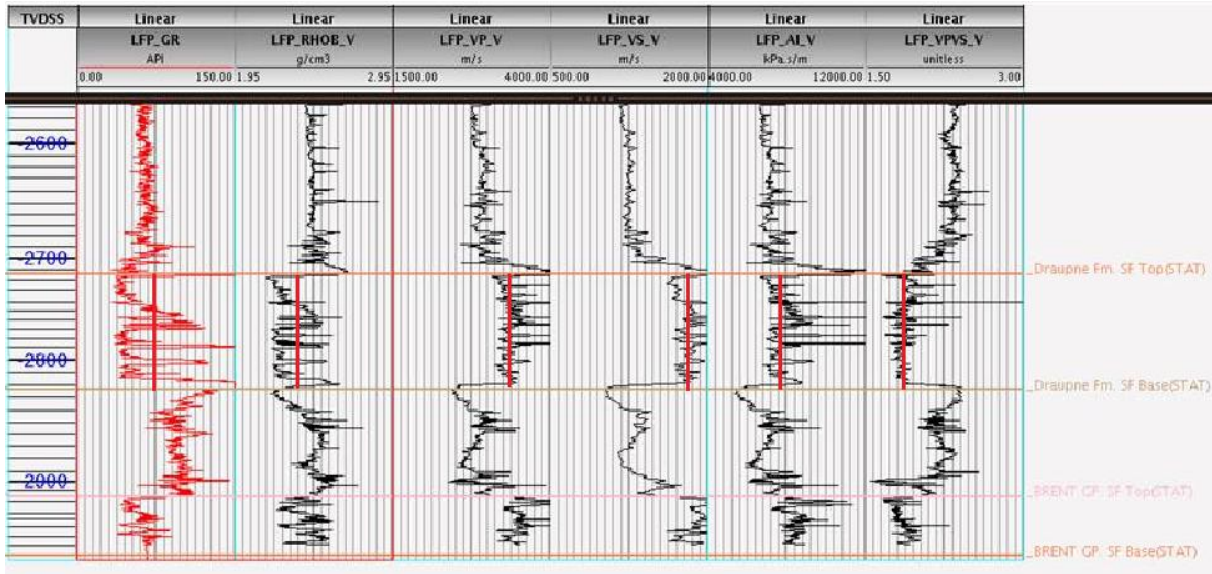


**Figure A.1:** Well log 2, showing the approximate mean values (red vertical lines) of the gamma ray log, density,  $V_P$ ,  $V_S$ , acoustic impedance and the  $V_P/V_S$  ratio of the Draupne Formation.

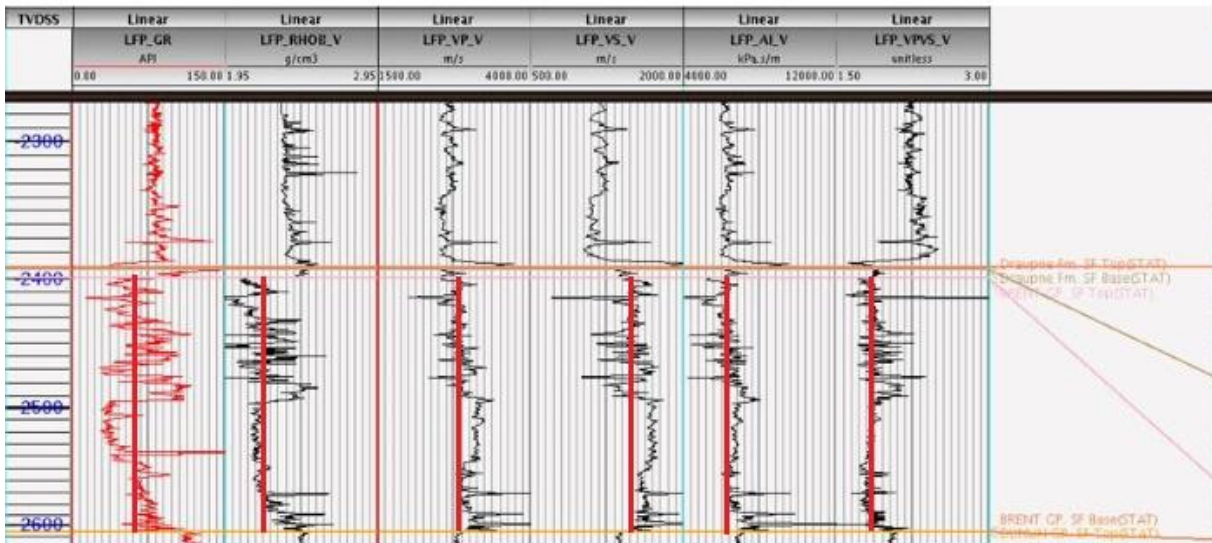


**Figure A.2:** Well log 1, showing the approximate mean values (red vertical lines) of the gamma ray log, density,  $V_P$ ,  $V_S$ , acoustic impedance and the  $V_P/V_S$  ratio of the Brent Group.

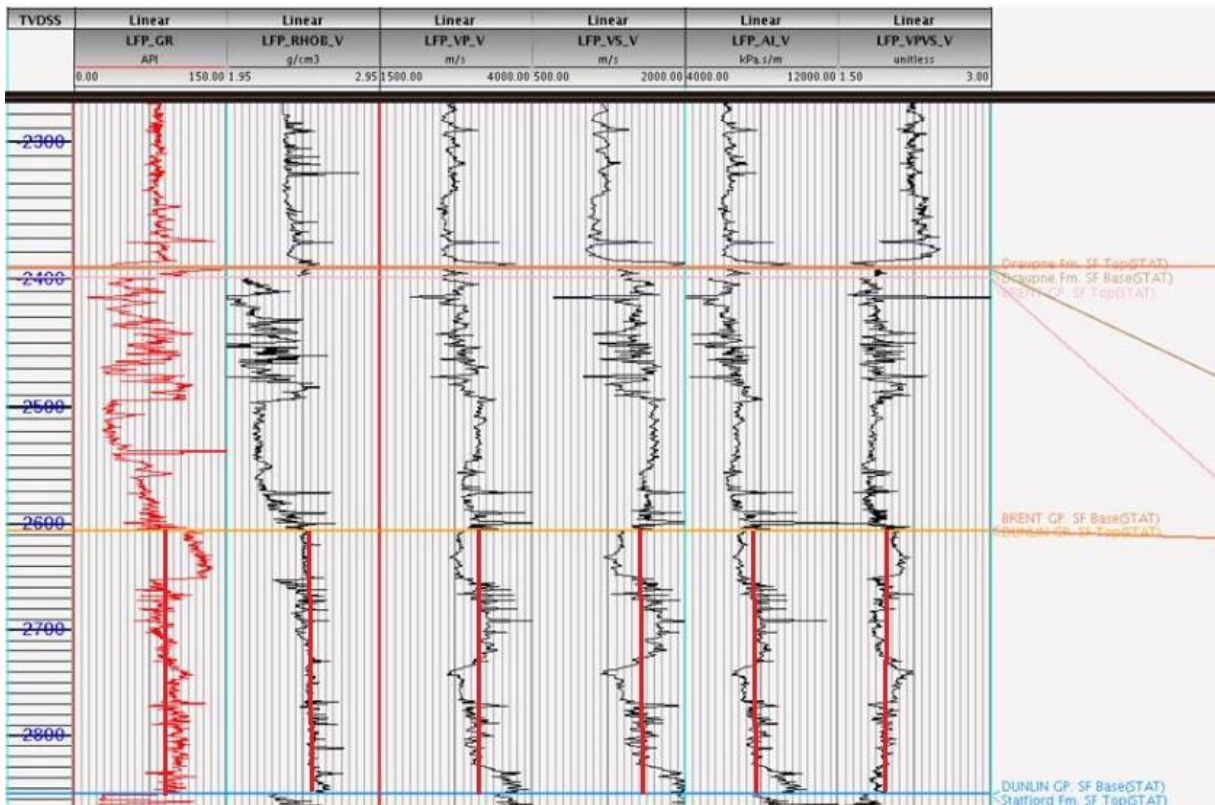


**Figure A.3:** Well log 1, showing the approximate mean values (red vertical lines) of the gamma ray log, density,  $V_P$ ,  $V_S$ , acoustic impedance and the  $V_P/V_S$  ratio of the Dunlin Group.

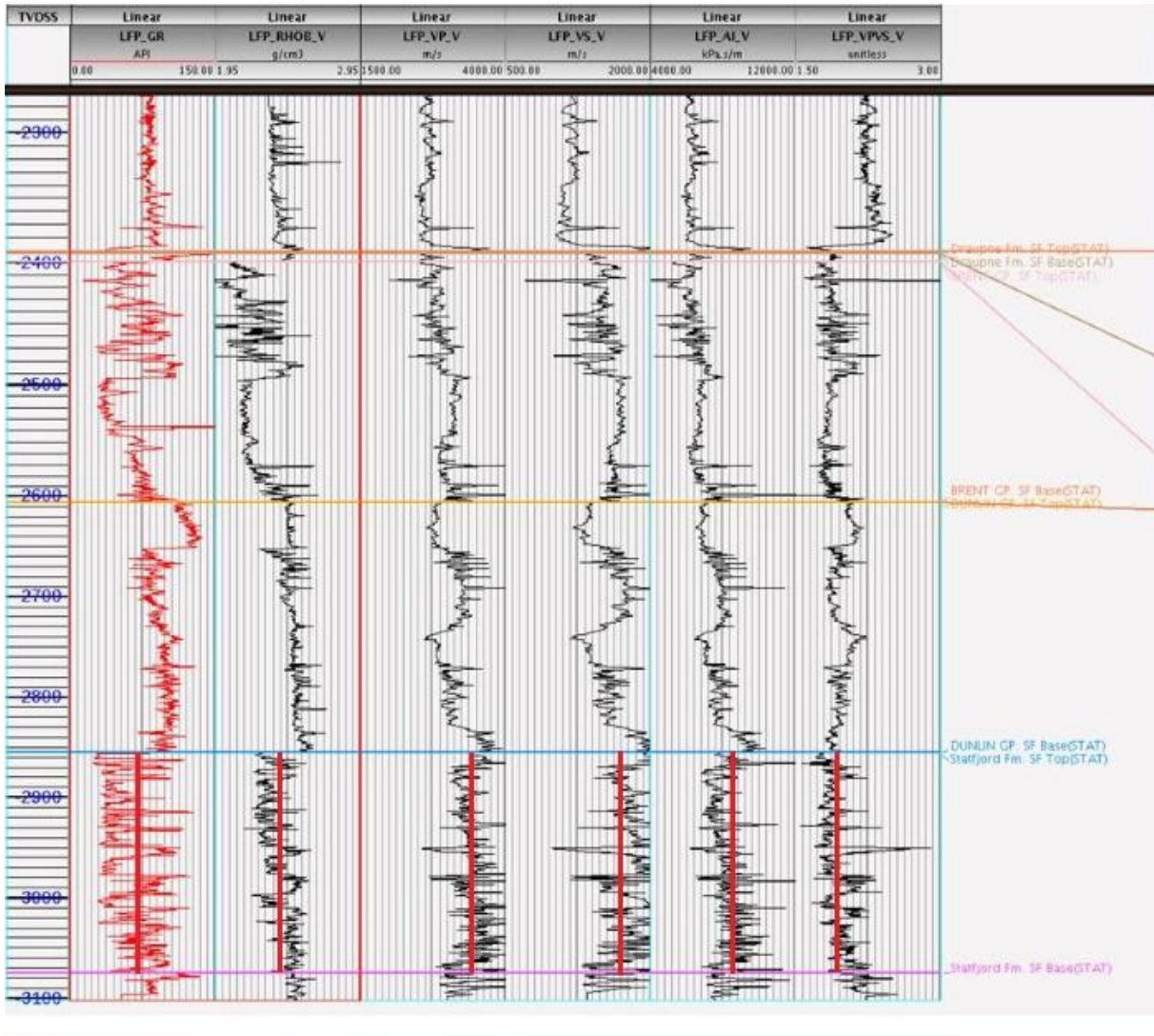


**Figure A.4:** Well log 1, showing the approximate mean values (red vertical lines) of the gamma ray log, density,  $V_P$ ,  $V_S$ , acoustic impedance and the  $V_P/V_S$  ratio of the Statfjord Formation.

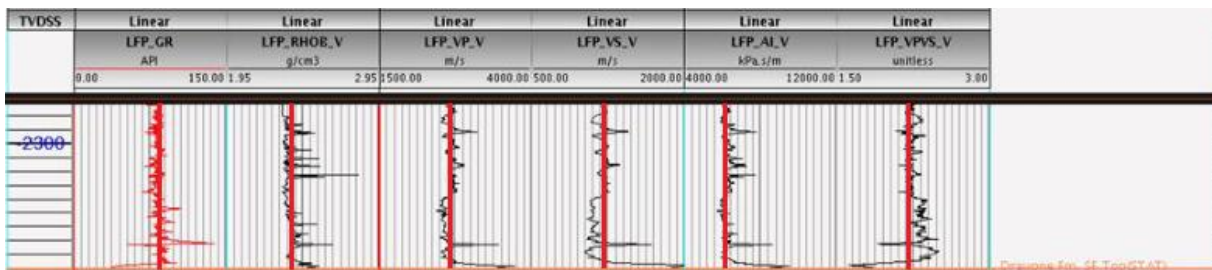


**Figure A.5:** Well log 1, showing the approximate mean values (red vertical lines) of the gamma ray log, density,  $V_P$ ,  $V_S$ , acoustic impedance and the  $V_P/V_S$  ratio of the Unknown Formation used as layer 5 (uppermost layer of both plaster models), just above the Draupne Formation.

**Table A.1:** *Approximate mean values of the elastic properties in the different formations used in the synthetic seismic modeling, gathered from well logs (Appendix A). Also, the table displays the  $V_P$ ,  $V_S$  and  $\rho$  after being increased with 10% and 20%.*

<b>Fm./Group</b>	<b>Density (g/cm<sup>3</sup>)</b>	<b>V<sub>P</sub> (km/s)</b>	<b>V<sub>S</sub> (km/s)</b>	<b>V<sub>P</sub>/V<sub>S</sub></b>
Overburden	2.10	2.50	1.10	2.27
Unknown Fm.	2.40	2.70	1.20	2.25
Draupne Fm.	2.35	2.80	1.80	1.80
Brent Gr.	2.20	2.70	1.50	1.80
Dunlin Gr.	2.55	3.00	1.60	1.90
Statfjord Fm.	2.45	3.40	1.70	1.80
<b>Increase 10%</b>	<b>Density (g/cm<sup>3</sup>)</b>	<b>V<sub>P</sub> (km/s)</b>	<b>V<sub>S</sub> (km/s)</b>	<b>V<sub>P</sub>/V<sub>S</sub></b>
Overburden	2.31	2.75	1.21	2.27
Unknown Fm.	2.64	2.97	1.32	2.25
Draupne Fm.	2.59	3.08	1.98	1.80
Brent Gr.	2.42	2.97	1.65	1.80
Dunlin Gr.	2.81	3.30	1.76	1.90
Statfjord Fm.	2.70	3.74	1.87	1.80
<b>Increase 20%</b>	<b>Density (g/cm<sup>3</sup>)</b>	<b>V<sub>P</sub> (km/s)</b>	<b>V<sub>S</sub> (km/s)</b>	<b>V<sub>P</sub>/V<sub>S</sub></b>
Overburden	2.52	3.00	1.32	2.27
Unknown Fm.	2.88	3.24	1.44	2.25
Draupne Fm.	2.82	3.36	2.16	1.80
Brent Gr.	2.64	3.24	1.80	1.80
Dunlin Gr.	3.06	3.60	1.92	1.90
Statfjord Fm.	2.94	4.08	2.04	1.80

**Table A.2:** Based on velocity- and density values in table A.1, the shear modulus and bulk modulus were calculated in order to create lithologic models. Each lithologic model corresponds to a layer in the plaster models, displayed in Chapter 5.2.

Formation/Group	Core depth (m)	Shear modulus (GPa)	Bulk modulus (GPa)	Gamma-ray (API)	Acoustic impedance (kPa s/m)
Overburden		2.5410	9.7370		
Unknown Fm.	-2390	3.4560	12.8880	80	7700
Draupne Fm.	2710-2820	7.6140	8.2720	75	7500
Brent Gr.	2400-2610	4.9500	9.4380	70	6000
Dunlin Gr.	2610-2850	6.5280	14.2460	85	6900
Statford Fm.	2850-3070	7.0805	18.4664	70	7550

## APPENDIX B

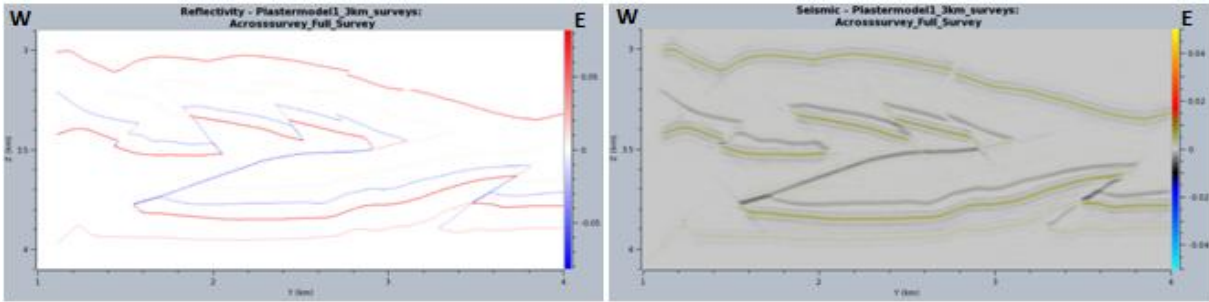


**Figure B.1:** Reflectivity series and seismogram discussed in Chapter 7. Incident angle:  $0^\circ$ , IVEC range:  $0^\circ - 5^\circ$ .

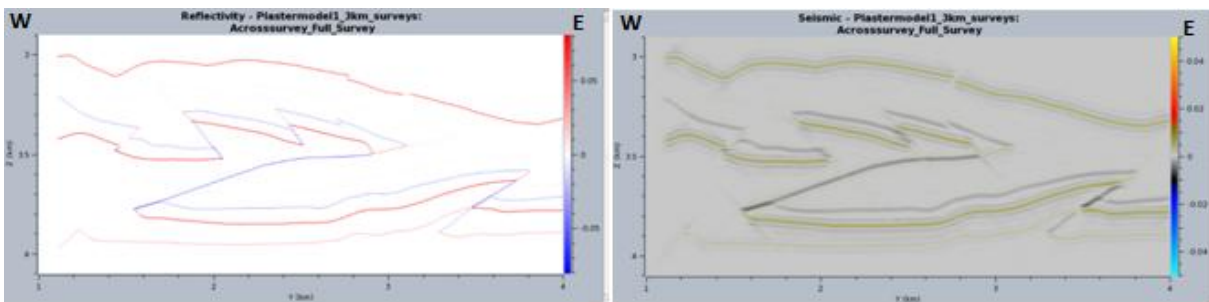


**Figure B.2:** Reflectivity series and seismogram discussed in Chapter 7. Incident angle:  $10^\circ$ , IVEC range:  $5^\circ - 15^\circ$ .

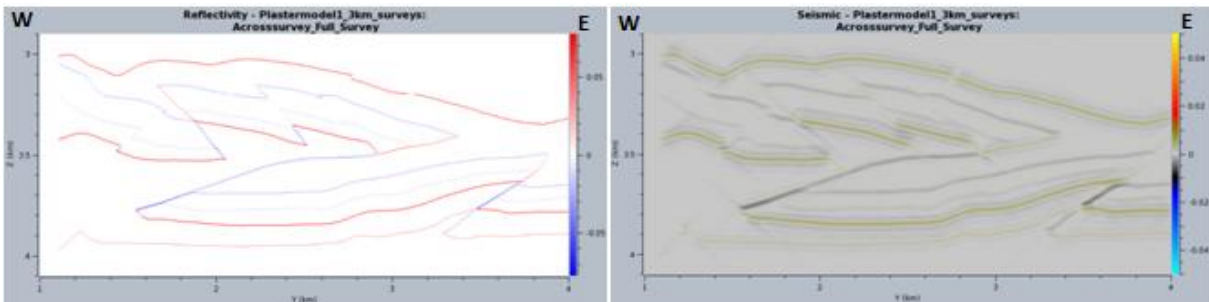


**Figure B.3:** Reflectivity series and seismogram discussed in Chapter 7. Incident angle:  $20^\circ$ , IVEC range:  $15^\circ - 25^\circ$ .

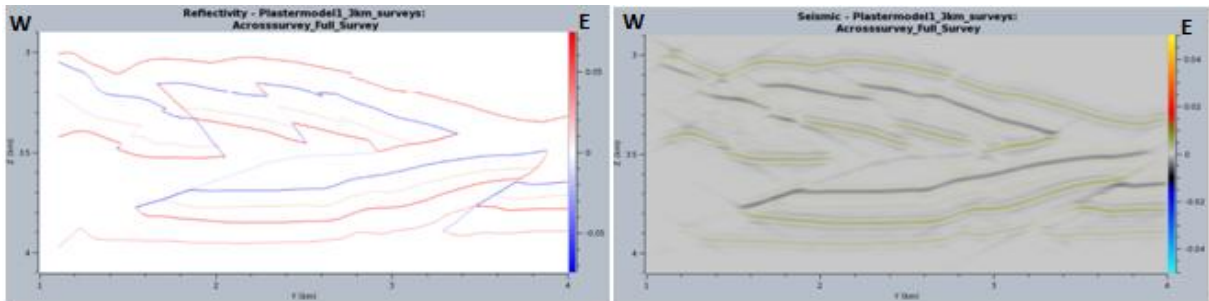


**Figure B.4:** Reflectivity series and seismogram discussed in Chapter 7. Incident angle:  $30^\circ$ , IVEC range:  $25^\circ - 35^\circ$ .

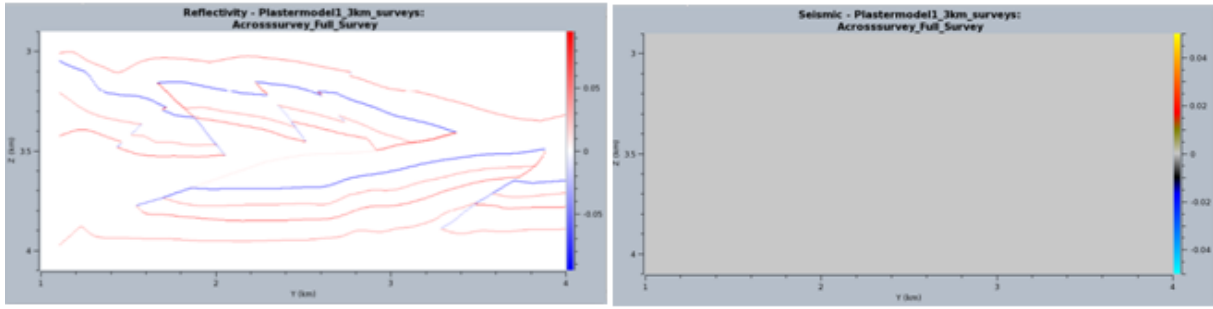


**Figure B.5:** Reflectivity series and seismogram discussed in Chapter 7. Incident angle:  $40^\circ$ , IVEC range:  $35^\circ - 45^\circ$ . Notice that there is no resulting seismogram for this incidence angle, even though the reflectivity series are present.

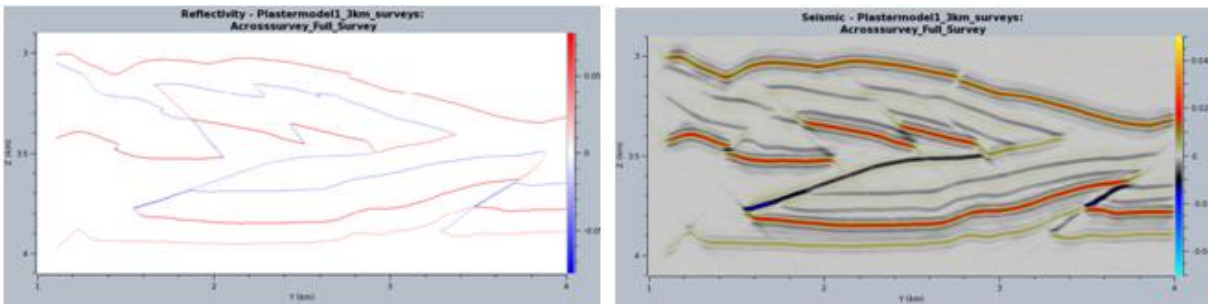


**Figure B.6:** Average reflectivity series and seismogram. Incident angle sum. IVEC range:  $0^\circ - 45^\circ$ . Here, all layer boundaries are reflected.